University of Wollongong

Research Online

University of Wollongong Thesis Collection 1954-2016

University of Wollongong Thesis Collections

2016

The effect of cooling rate and coiling temperature on the niobium retention in ultrathin castrip steel

Zhizhang Wang
University of Wollongong

Follow this and additional works at: https://ro.uow.edu.au/theses

University of Wollongong

Copyright Warning

You may print or download ONE copy of this document for the purpose of your own research or study. The University does not authorise you to copy, communicate or otherwise make available electronically to any other person any copyright material contained on this site.

You are reminded of the following: This work is copyright. Apart from any use permitted under the Copyright Act 1968, no part of this work may be reproduced by any process, nor may any other exclusive right be exercised, without the permission of the author. Copyright owners are entitled to take legal action against persons who infringe their copyright. A reproduction of material that is protected by copyright may be a copyright infringement. A court may impose penalties and award damages in relation to offences and infringements relating to copyright material. Higher penalties may apply, and higher damages may be awarded, for offences and infringements involving the conversion of material into digital or electronic form.

Unless otherwise indicated, the views expressed in this thesis are those of the author and do not necessarily represent the views of the University of Wollongong.

Recommended Citation

Wang, Zhizhang, The effect of cooling rate and coiling temperature on the niobium retention in ultrathin castrip steel, Master of Engineering Materials thesis, School of Mechanical, Materials and Mechatronic Engineering, University of Wollongong, 2016. https://ro.uow.edu.au/theses/4867

Research Online is the open access institutional repository for the University of Wollongong. For further information contact the UOW Library: research-pubs@uow.edu.au

UNIVERSITY OF WOLLONGONG

THE EFFECT OF COOLING RATE AND COILING TEMPERATURE ON THE NIOBIUM RETENTION IN ULTRA-THIN CASTRIP STEEL

By

Zhizhang Wang

"This thesis is presented as part of the requirements for the award of the Degree of

Master of engineering materials

From

University of Wollongong

Faculty of Engineering

August 2016

Acknowledgment

I would like to thank Dr ZhiXin Chen for his supporting and encouragements. I also thank him for giving me many useful advises during my research work and aided me in preparing my thesis. I couldn't make progress in my research study without his help.

I would like to thank Drs Chris Killmore of BlueScope and Kristin Carpenter for many useful discussions and Dr Liang Chen for helping me in my numerous experiments.

Finally, my deepest regards are to my parents who financially and mentally supported me during my entire research study in Australia.

Table of Contents

Acknowledgment I

Abstract V

List of Figures VI

List of Tables XIII

1 Introduction 1

2 Literature review 3

2.1 CASTRIP process 3

2.2 Microstructure and phase transformation of low carbon steel in CASTRIP Process 4

2.2.1 Microstructures and phase transformations in steel 4

2.2.2 The influence of reheating temperature on γ-α phase transformation 31

2.2.3 The influence of hot rolling reduction on phase transformation of low carbon steel in CASTRIP process 33

2.2.4 Effect of cooling rate and coiling temperature on γ-α phase transformation 34

2.3 Precipitation hardening in HSLA steel 38

2.3.1 Introduction of precipitation hardening 38

2.3.2 Analysis of precipitate in precipitation hardening 40

2.3.3 Strengthen mechanism of precipitation hardening 50

2.3.4 The influence of cooling rate and coiling temperature on the Nb retention in low carbon steel in CASTRIP process 51

2.4 Literature review summary 61

3 Experimental Procedure 61

3.1 Materials 61

3.2 Experimental approach 62

3.2.1 Heat treatment 62

3.2.2 Sample sectioning 66

3.2.3 Sample mounting 67

3.2.4 Grinding and polishing 68

3.2.5 Etching 71

3.2.6 Optical Microscope 71

3.2.7 Vickers Hardness and Microhardness tests 72
3.3 Optical microscopy 74
3.3.1 Austenite grain size measurement 74
3.3.2 Volume fraction of constituents measurement 76
3.4 Construct dilatation curve 77
4 Results 78
4.1 Microstructure, phase transformation and hardness of the samples solution treated at 1280°C and cooled from 900°C to the coiling temperature of 675°C at the cooling rates: 1 °C/s, 5°C/s and 40°C/s 78
4.1.1 The sample cooled at 1 °C/s 78
4.1.2 The sample cooled at 5°C/s 80
4.1.3 The sample cooled at 40°C/s 83
4.2 Microstructure, phase transformation and hardness of the samples solution treated at 1280°C and cooled from 900°C to the coiling temperature of 500°C at the cooling rates: 1 °C/s, 5°C/s and 40°C/s 85
4.2.1 The sample cooled at 1°C/s 85
4.2.2 The sample cooled at 5°C/s 87
4.2.3 The sample cooled at 40°C/s 88
4.3 Microstructure, phase transformation and hardness of the samples solution treated at 1150°C and cooled from 900°C to the coiling temperature of 675°C at the cooling rates: 1 °C/s, 5°C/s and 40°C/s 90
4.3.1 The sample cooled at 1°C/s 90
4.3.2 The sample cooled at 5°C/s 92
4.3.3 The sample cooled at 40°C/s 94
4.4 Microstructure, phase transformation and hardness of the samples solution treated at 1150°C and cooled from 900°C to the coiling temperature of 500°C at the cooling rates: 1 °C/s, 5°C/s and 40°C/s 96
4.4.1 The sample cooled at 1°C/s 96
4.4.2 The sample cooled at 5°C/s 98
4.4.3 The sample cooled at 40°C/s 100
4.5 Vickers hardness of the sample and the micro Vickers hardness of the constituent after age hardening 102
4.6 Result summary 104
4.6.1 The effect of cooling rate and coiling temperature on phase transformation 104
4.6.2 The influence of the cooling rate and coiling temperature on micro Vickers hardness of each constituent and Vickers hardness of the sample 105

4.6.3 The influence of reheating temperature on the austenite grain size and phase transformation 109

5 Discussions 112

5.1 The influence of the reheating temperature on the retention of Nb 112

5.2 The influence of the cooling rate on the Nb retention 113

5.3 The effect of the coiling temperature on the Nb retention in the UCS steel 115

6 Conclusions 117

7 Suggestions for Future Works 118

8 References 120

Abstract

The main objective of this study is to investigate the effect of the cooling rate from 1 to 40°C/s and the coiling temperatures of 500 and 675°C on the niobium retention in ultra-thin CASTRIP steel.

The samples were solution treated at 1150 and 1280°C for 5 mins and cooled to 900°C at the cooling rate of 50°C/s. Then the samples were cooled from 900°C to the coiling temperatures of 675 and 500°C at 1, 5 or 40°C/s. The cooling rate from the coiling temperatures to 300°C was at 0.17°C/s. The samples were age hardened at 700°C for 60s. All the experiments were carried out on a theta dilatometer and dilatation curves obtained from the dilatometer were used to analyse the γ-α phase transformation of the samples in the temperature ranges of 900 to 500°C. The microstructures of the samples in the various cooling conditions were characterized to determine the influence of the cooling rates and coiling temperatures on the γ-α phase transformations. An INDENTEC Vickers hardness tester and a LECO M-400-H1 Micro Vickers hardness testing machine were used to measure the Vickers hardness of the samples and Micro Vickers hardness of the individual constitutes. The hardness results were used to assess how the cooling rates and coiling temperatures influenced the niobium retention in the samples.

It was found as expected that at the coiling temperature of 500°C, more Nb atoms were retained in the solid solution for the sample cooled at the cooling rate of 40°C/s compared to the samples cooled at 1 and 5°C/s However, at the coiling temperature of 675°C, more Nb atoms were retained in the solid solution for the sample cooled at 1°C/s compared to the samples cooled at 5 and 40°C/s. This may be due to the fact that the coiling temperature of 675°C is well within the γ→α transformation temperature range and the cooling rate below the coiling temperature is one magnitude slower than the cooling rates above the coiling temperature. The retention of Nb depends on the γ→α transformation temperature range of the samples and most of the γ→α transformation occurred above the coiling temperature of 675°C for the sample cooled at 1°C/s and the most of the γ→α transformation occurred at or below the coiling temperature. Consequently more Nb will be retained and the larger age hardening effect was obtained in the samples cooled at 1 °C/s. The reheating temperature also has an effect on the retention of the Nb in the samples. The higher the reheating temperature the lower Nb retention and lower age hardening effect in the samples. This may be explained by the fact that the higher reheating temperature resulted in the larger austenite grain size and the lower γ→α transformation temperatures. The austenite grain size of CASTTRIP steel is more likely larger than the austenite sizes used in this investigation. The retention of Nb in CASTRIP steel is likely smaller than the one obtained in this investigation.

List of Figures

Figure 2.1 Main components of the CASTRIP process 4

Figure 2.2 Fe-Fe3C phase diagram 6

Figure 2.3 Schematic representations of the microstructures for an iron-carbon alloy (containing less than 0.76wt%C). As it is cooled from within the austenite phase region to below the eutectoid temperature 6

Figure 2.4 Schematic representation of the formation of pearlite from austenite; direction of carbon diffusion indicated by arrows 8

Figure 2.5 Microstructure of a sheaf of upper bainite....9

Figure 2.6 Optical micrograph of bainite microstructures in Fe-Ni-C alloys....10

Figure 2.7 Classification of bainite based upon carbide precipitation: (a) upper bainite, (b) lower bainite....10

Figure 2.8 Schematic representation of formation of a bainite sheaf by repeated nucleation and limited growth of sub-units and its effect on overall transformation kinetics 11

Figure 2.9 Photomicrograph showing the martensitic microstructure. The needle-shape grains are the martensite phase, and the white regions are austenite that failed to transform during the rapid quench 12

Figure 2.10 Polygonal ferrite formed in HSLA-80 steel isothermally transformed at 675 C (1250 F) for 500 s. Martensite (dark structure) has formed during cooling in austenite untransformed after the isothermal hold. Light micrograph, nital etch....13

Figure 2.11 Micrographs of recent UCS steels, where shows acicular ferrite nucleating at two non-metallic inclusions 14

Figure 2.12 Pearlite in a furnace-cooled Fe-0.75C alloy. Picral etch. Original magnification at 500. Courtesy of A.R. Marder and A. Benscoter, Bethlehem Steel Corp., Beth-lehem, PA …..15

Figure 2.13 Schematic diagram which indicates that pearlite grows as nodules on one side of the prior austenite boundaries and at grain corners 15

Figure 2.14 CCT diagram for UCS steel with 0.024% Nb.....16

Figure 2.15 Granular ferrite formed by continuous cooling of a low carbon steel. Nital etch, light micrograph. Courtesy of B. Kloberdanz, Colorado School of Mines 17

Figure 2.16 Demonstration of how a time temperature transformation diagram (bottom) is generated from percentage transformation-versus-logarithm of time measurements (top).....19

Figure 2.17 Isothermal transformation diagram for a eutectoid iron-carbon alloy, with superimposed isothermal heat treatment curve Microstructures before, during, and after the austenite-to-pearlite transformation are shown 20

Figure 2.18 The complete time temperature transformation diagram for an iron-carbon alloy of eutectoid composition 21

Figure 2.19 CCT diagrams for the low carbon steel with 0.08% Nb.....22

Figure 2.20 Dilatation curve obtained at 1 K/s cooling rate for Ultrahigh-Thickness Cr-Mo Steel 24

Figure 2.21 Sketch of the dilatometer experiment.....25

Figure 2.22 Heating dilatation curve of a low carbon steel (Fe–0.11C–0.50Mn) obtained at a heating rate of 0.05K s-1 27

Figure 2.23 Diagram of the heating dilatation curve response of α-γ transformation and the carbide dissolution process of martensitic stainless steels 28

Figure 2.24 Cooling dilatation curve of a carbon manganese steel (Fe-0.20C-1.1Mn-0.34Si) obtained at a cooling of 1K s^{-1} 29

Figure 2.25 Optical micrographs corresponding to the evolution of ferrite and pearlite formation during cooling at a rate of 1 K s-1 in a carbon manganese steel (Fe– 0.20C–1.1Mn–0.34Si). Quench-out temperatures: (a) 765 °C; (b) 758°C (Ar3); (c) 754°C; (d)746 °; (e) 726°; (f) 676°; (g) 636°; (h) 626° (Ar_1); (i) room temperature 30

Figure 2.26 Cooling dilatometric curve and of a low carbon manganese steel (Fe – 0.07C–1.56Mn–0.41Si) after cooling at a rate of 234 K s-1 31

Figure 2.27 Variation of austenite grain size with holding time at reheating temperatures of 1153 and 1223 K.....32
Figure 2.28 Effect of holding time on morphology of austenite grain at 1223 K.....32
Figure 2.29 Effect of hot rolling reduction on austenite grain size measured through the thickness of a UCS strip.....33
Figure 2.30 Optical microstructures for 0.06% Nb UCS flat dilatometer samples cooled at (a) 3 °C/s αq + αB, (b) 10 °C/s αq + αB + ~αB°, (c) 30 °C/s αB + αB°, and (d) 60 °C/s αB + αB°.35
Figure 2.31 Vickers hardness, HV5, as a function of increasing cooling rate and increasing Nb addition 36
Figure 2.32 Microstructures for 0.024%Nb UCS steel at different coiling temperatures, a) 490ºC, b) 535ºC, c) 570ºC and d) 650ºC 37
Figure 2.33 Effect of coiling temperature on yield strength of the C-Mn-Si base UCS steel and various Nb microalloyed UCS steels 37
Figure 2.34 Schematic diagram of age hardening 39
Figure 2.35 Solubility products of main precipitate species in HSLA steels 39
Figure 2.36 Dislocation motion may continue through second phase particles (particle cutting) 42
Figure 2.37 Relationship between shear strength increment and particle radius.....43
Figure 2.38 Dislocation meets hard undeformable second phase particles; dislocation release higher stresses may occur by Orowan looping or by cross-slip 44
Figure 2.39 Ashby-Orowan relationship.....45
Figure 2.40 Zones or precipitate phase (aging) with lattice distortion.....46
Figure 2.41 Equilibrium phase (Overaging) without distortion 46
Figure 2.42 Solubility products of main precipitate species in HSLA steels 48
Figure 2.43 Hardness as a function of aging time for Nb-free, 0.04wt% and 0.08wt% Nb steel aged at 800°C 49
Figure 2.44 Laboratory aging results for V, Nb and V+Nb steels for strength as a function of peak aging temperature 50

Figure 2.45 Thermal schedules of the simulation for solidification and cooling 52
Figure 2.46 Amounts of Nb and Ti precipitated in precipitates formed in the cast slab, and in the simulated samples measured by dissolution and filtration with ICP spectroscopy 53
Figure 2.47 Heat treatment used in experiment.....54
Figure 2.48 Effect of cooling rate on Nb precipitation after austenitization at 1350°C.....55
Figure 2.49 Schematic diagram of the simulation for forging and cooling.....56
Figure 2.50 Schematic diagram of the simulation for rolling and cooling.....57
Figure 2.51 Continuous cooling transformation diagram(CCT) calculated by JMatPro 58
Figure 2.52 Bright field TEM micrographs of Ti-Nb-Mo steel at different cooling rates showing fine carbide precipitates at (a) 0.5°C/s (b) 1°C/s (c) 5°C/s, and (d)precipitation at subgrain boundary.....58
Figure 2.53 Schematic diagram dividing the variation of microhardness with interrupted cooling temperature into three different regions and further associating the microhardness with the carbide precipitation by corresponding TEM images 60
Figure 2.54 The average size of precipitates of the steels treated by the different simulated hot-coiling temperatures.....60
Figure 3.1 Theta Dilatometer 62
Figure 3.2 Dilatometer sample 63
Figure 3.3 Heat treatment simulated CASTRIP process under the condition of 1280˚C reheating temperature.....64
Figure 3.4 Control experiment under the condition of 1150˚C reheating temperature 65
Figure 3.5 Antitheses to show age hardening performance.....65
Figure 3.6 Heat treatment simulated post age hardening heat treatment.....66
Figure 3.7 Accutom 5/50 Sectioning machine 67
Figure 3.8 Struers CitoPress-20 mounting machine 68
Figure 3.9 The Struers grinding and polishing equipment used in the experiment 69
Figure 3.10 Metalogram.....69
Figure 3.11 Light optical Microscope used in the experiment 72

Figure 3.12 INDENTEC Vickers hardness testing machine 73

Figure 3.13 LECO M-400-H1 micro Vickers hardness testing machine 73

Figure 3.14 Outline austenite grain boundary based on bainitic ferrite 75

Figure 3.15 Eight austenite grains are measured to calculate austenite grain size 75

Figure 3.16 Ten austenite grains are measured to calculate austenite grain size.....75

Figure 3.17 Thirteen austenite grains are measured to calculate austenite grain size.....76

Figure 3.18 Dilatation curve mapped in the experiment.....77

Figure 4.1 Optical micrograph showing the transformation of microstructure for the sample cooled from 900°C to the coiling temperature of 675°C at the cooling rate of 1°C/s under the condition of the 1280°C reheating temperature.....79

Figure 4.2 Dilatation curve obtained for the sample at the cooling rate of 1°C/s with the coiling temperature of 675°C under the condition of the 1280°C reheating temperature 80

Figure 4.3 Optical micrograph showing the transformation of microstructure for the sample cooled from 900°C to the coiling temperature of 675°C at the cooling rate of 5°C/s under the condition of the 1280°C reheating temperature.....81

Figure 4.4 Microstructure of the sample cooled from 900^0C to the coiling temperature of 675°C at the cooling rate of 5°C/s, showing pearlites were produced in this cooling condition. 81

Figure 4.5 Dilatation curve obtained for the sample at the cooling rate of 5°C/s with the coiling temperature of 675°C under the condition of the 1280°C reheating temperature 82

Figure 4.6 Optical micrograph showing the transformation of microstructure for the sample cooled from 900°C to the coiling temperature of 675°C at the cooling rate of 40°C/s under the condition of the 1280°C reheating temperature.....83

Figure 4.7 Dilatation curve obtained for the sample at the cooling rate of 40°C/s with the coiling temperature of 675°C under the condition of the 1280°C reheating temperature 84

Figure 4.8 Optical micrograph showing the transformation of microstructure for the sample cooled from 900°C to the coiling temperature of 500°C at the cooling rate of 1°C/s under the condition of the 1280°C reheating temperature.....85

Figure 4.9 Dilatation curve obtained for the sample at the cooling rate of 1°C/s with the coiling temperature of 500°C under the condition of the 1280°C reheating temperature 86
Figure 4.10 Optical micrograph showing the transformation of microstructure for the sample cooled from 900°C to the coiling temperature of 500°C at the cooling rate of 5°C/s under the condition of the 1280°C reheating temperature.....87
Figure 4.11 Dilatation curve obtained for the sample at the cooling rate of 5°C/s with the coiling temperature of 500°C under the condition of the 1280°C reheating temperature 88
Figure 4.12 Optical micrograph showing the transformation of microstructure for the sample cooled from 900°C to the coiling temperature of 500°C at the cooling rate of 40°C/s under the condition of the 1280°C reheating temperature.....89
Figure 4.13 Dilatation curve obtained for the sample at the cooling rate of 40°C/s with the coiling temperature of 500°C under the condition of the 1280°C reheating temperature.....90
Figure 4.14 Optical micrograph showing the transformation of microstructure for the sample cooled from 900°C to the coiling temperature of 675°C at the cooling rate of 1°C/s under the condition of the 1150°C reheating temperature.....91
Figure 4.15 Dilatation curve obtained for the sample at the cooling rate of 1°C/s with the coiling temperature of 675°C under the condition of the 1150°C reheating temperature 92
Figure 4.16 Optical micrograph showing the transformation of microstructure for the sample cooled from 900°C to the coiling temperature of 675°C at the cooling rate of 5°C/s under the condition of the 1150°C reheating temperature.....93
Figure 4.17 Dilatation curve obtained for the sample at the cooling rate of 5°C/s with the coiling temperature of 675°C under the condition of the 1150°C reheating temperature 94
Figure 4.18 Optical micrograph showing the transformation of microstructure for the sample cooled from 900°C to the coiling temperature of 675°C at the cooling rate of 40°C/s under the condition of the 1150°C reheating temperature.....95
Figure 4.19 Dilatation curves obtained for the sample at the cooling rate of 40°C/s with the coiling temperature of 675°C under the condition of the 1150°C reheating temperature.....96

Figure 4.20 Optical micrograph showing the transformation of microstructure for the sample cooled from 900°C to the coiling temperature of 500°C at the cooling rate of 1°C/s under the condition of the 1150°C reheating temperature.....97
Figure 4.21 Dilatation curve obtained for the sample at the cooling rate of 1°C/s with the coiling temperature of 500°C under the condition of the 1150°C reheating temperature 98
Figure 4.22 Optical micrograph showing the transformation of microstructure for the sample cooled from 900°C to the coiling temperature of 500°C at the cooling rate of 5°C/s under the condition of the 1150°C reheating temperature.....99
Figure 4.23 Dilatation curves obtained for the sample at the cooling rate of 5°C/s with the coiling temperature of 500°C under the condition of the 1150°C reheating temperature.....100
Figure 4.24 Optical micrograph showing the transformation of microstructure for the sample cooled from 900°C to the coiling temperature of 500°C at the cooling rate of 40°C/s under the condition of the 1150°C reheating temperature.....101
Figure 4.25 Dilatation curves obtained for the sample at the cooling rate of 40°C/s with the coiling temperature of 500°C under the condition of the 1150°C reheating temperature.....102

List of Tables

Table 2.1 ISIJ Transformation Products Nomenclature and Classification 22

Table 2.2 Values of the constants A and B 47

Table 2.3 A summary of the microstructural observations 56

Table 3.1 Chemical compositions of the UCS steel.....62

Table 3.2 Wheel Selection based on the characterization of material 67

Table 3.3 Grinding and polishing detail for method D 70

Table 4.1 the Vickers hardness of the samples in various cooling conditions under the conditions of 1150 and 1280°C reheating temperatures after age hardening.....103

Table 4.2 the micro Vickers hardness of the constituent in various cooling conditions under the conditions of 1150 and 1280°C reheating temperatures after age hardening.....103

Table 4.3 Proportion of each constituent for the samples with the different cooling rates and coiling temperatures under the condition of 1280°C reheating temperature.....104

Table 4.4 Proportion of each constituent for the samples with the different cooling rates and coiling temperatures under the condition of the 1150°C reheating temperature 105

Table 4.5 Vickers hardness of the samples at 1280°C reheating temperature from Vickers hardness tester with 1kg load before and after age hardening 106

Table 4.6 Micro Vickers hardness of the constituent of the sample from Micro Vickers hardness tester with 50g load before and after age hardening 107

Table 4.7 Micro Vickers hardness of the constituent of the sample at 1150°C reheating temperature from Micro Vickers hardness tester with 50g load before and after age hardening 108

Table 4.8 Vickers hardness of the samples at 1150°C reheating temperature from Vickers hardness tester with 1kg load before and after age hardening.....109

Table 4.9 Austenite grain size for the sample at the 1150°C reheating temperature 109

Table 4.10 Austenite grain size for the sample at the 1280°C reheating temperature 110

Table 4.11 Phase transformation temperatures for samples in various cooling conditions.....111

Table 5.1 Results summary of the samples in γ-α phase transformation temperature range at various cooling conditions under the condition of 1150℃ or 1280℃ reheating temperature ..113

1 Introduction

Nowadays, the biggest challenge steel industry has to meet is protecting environment and saving resources. In fact, it is hard to balance the environment pollution and cost of production. Therefore, it is necessary to develop the technology of manufacture for steel industry to save resources and protect environment. CASTRIP process is a revolutionary new technique for producing Ultra-Thin cast strip steel, which owns many advantages over conventional casting and rolling technologies, including a smaller carbon foot print, lower cost of production, simpler and more flexible operating plants and improved environmental performance. The world's first commercial installation of CASTRIP process for the production of Ultra-Thin Cast Strip (UCS) is located in Nucor Steel's Crawfordsville, Indian plant. The facility has been producing low-carbon sheet steel since its start-up in 2002. The CASTRIP process is mainly composed of three parts: twin-roll casting, hot rolling reduction, cooling control process. The steel is produced from liquid steel with a rapid solidification rate in twin-roll casting followed by hot rolling reduction to 0.9-1.5 mm thickness. Finally, on the run-out-table, the steel is cooled by water cooling which is controlled by air mist. Control of cooling rate plays an important role in achieving desired microstructure and mechanical properties of the UCS products.

There are many strengthening mechanisms in UCS steel, including grain refinement hardening, solid solution hardening and precipitation hardening. Precipitation hardening, as an effect strengthening mechanisms, is usually used to strengthen UCS steel after the CASTRIP process. It is well known that the effective precipitation hardening

performance can be achieved with more Nb retained in solid solution after the CASTRIP process. In addition, it is important to note that on the run-out-table, the cooling rate and the coiling temperature can be used to control the retention of Nb in solid solution in the CASTRIP process. Therefore, in order to achieve ideal precipitation hardening performance, it is necessary to study the influence of cooling rate and coiling temperature on the Nb retention in UCS steel in CASTRIP process.

Some research works about the influence of cooling conditions on the precipitation hardening focused on how cooling rate and coiling temperature influence the diffusion time and diffusion rate of solute atom [1]. While only a small number of studies focused on major precipitation region of steel and pointed out that the precipitates were mainly produced in the phase transformation temperature range during cooling control process [2]. The aim of the present research is to investigate how the cooling rate and coiling temperature influence the Nb retention in UCS steel during the cooling control process, viewed from phase transformation temperature range where the precipitates are mainly produced.

2 Literature review

2.1 CASTRIP process

CASTRIP process is a revolutionary new twin-rolling technique for producing strip cast steel. It uses less energy, time and space compared to a conventional continuous casting process. It is important to note that the solidification of the CASTRIP process is very fast and the solidification can be finished within a fraction of a second. In contrast, the conventional casting solidification takes a few of minutes to finish. Ultra-Thin Cast Strip (UCS) products produced by the CASTRIP process have the yield strength levels from 380 MPa to 550 MPa and the thickness ranges from 0.9 mm to 1.5 mm [3]. It is difficult to use the conventional casting process to produce the steel with 0.9 mm thickness because the minimum strip thickness and maximum strip width are restricted by the maximum mill rolling load.

The Nucor Steel's CASTRIP facility in Indiana is the world's first commercial installation for producing UCS steel, which is shown in Figure 2.1 [3]. It is clear that the two rotating rolls to form two individual shells that are formed into continuous sheet at the roll nip. The size of the ladle is 110 metric tonnes and the ladle is used to feed a large conventional tundish and a smaller tundish or transition piece. The core nozzle between the casting rolls is used to deliver liquid metal to the metal pool. The casting rate ranges from 60 to 100 m/min. The hot rolling mill leads to a reduction of steel thickness in the range of 10 to 50%. There is water cooling section using air mist to control the cooling rate during austenite to ferrite phase transformation on the run-out-table.

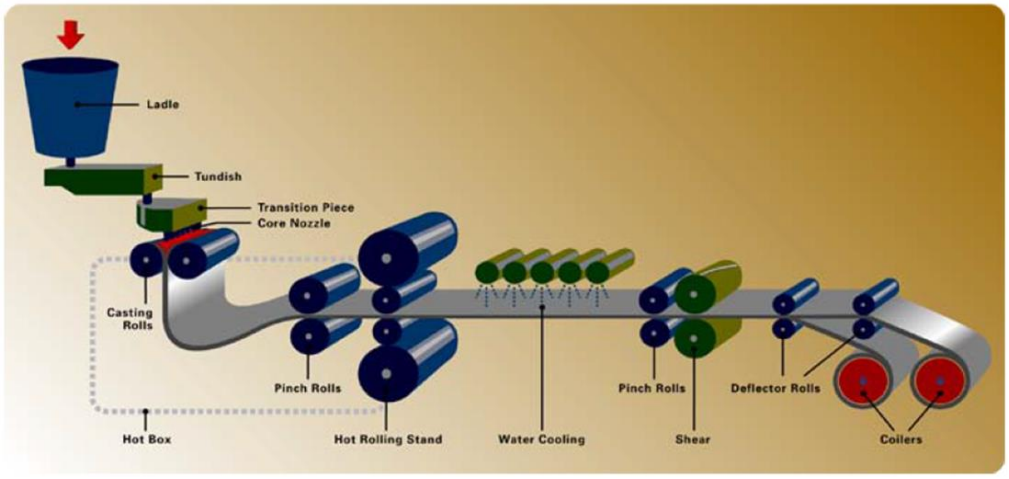

Figure 2.1 Main components of the CASTRIP process [3]

2.2 Microstructure and phase transformation of low carbon steel in CASTRIP Process

2.2.1 Microstructures and phase transformations in steel

2.2.1.1 Microstructures in steel

Figure 2.2 shows Fe-Fe_3C phase diagram [4]. As for pure iron, it is in the stable form called ferrite or α-iron at the room temperature and it has a body centred cubic (BCC) crystal structure. The pure iron has a face centred cubic (FCC) crystal structure known as austenite or γ-iron at the temperatures between 912^0C and 1394^0C and BCC crystal structure known as δ at the temperatures between 1394^0C and 1538^0C. Steel is basically iron carbon alloys and the solid solubilities of carbon are very different in α and γ iron as can be seen from Figure 2.2 that the maximum solubility of carbon in austenite is 2.14% which is much higher than 0.022% maximum solubility of carbon in ferrite. Therefore, cementite Fe_3C forms as the solubility limit of carbon in ferrite is exceeded below 727 ^{0}C which is the eutectoid temperature.

Ferrous alloys are mainly composed of iron with a small amount of carbon and other alloying elements. Normally, there are three types of ferrous alloys: iron, steel, and cast

iron. Commercially, the carbon content of pure iron is less than 0.008 wt%. The iron-carbon alloys that contain between 0.008 and 2.14 wt% C are classified as steels. Cast iron is classified as ferrous alloys that contain between 2.14 and 6.70 wt% C. Low carbon steel, the carbon content is between 0.008 and 0.25 wt%, can be classified into hypoeutectoid steel in which the carbon content is between 0.022 and 0.76 wt%. As for a hypoeutectoid steel, it can be seen from Figure 2.3 that at about 875^0C, the point c, the microstructure is entirely of γ grains [5]. With decreasing the temperature from the point c to the point d at about 775^0C, α particle nucleate along the original γ grain boundaries. The microstructure of steel consists of austenite and ferrite. Upon further cooling the steel from the point d to e, just above the 727^0C but still in the α+γ region, α particles grow larger and the fraction of the ferrite increases. As the temperature is lowered to the point f, below 727^0C, there is no change in the pro-eutectoid α phase and the remaining γ eutectoid transform alternating α and cementite (Fe_3C) plates and this microstructure is known as pearlite. The microstructure of the steel at room temperature consists of a continuous ferrite matrix surrounding the isolated pearlite colonies as shown in Figure 2.3. The ferrite formed in the pearlite is called eutectoid ferrite, while the ferrite formed before 727^0C is called proeutectoid ferrite or α.

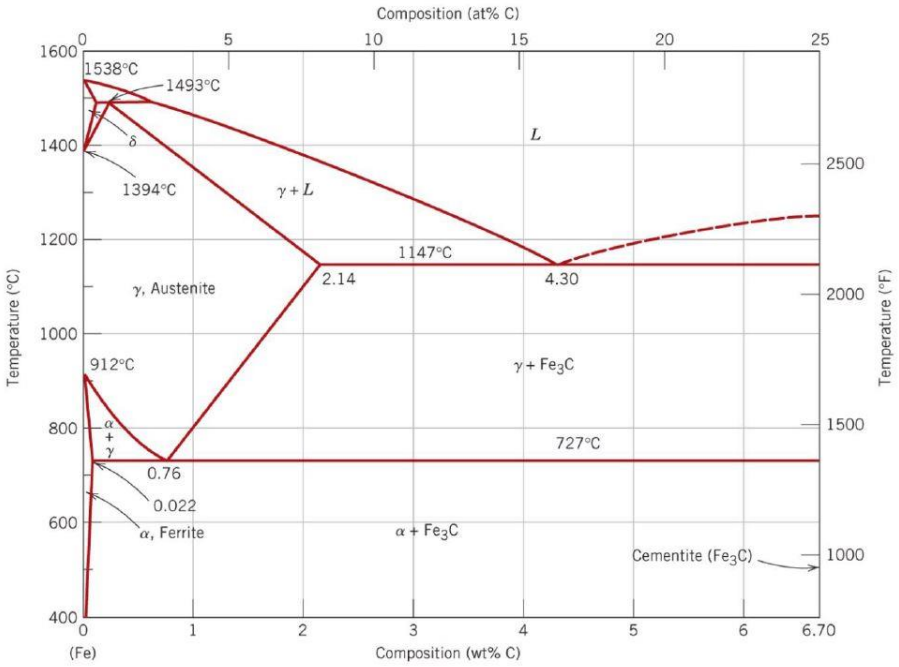

Figure 2.2 Fe-Fe3C phase diagram [4]

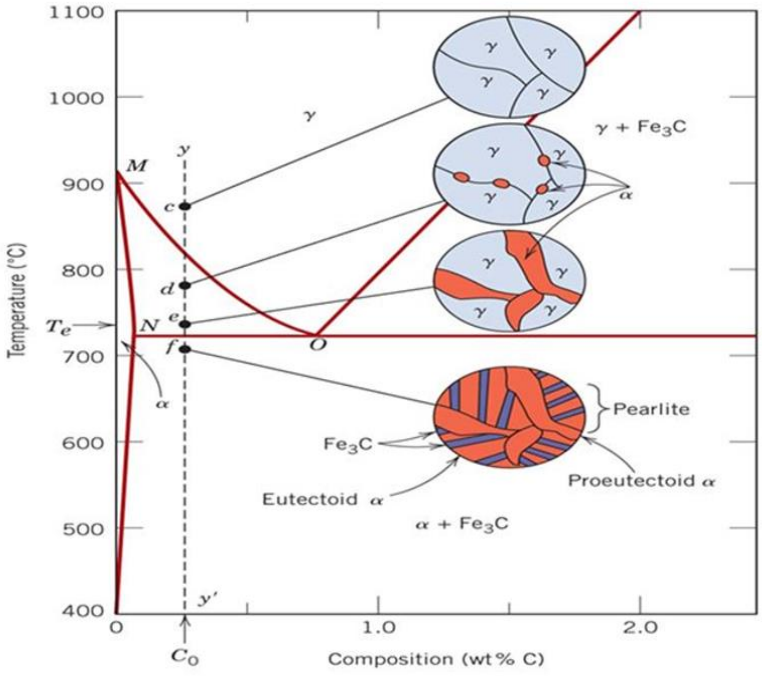

Figure 2.3 Schematic representations of the microstructures for an iron-carbon alloy (containing less than 0.76wt%C), as it is cooled from within the austenite phase region to below the eutectoid temperature [5]

In pearlite, the spacing between α and Fe_3C plates varies from grain to grain, some pearlite appears dark because the many close-spaced layers are unresolved at the magnification of the optical micrograph. The formation of pearlite is illustrated in Figure 2.4 [5]. The arrows indicate the directions of carbon diffusion and the carbon atoms diffuse away from the ferrite region to the cementite layers as the pearlite extends from the grain boundary into the unreacted austenite grain.

Eutectoid reaction happens at the eutectoid reaction point where solid austenite of 0.8 percent C produces **α** ferrite with 0.02 percent C and Fe_3C (cementite) that contains 6.67 percent C. This reaction can be written as below:

$$\gamma \text{ austenite } (0.8\%C) \xrightarrow{727^0C} \alpha \text{ ferrite}(0.02\%C) + Fe_3C\ (6.67\%C) \qquad (2\text{-}1)$$

where 727^0C is called eutectoid temperature and the α ferrite in the pearlite is called eutectoid ferrite after eutectoid reaction.

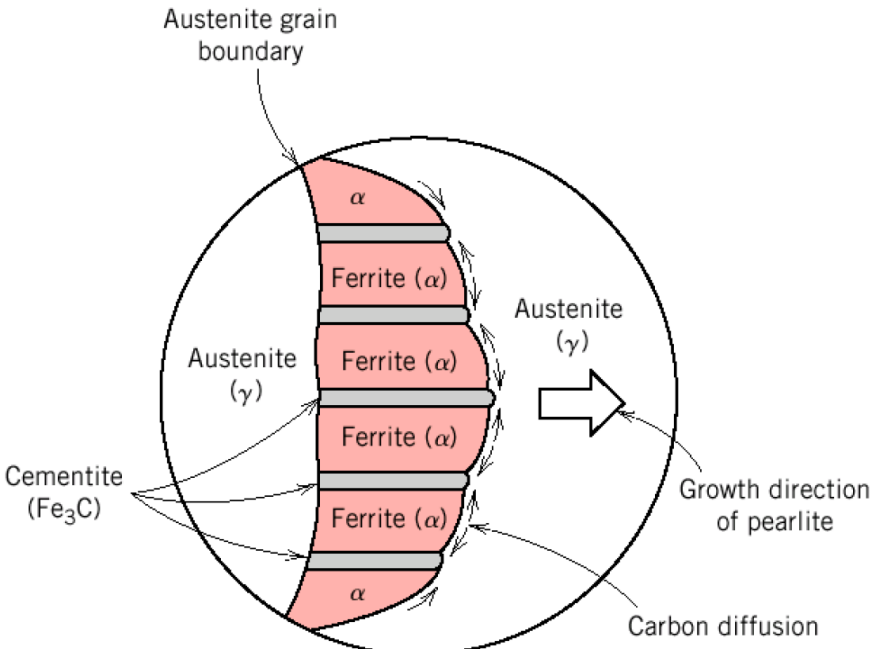

Figure 2.4 Schematic representation of the formation of pearlite from austenite; direction of carbon diffusion indicated by arrows [5]

Apart from the pearlite, bainite and martensite are also products of the austenitic transformation. Bainite consists of ferrite and cementite phases, for this reason, diffusional processes are involved in its formation. The shape of bainite is needles or plates, depending on the temperature of the transformation. An electron microscope is used to observe the microstructure of bainite due to the fine grain size of bainite as shown in Figure 2.5 [6]. There are two types of bainite structures based on microstructure observed on a light optical microscope: upper bainite and lower bainite which form in higher and lower temperatures respectively [7]. The upper bainte forms in the temperature range below the pearlite formation temperatures, typically below 500^0C. The upper bainite has a feather-like morphology as shown in Figure 2.5. The upper bainite is acicular and grows from austenite grain boundaries in the form of needles or laths. The lower bainite has finer plate-like grains compared to the upper

bainite and nucleates at austenite grain boundaries as well as within grain interiors as shown in Figure 2.6 [8]. Figure 2.7 shows that the difference between the upper bainite and lower bainite lies in the fact that carbide precipitates in the upper bainite are at the ferrite and austenite interphase boundaries i.e. an inter-lath dispersion and carbides in the lower bainite are contained within the ferrite grains [9]. The formation mechanisms of the upper and lower bainites are illustrated schematically in Figure 2.8 [10]. It can be seen that the plate like ferrite grain nucleates at grain boundaries and the reaction progresses further by the nucleation of new plates known as sub-units, which results in a sheaf-like structure.

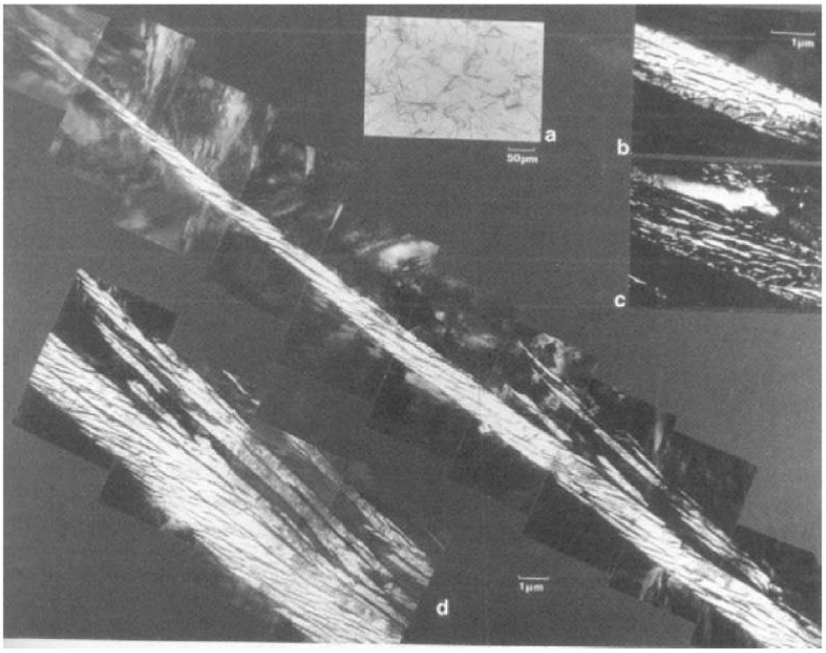

Figure 2.5 Microstructure of a sheaf of upper bainite [6]

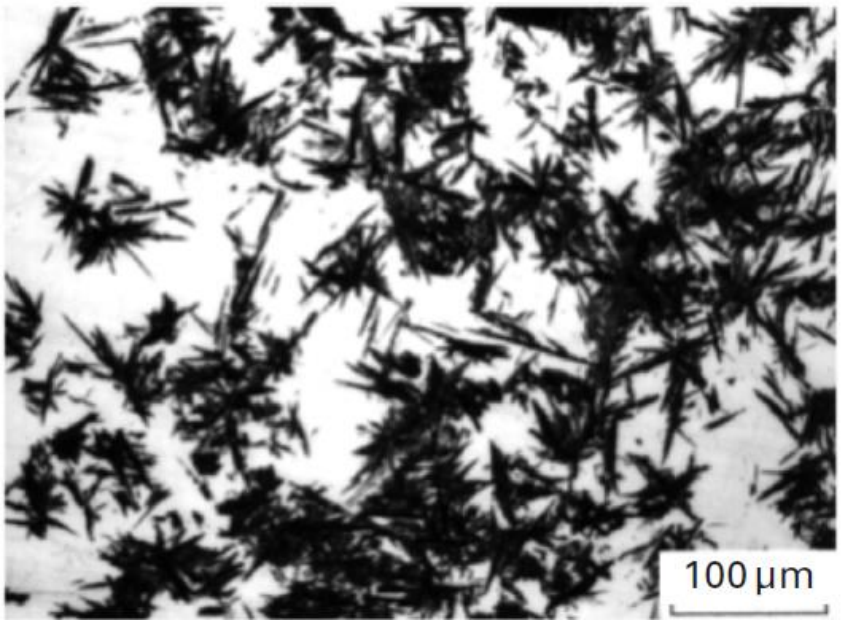

Figure 2.6 Optical micrograph of bainite microstructures in Fe-Ni-C alloys [8]

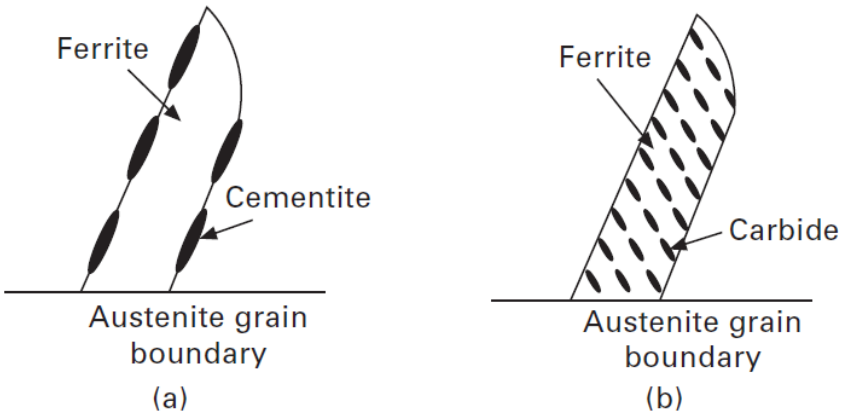

Figure 2.7 Classification of bainite based upon carbide precipitation: (a) upper bainite, (b) lower bainite [9]

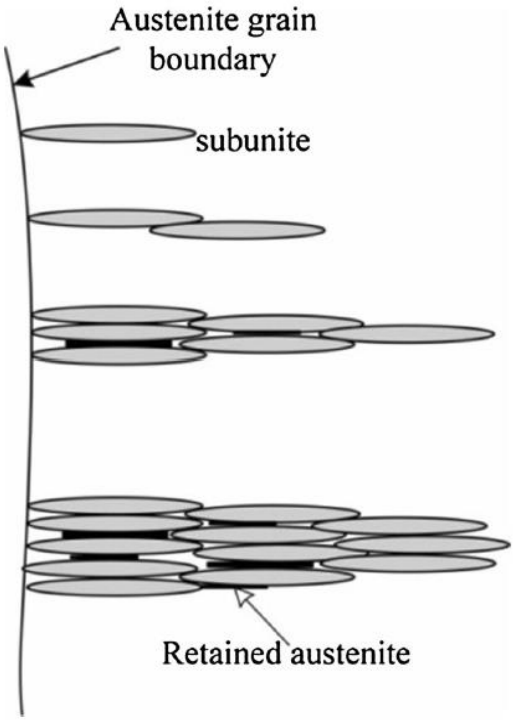

Figure 2.8 Schematic representation of formation of a bainite sheaf by repeated nucleation and limited growth of sub-units and its effect on overall transformation kinetics [10]

Martensite is formed in carbon steel by the rapid cooling of austenite to room temperature at such a high rate that carbon atoms do not have time to diffuse out of the crystal structure in large enough quantities to form cementitie (Fe_3C). As a result, the face-centered-cubic austenite transforms to a highly strained body-centered tetragonal form called matensite that is supersaturated with carbon. The shape of matensite is either lath bundles (low carbon) or plate like (high carbon) as shown in Figure 2.9 [11]. It is the hardest, strongest and the most brittle microstructure compared to other microstructures produced for a given steel alloy. These properties are attributed to the effectiveness of the interstitial carbon atoms in hindering dislocation motion and to the relatively few slip systems for the BCT structure of martensite.

Figure 2.9 Photomicrograph showing the martensitic microstructure. The needle-shape grains are the martensite phase, and the white regions are austenite that failed to transform during the rapid quench [11]

2.2.1.2 Microstructures in low carbon steel

There are many microstructures forming during the γ-α phase transformation of low carbon steel, including polygonal ferrite, acicular ferrite, pearlite and bainite.

Polygonal ferrite forms at the highest austenite transformation temperatures and slow cooling rate in a low-carbon steel. The nucleation site of the polygonal ferrite is austenite grain boundary and the ferrite grains grow away from austenite grain boundary to form equiaxed grains. A typical polygonal ferrite microstructure is shown in Figure 2.10 [12]. It is clear that polygonal ferrite grains are smooth, reflect light and appear bright and are separated by continuous, linear boundaries.

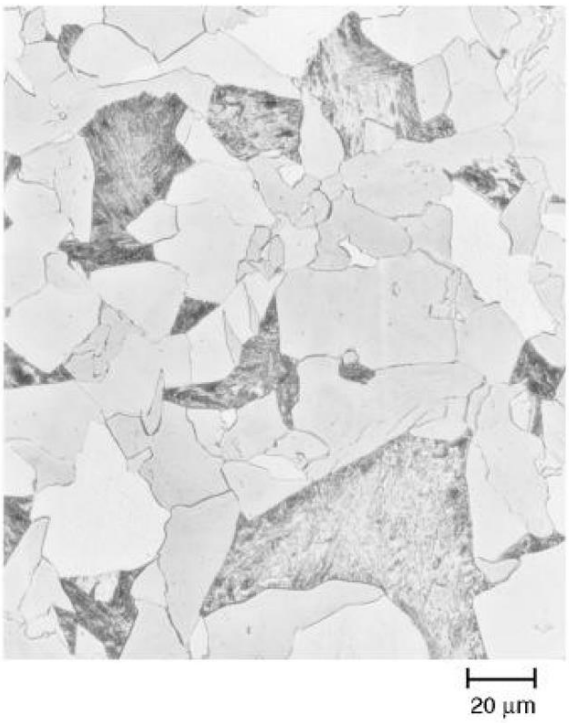

Figure 2.10 Polygonal ferrite formed in HSLA-80 steel isothermally transformed at 675 C (1250 F) for 500 s. Martensite (dark structure) has formed during cooling in austenite untransformed after the isothermal hold. Light micrograph, nital etch [12]

Austenite transforms into much finer ferrite crystals than polygonal ferrite at a high cooling rate and morphology changes from equiaxed to acicular and it is known as acicular ferrite. A typical acicular ferrite is shown in Figure 2.11 [13]. Normally, the nucleation site of acicular ferrite is inclusion within austenite and the grain of acicular ferrite forms in nonparallel arrays within austenite grains. An important characteristic of the acicular ferrite is that there is a high density of dislocations within the acicular ferrite grains, which together with small grain size and high angle grain boundaries give the acicular ferrite high hardness and toughness [14-17].

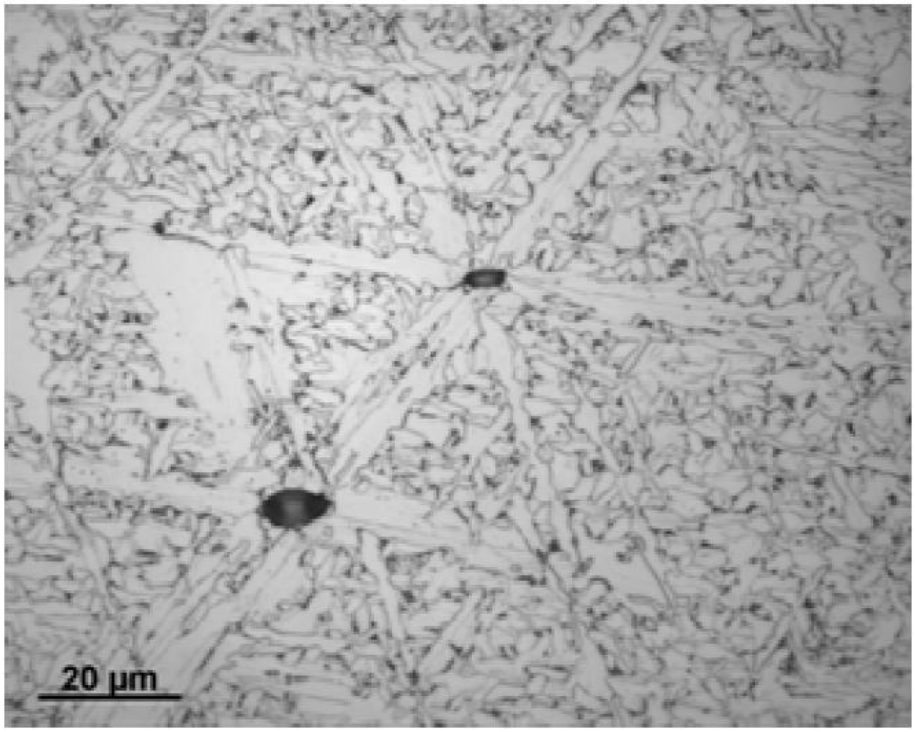

Figure 2.11 Micrographs of recent UCS steels, where shows acicular ferrite nucleating at two non-metallic inclusions [13]

Pearlite is composed of alternate closely spaced platelets or lamellae of ferrite and cementitie as shown in Figure 2.12 [18]. The pearlite nucleates heterogeneously on prior austenite grain boundary as shown in Figure 2.13 [11]. It has to be noted that the pearlite is formed at a fairly slow cooling rate in low carbon steel during cooling in CASTRIP process, which can be seen from CCT diagram shown in Figure 2.14 [19].

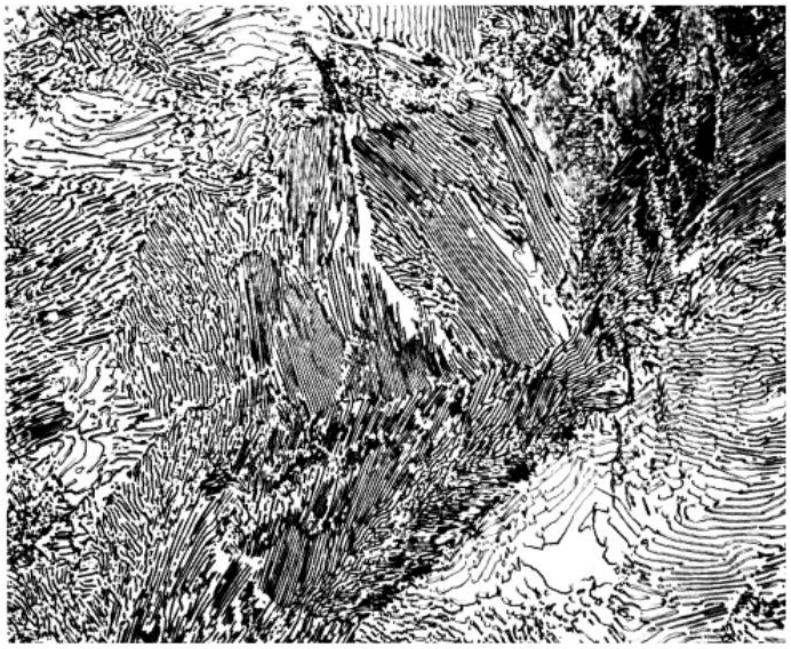

Figure 2.12 Pearlite in a furnace-cooled Fe-0.75C alloy. Picral etch. Original magnification at 500. Courtesy of A.R. Marder and A. Benscoter, Bethlehem Steel Corp., Beth-lehem, PA [18]

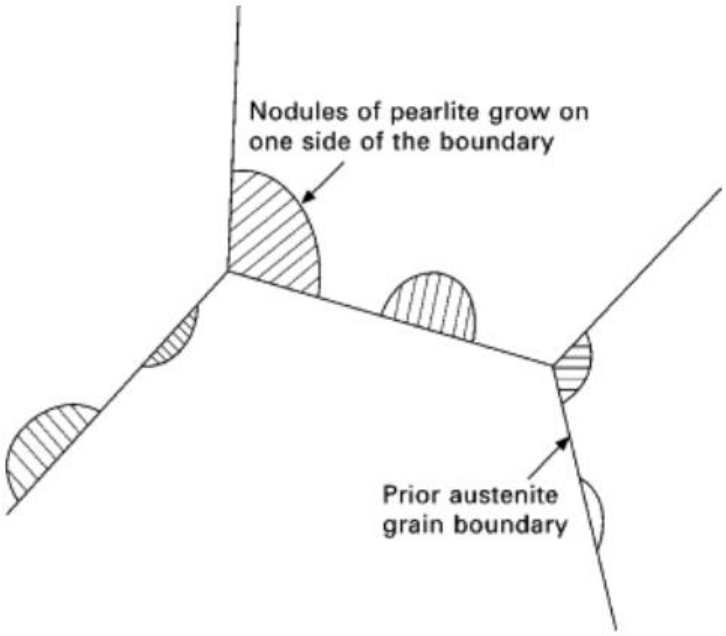

Figure 2.13 Schematic diagram which indicates that pearlite grows as nodules on one side of the prior austenite boundaries and at grain corners [11]

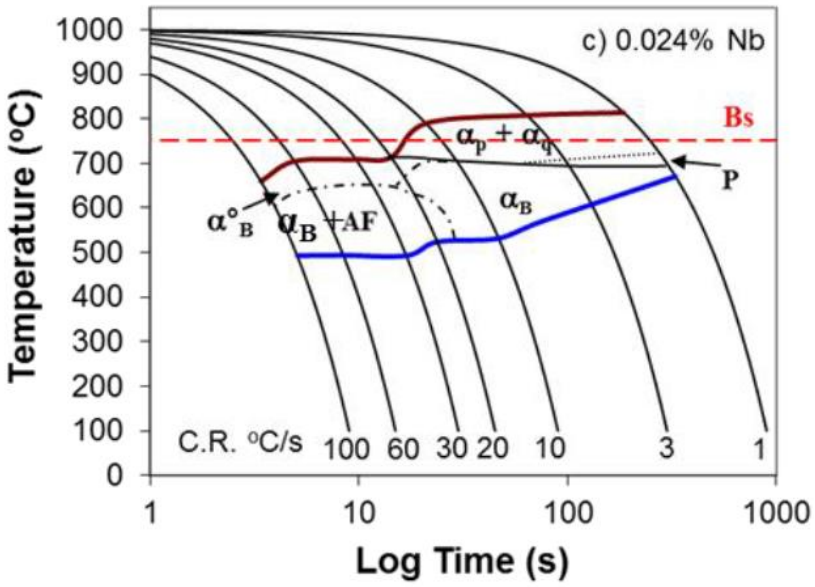

Figure 2.14 CCT diagram for UCS steel with 0.024% Nb [19]

Since the bainitic ferrite forms in the much lower temperatures than the polygonal ferrite, they are much finer than the polygonal ferrite. The elongated shape of the ferrite is referred to as α_B° and bainitic ferrite is defined as sheaf-like with laths but no carbide, conserving the prior γ-grain boundary, generally enough dislocated in the ISIJ system [20-23]. Granular ferrite, which is referred to as α_B in the ISIJ system, has many similarities to the bainitic ferrite as shown in Figure 2.15 [24]. The microstructure of the granular bainite consists of islands of retained austenite that may reveal austenite grain boundary as a result of an etching. The grain of the granular ferrite is quite fine and contains a high density of dislocations. In addition, the grain boundaries of granular ferrite are low angle grain boundaries [20, 25-26].

Figure 2.15 Granular ferrite formed by continuous cooling of a low carbon steel. Nital etch, light micrograph. Courtesy of B. Kloberdanz, Colorado School of Mines [24]

2.2.1.3 Phase transformations in steel

Fe-Fe_3C phase diagram is time-invariant diagram, in contrast**,** time-temperature-transformation (TTT) and continuous-cooling-transformation (CCT) diagrams are time–variant diagrams, which allow prediction of the microstructure after some period or constant-temperature and continuous-cooling heat treatment. Time-temperature-transformation (TTT) diagram shows the transformation of austenite to various ferrites, pearlite and martensite as a function of time at a constant temperature. TTT diagram is mapped by metallographic examination of series of specimens held for various times at various temperatures combined with dilatometry. Figure 2.16 shows how an isothermal transformation diagram is generated from percentage transformation-versus-logarithm

of time measurements [5]. In Figure 2.16, the vertical and horizontal axes are temperature and logarithm of time respectively. There are two solid curves in TTT diagram: one is the time required at each temperature for the initiation or start of the transformation and the other is for the transformation conclusion. The dashed curve means that 50% of transformation has completed. These curves were obtained from a series of plots of the percentage transformation versus the logarithm of time taken over a range of temperatures. The S-shaped curve in the upper portion of Figure 2.16 shows how a time temperature transformation diagram (bottom) is generated from percentage transformation-versus-logarithm of time measurements. As for the TTT diagram, it is clear to see from Figure 2.16 that only austenite exists above a horizontal line which indicates eutectoid temperature (727°C). Austenite will transform to pearlite as the alloy is supercooled to the temperature below the eutectoid temperature. The start and finish curves are nearly parallel, only austenite is present to the left of the transformation start curve, while only pearlite exists to the right of the finish curve. The isothermal transformation diagram for a eutectoid iron-carbon alloy is shown in Figure 2.17 [5]. The near-vertical line AB indicates the very rapid cooling of austenite to a given temperature. The horizontal segment BCD represents the isothermal treatment at this temperature. Austenite starts to transform to ferrite at point C and austenite finishes transformation to ferrite and cementite at point D. Figure 2.17 also shows schematic microstructures at various times during the progression of the reaction.

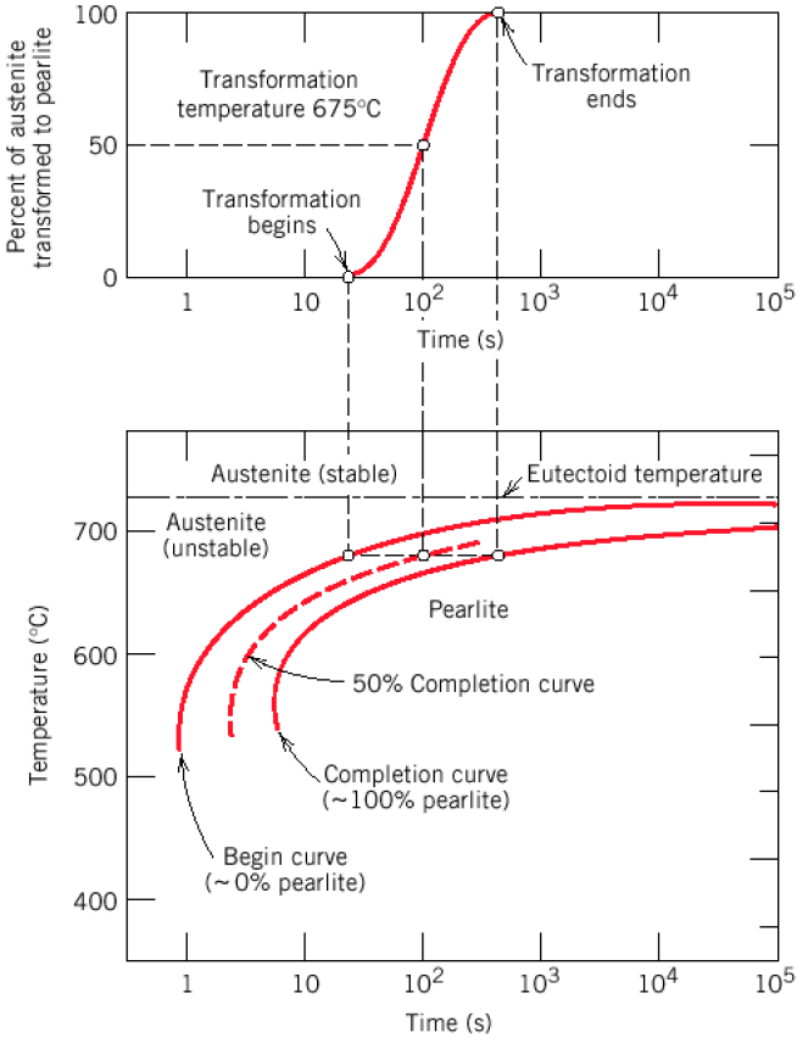

Figure 2.16 Demonstration of how a time temperature transformation diagram (bottom) is generated from percentage transformation-versus-logarithm of time measurements (top) [5]

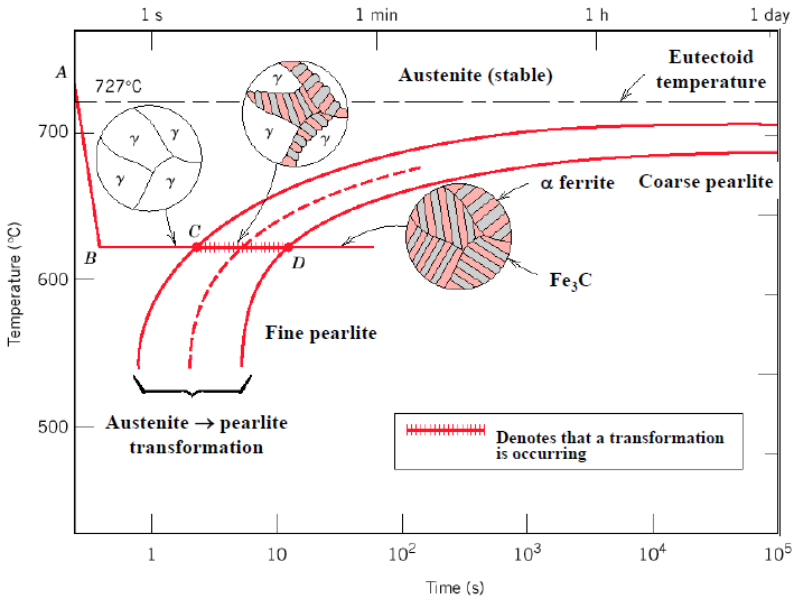

Figure 2.17 Isothermal transformation diagram for a eutectoid iron-carbon alloy, with superimposed isothermal heat treatment curve Microstructures before, during, and after the austenite-to-pearlite transformation are shown [5]

Figure 2.18 shows that austenite of eutectoid steel is rapidly cooled to temperatures below the eutectoid temperature and then isothermally transformed [5]. It can be seen from Figure 2.18 that pearlite is produced in the steel at a higher holding temperature and at a lower holding temperature, bainte may be produced. Apart from the holding temperature, holding time also plays an important role in the phase transformation of steel. If the steel is rapidly cooled to a relatively low temperature, austenite will transform completely to martensite, because there is no sufficient time at the hold temperature for any diffusion controlled transformation. However, if the steel is held for a longer time at a given high temperature and then quenched, the austenite may transform to ferrite, cementite, pearlite or baintie, depending on the holding temperature.

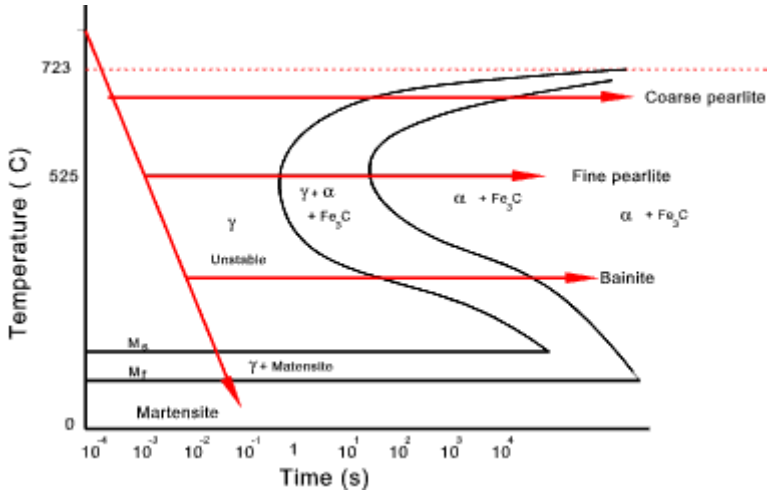

Figure 2.18 The complete time temperature transformation diagram for an iron-carbon alloy of eutectoid composition [5]

Isothermal heat treatment is not easy to put into practice because steel needs to be rapidly cooled to and maintained at an elevated temperature from a higher temperature above the eutectoid. However, most heat treatments for steels involve the continuous cooling of a specimen to room temperature. Therefore, continuous-cooling transformation (CCT) diagram is used to represent which types of phase changes will occur in a material as it is cooled at different rates. The influence of cooling rate on phase transformation for low carbon steel is shown in Figure 2.19 [19]. It can be seen that between 1 and 3°C/s cooling rates, pearlite and polygonal ferrite are produced. With increasing the cooling rate, between 3 and 20°C/s, there were no pearlite but polygonal ferrite and bainite produced. Upon further increasing cooling rate, polygonal ferrite was no longer produced after 20°C/s cooling rate, instead, bainitic ferrite and acicular ferrite were produced. The further explanation of polygonal ferrite, pearlite and bainte can be seen from Table 2.1 [25].

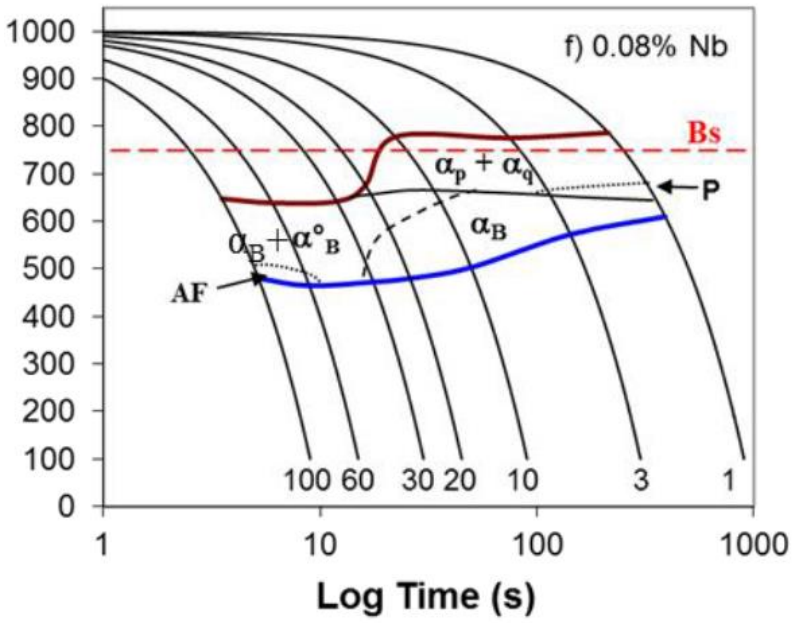

Figure 2.19 CCT diagrams for the low carbon steel with 0.08% Nb [19]

Table 2.1 ISIJ Transformation Products Nomenclature and Classification[25]

Symbol	Nomenclature	Characteristics—Major Matrix phases
α_p	Polygonal Ferrite	Equiaxed, polyhedral shaped, mostly recrystallized
α_q	Quasi-polygonal α	Irregular changeful shape, formed at lower temperature crossing over γ-grain boundary, mostly recovered
α_w	Widmanstätten α	Characteristic lath/plate-like shape; not usual in very low-C steels, mostly recovered
α_B (Zw)	(Granular bainitic) α	Granular bainitic ferritic Zw structure; dislocated substructure but fairly recovered like "lath-less"
α_B°	Bainitic Ferrite	Sheaf-like with laths but no carbide; conserving the prior γ-grain boundary, generally enough dislocated
Minor Secondary Phases		C-enriched and scattered in Islands or films
P	Pearlite	Eutectoidal reaction product

2.2.1.4 Dilatometry in phase transformation determination

2.2.1.4.1 Introduction of thermal expansion measurement

Thermal expansion is the tendency of matter to change in shape, area and volume to change in temperature through heat transfer. There are many methods to measure thermal expansion of solid. All methods can be divided into two classes: (1) relative methods where the expansion of solids is measured relative to the expansion of another material; (2) methods where the expansion of solids is measured directly. Early measurement of thermal expansion of solids is in 18th century, Musschebrock measured the expansion of a horizontally mounted specimen and the heat was provided by candles placed beneath the specimen [27]. It has to be noted that a major breakthrough of thermal expansion measurement was achieved in 1927. Becker successfully used X-rays to measure thermal expansion and it became possible to measure thermal expansion of solid directly [28]. Computer and laser technologies began to use in thermal expansion measurement in the late nineteenth century. For instance, sensitivities of 10^{-9} in solid expansion can be obtained by using lasers and computer controlled data acquisition systems were also used to measure a specimen during a rapid temperature change [29-30]. Nowadays, computer and laser technologies are widely used in dilatometry which is a method to measure thermal expansion of solid.

2.2.1.4.2 Application of dilatometry

The industrial application of the steels is due to their mechanical properties which are influenced by the microstructure of the steels. Therefore, it is very important to study the microstructure change during heat treatment. Dilatometry is a thermos-analytical method to study the solid-solid phase transformation in steels during heat treatment and it can be used to reveal the relationship between the temperature and the phase

transformation in terms of dimensional changes in the sample during heat treatment. The dilatometry can be used in phase transformation study because the volume of the steel changes during the phase transformation. Dilatometer is typical equipment for dilatometry analysis. Results obtained from a dilatometer are presented as a graphical form which shows the formation temperatures of microstructural constitute of the steel during heat treatment as shown in Figure 2.20 [31]. These transformation diagrams have great value in metallurgical applications such as heat treatment and welding.

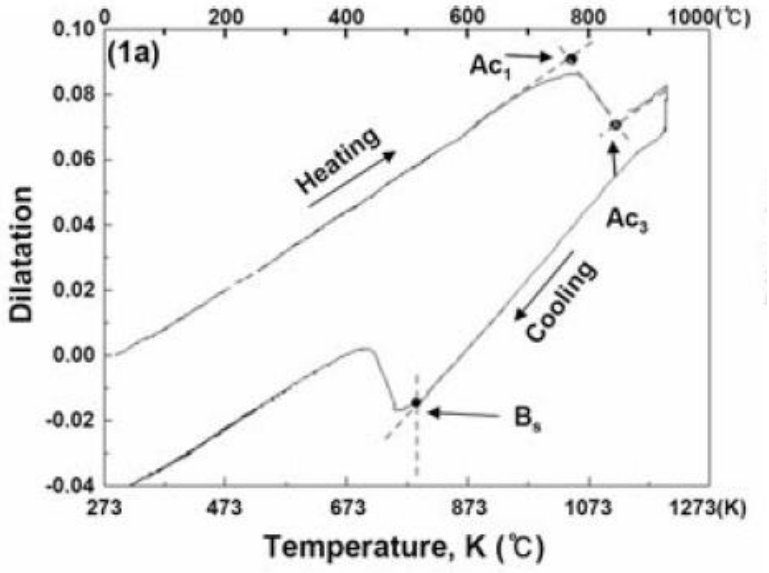

Figure 2.20 Dilatation curve obtained at 1 K/s cooling rate for Ultrahigh-Thickness Cr-Mo Steel [31]

2.2.1.4.3 Dilatometer and dilatation curve

Dilatometer is an instrument which can be used to measure expansion and contraction of solid during the heat treatment and determine the phase transition occurring with the change of temperature for the steel during heat treatment. A typical dilatometer is illustrated schematically in Figure 2.21 where the sample is contained in a heating

device [32]. There is a rod on the right of the sample which is used to measure the length changes due to compression or expansion of the sample and the temperature of the sample is also measured by the thermocouple which is a temperature sensor.

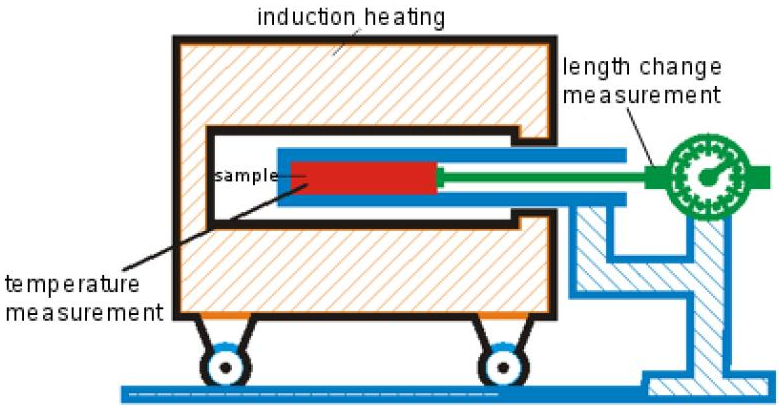

Figure 2.21 Sketch of the dilatometer experiment [32]

Normally, the results are shown in a dilatation curve where the length change is plotted as a function of the temperature. The data from dilatation curve is used to map Continuous-Cooling-Transformation (CCT) diagram. A heating dilatation curve of the low carbon steel is illustrated in Figure 2.22 [33]. The initial microstructure of the steel is ferrite and pearlite. It is clear from Figure 2.22 that the relative change in length of the steel increases in direct proportion to temperature due to thermal expansion as the temperature increased from 500°C to Ac_1. Ferrite begins to transform to austenite at Ac_1. The α-γ transformation during heating is accompanied by an atomic volume change of approximately 1%, which is associated with a significant contraction on the heating dilatation curve [34]. Therefore, upon further increasing the temperature to Ac_3, ferrite transforms into austenite and the relative change in length of the steel is no longer proportion to the temperature. Ferrite stops transforming into austenite at Ac_3. After phase transformation, the relative change in length of the steel increases in direct proportion to temperature again. Heating dilatation can not only show the α-γ phase

transformation, but also can reveal the carbide dissolution process. Figure 2.23 shows the heating dilatation curve response of α-γ transformation and the carbide dissolution process [33]. The solubility of carbide in austenite is larger than that in ferrite, therefore, lots of carbide will dissolve into austenite after α-γ transformation. It is clear that above α-γ transformation finish temperature Ac_3, there is a continuous increase of slop in the curve that corresponds to the progressive dissolution of the carbides in austenite. After the carbides stop dissolving into austenite at Ac_c, a significant carbon concentration gradient is presented in austenite. Upon further increasing the temperature from Ac_c to Ac_h, the concentration in the austenite balances out by carbon and carbide-forming elements diffusion, reaching the homogeneity at temperature Ac_h. The carbides in the steel have significant influence on its property, therefore, the study of carbide dissolution process is important for the optimization of the steel. In this sense, dilatometric analysis plays an important role in determine the temperature where the carbides stop dissolving into austenite during continuous heating [35].

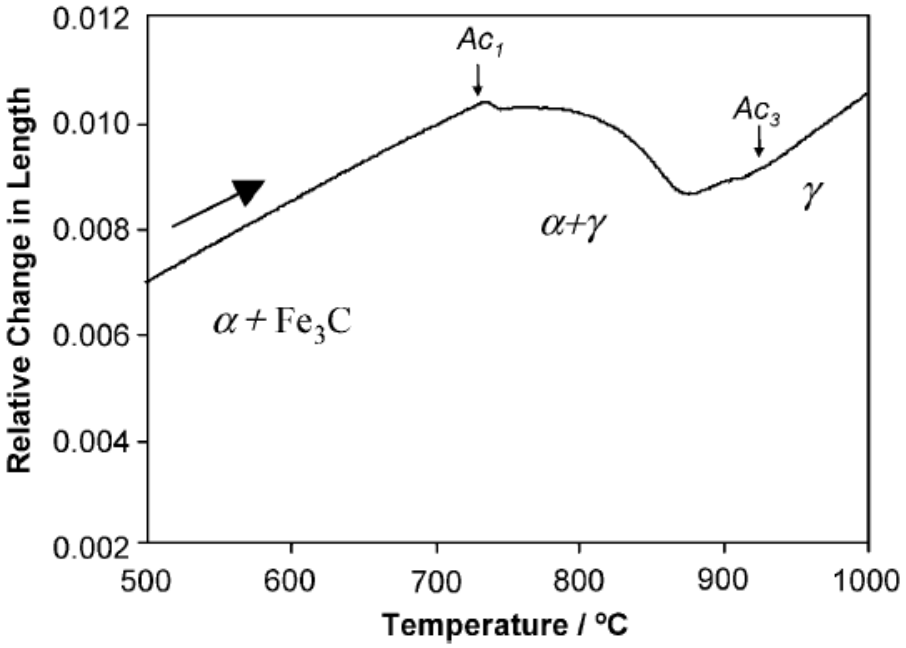

Figure 2.22 Heating dilatation curve of a low carbon steel (Fe–0.11C–0.50Mn) obtained at a heating rate of 0.05K s-1 [33]

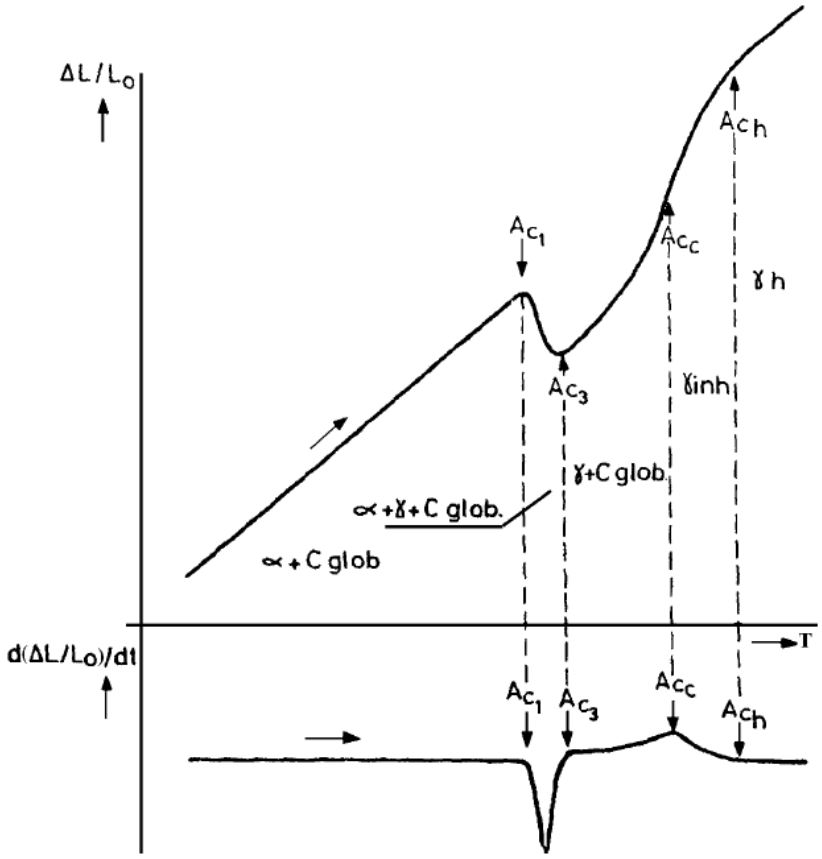

Figure 2.23 Diagram of the heating dilatation curve response of α-γ transformation and the carbide dissolution process of martensitic stainless steels [33]

Figure 2.24 is the cooling dilatation curve of a carbon manganese steel cooled at 1 K s^{-1} cooling rate, showing that austenite transforms into ferrite and bainite during continuous cooling [33]. Ar_3 and Ar_1 are the start and finish temperatures of austenite to ferrite and pearlite transformation. The austenite-to-pearlite transformation cannot show clearly in the dilatation curve due to a masking of the individual reactions by the continued growth of the other phase. Therefore, interrupted cooling by quenching experiments and subsequent metallographic examination is necessary to determine the pearlite transformation start and finish temperatures. Several quench temperatures are selected from cooling dilatation curve to study the austenite to ferrite and pearlite transformation process and the microstructures of the steel in different quench temperatures are shown in Figure 2.25 [33]. The phase transformation starts at Ar_3

shown in Figure 2.25 (b) and finishes at Ar_1 shown in Figure 2.25 (h). It is clear to see the intermediate stages of the reaction from Figure 2.25 (c-g). The dilatation curve deviates from linearity is due to the volume expansion related to the austenite to ferrite and bainte transformation.

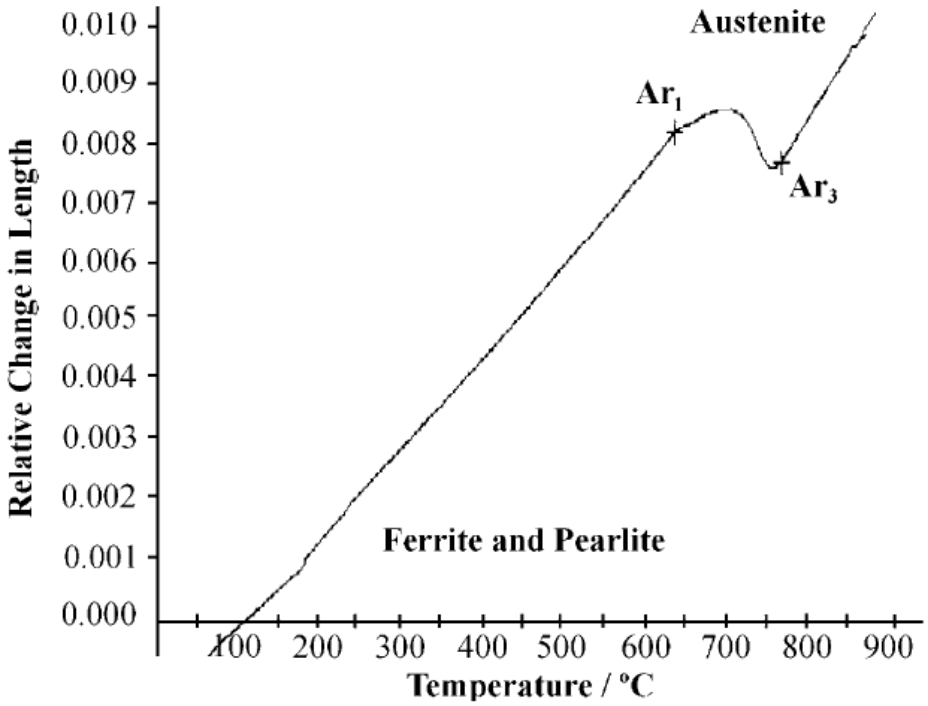

Figure 2.24 Cooling dilatation curve of a carbon manganese steel (Fe-0.20C-1.1Mn-0.34Si) obtained at a cooling of 1K s^{-1} [33]

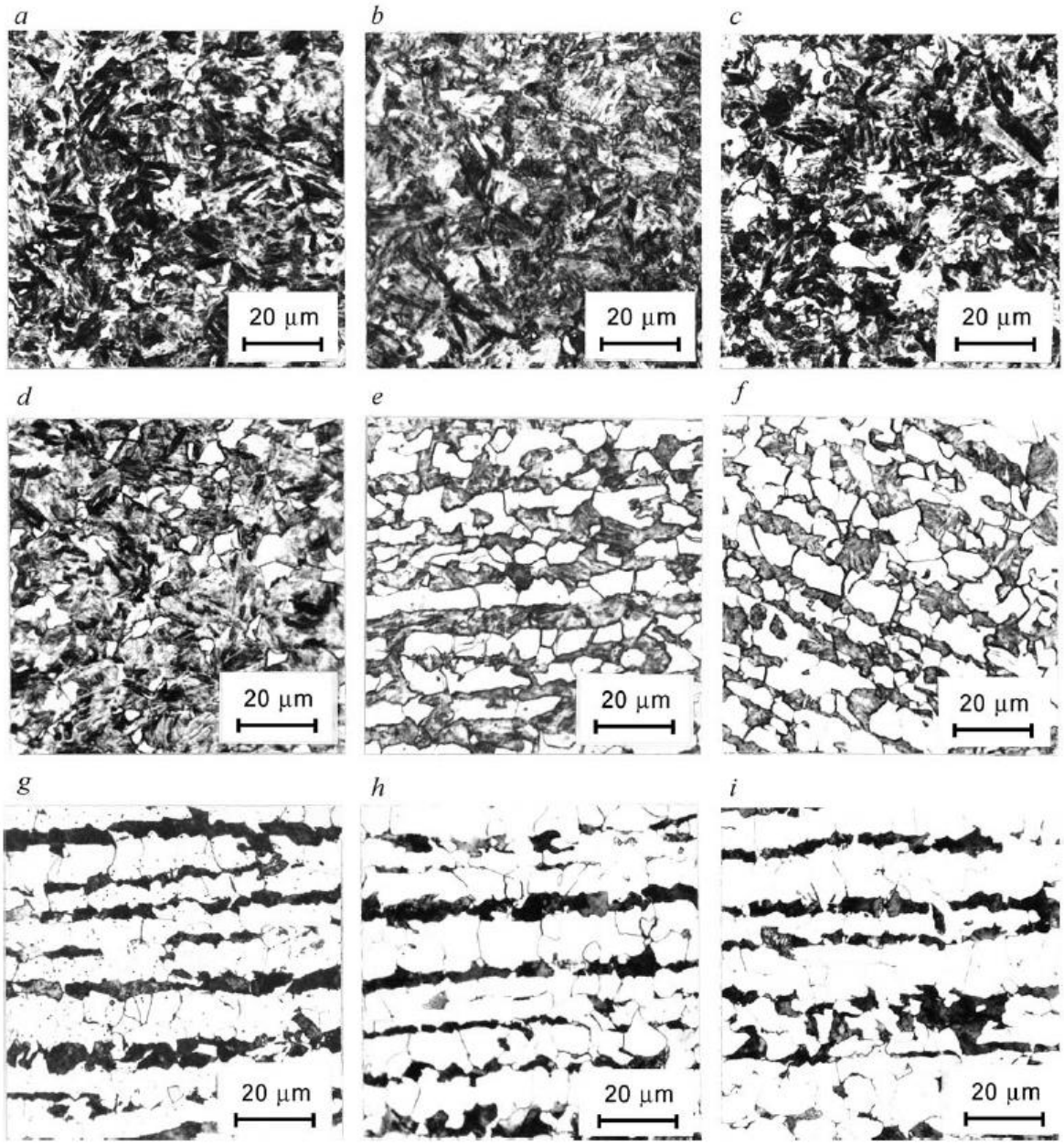

Figure 2.25 Optical micrographs corresponding to the evolution of ferrite and pearlite formation during cooling at a rate of 1 K s-1 in a carbon manganese steel (Fe– 0.20C–1.1Mn–0.34Si). Quench-out temperatures: (a) 765 °C; (b) 758°C (Ar3); (c) 754°C; (d)746 °; (e) 726°; (f) 676°; (g) 636°; (h) 626° (Ar_1); (i) room temperature [33]

In contrast, Figure 2.26 shows the cooling dilatation curve for a low carbon manganese steel cooled at fast cooling rate [33]. There are two phase transformations

during cooling. Austenite transforms into bainite at higher temperature and martensite at lower temperature. The dilatation curve deviates from linearity is due to the volume expansion related to the austenite-to-bainte transformation first and austenite-to-martensite transformation latter.

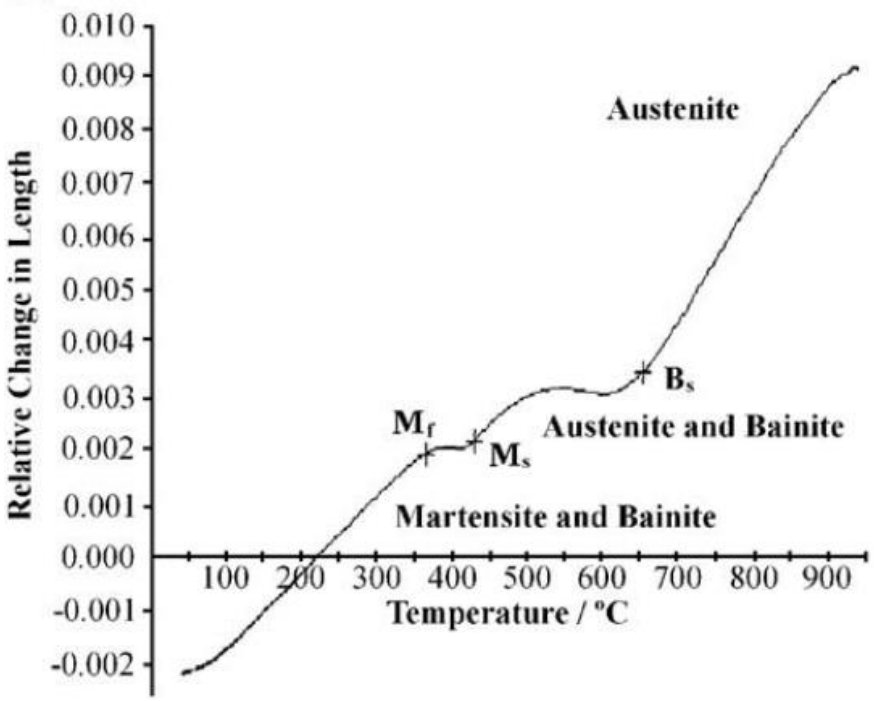

Figure 2.26 Cooling dilatometric curve and of a low carbon manganese steel (Fe – 0.07C–1.56Mn–0.41Si) after cooling at a rate of 234 K s-1 [33]

2.2.2 The influence of reheating temperature on γ-α phase transformation

Reheating process as a part of a thermos-mechanical control process plays an important role in γ-α phase transformation because it is related austenite grain size. It is can be seen from Figure 2.27 that the size of austenite increases with the increase of the reheating temperature and reheating time [36]. The size distribution of austenite becomes more homogeneously with the increase of the reheating time as shown in Figure 2.28 [37]. Therefore, a reheating process can be used to control the strength,

toughness and the final microstructure of the steel. It has been shown that a higher toughness of HSLA steel can be achieved by using a lower reheating temperature.

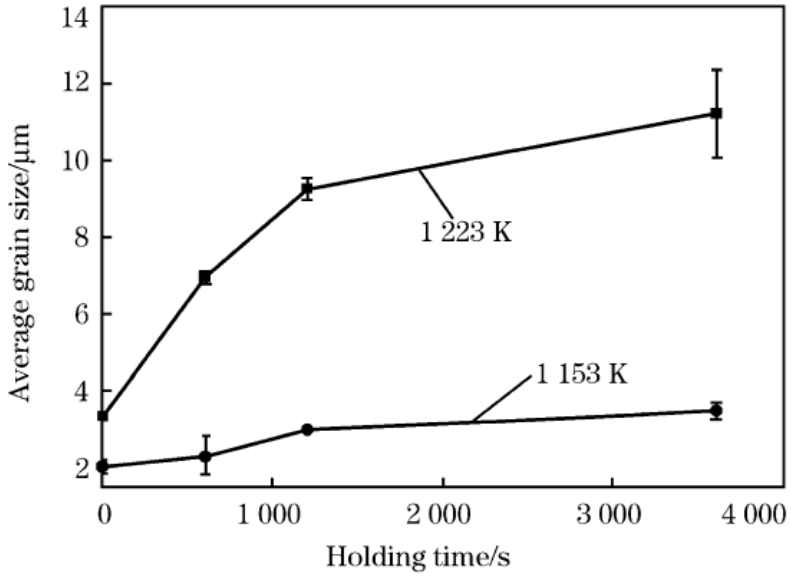

Figure 2.27 Variation of austenite grain size with holding time at reheating temperatures of 1153 and 1223 K [36]

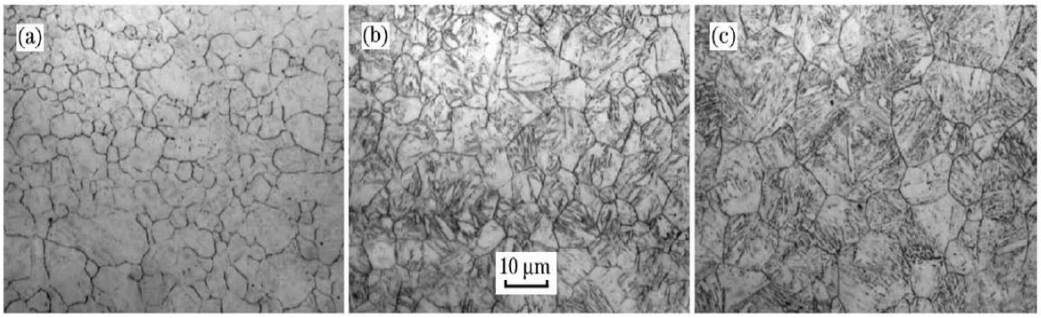

(a) 1 s; (b) 600 s; (c) 1200 s.

Figure 2.28 Effect of holding time on morphology of austenite grain at 1223 K [37]

2.2.3 The influence of hot rolling reduction on phase transformation of low carbon steel in CASTRIP process

Hot rolling reduction in CASTRIP process can be used to control not only austenite grain size but also austenite grain shape. Figure 2.29 shows the relationship between the hot rolling reduction and austenite grain size. It is clear that the austenite grain size decreases with the increase of the hot rolling reduction [13]. Apart from the austenite grain size, hot rolling reduction can also influence the austenite grain shape. S. Datta, who studied effect of thermomechanical processing on microstructure in low carbon steel, proposed that the prior austenite grain size becomes more elongated with higher hot rolling reduction [38].

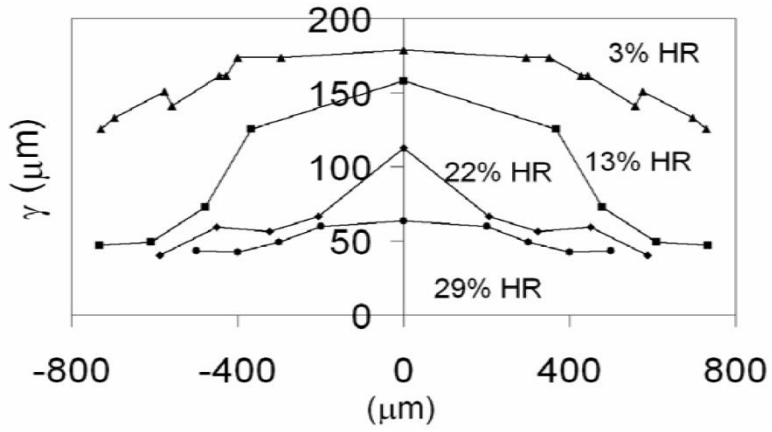

Figure 2.29 Effect of hot rolling reduction on austenite grain size measured through the thickness of a UCS strip. [13]

The formation of acicular ferrite and polygonal ferrite can also be influenced by hot rolling reduction. It has been reported that the number of acicular ferrite decreased with the increase of hot rolling reduction and the acicular ferrite was replaced by an

increased proportion of polygonal ferrite [13]. As previously mentioned, the size of austenite grain decreased with the increase of hot rolling reduction and more austenite grain boundaries were produced so that the nucleation sites of polygonal ferrite increased.

2.2.4 Effect of cooling rate and coiling temperature on γ-α phase transformation

Cooling rate as an important factor influencing the austenite to ferrite phase transformation can be controlled to get a desired property of UCS steel. It can be seen from Figure 2.30 that more polygonal ferrites are produced in the steel at 3°C/s cooling rate than that of the steel cooled at 60°C/s and the volume fraction of bainte gradually increases as the cooling rate increases from 3 to 60°C/s [19]. Therefore, the steel hardness increases with the increase of the cooling rate. The hardness as a function of cooling rate for the base and Nb UCS steel is illustrated in Figure 2.31[19].

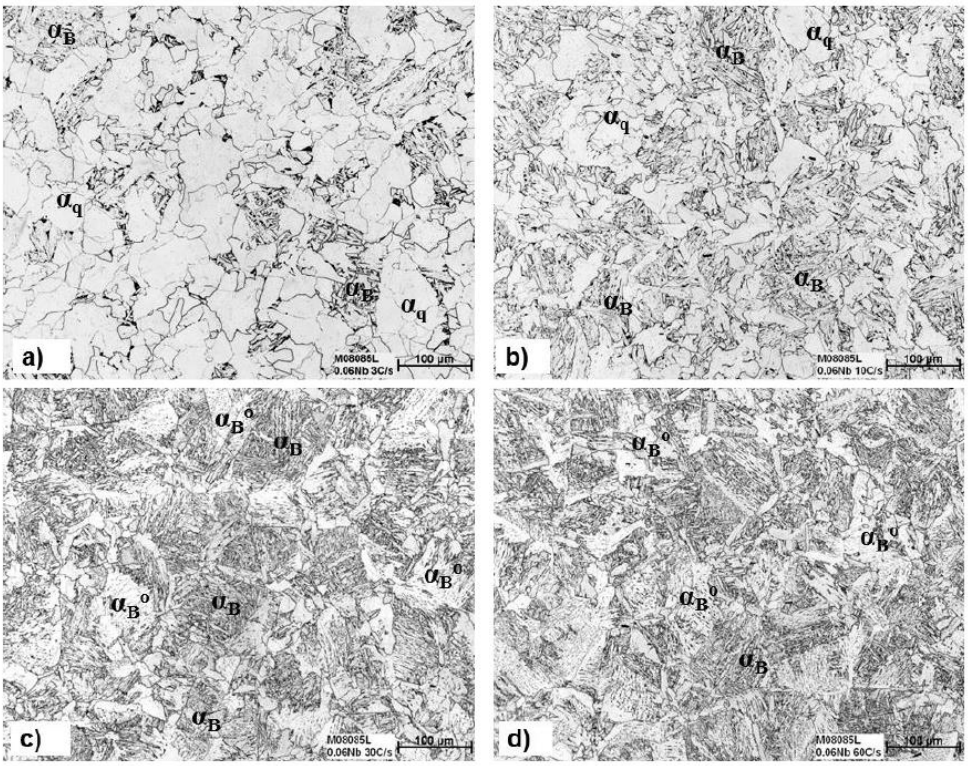

Figure 2.30 Optical microstructures for 0.06% Nb UCS flat dilatometer samples cooled at (a) 3 °C/s αq + αB, (b) 10 °C/s αq + αB + ~αB°, (c) 30 °C/s αB + αB°, and (d) 60 °C/s αB + αB° [19]

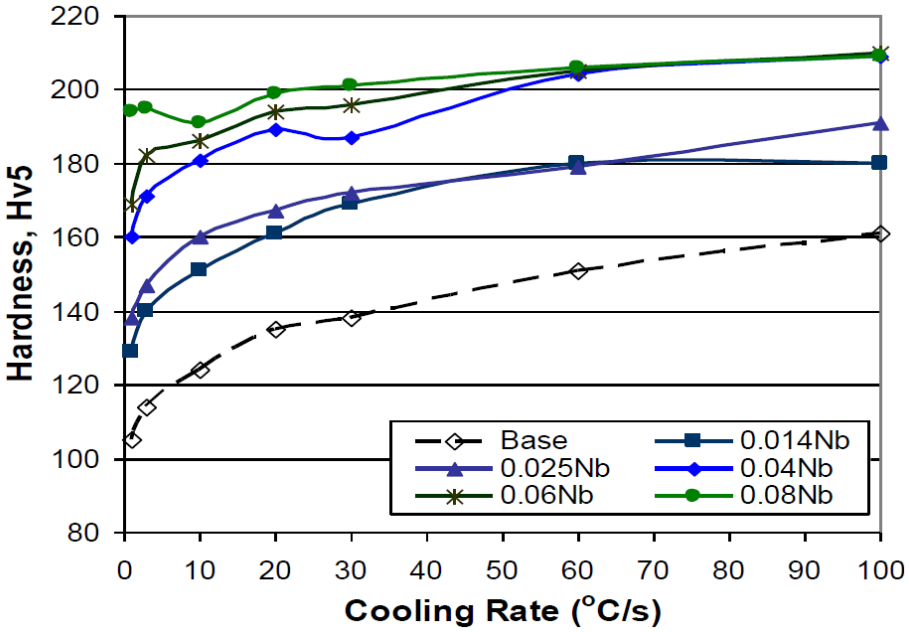

Figure 2.31 Vickers hardness, HV5, as a function of increasing cooling rate and increasing Nb addition [19]

Apart from the cooling rate, the coiling temperature can also influence on the austenite to ferrite phase transformation in the CASTRIP process. It is well known that the yield strength of HSLA steel increases with the decrease of the coiling temperature as shown in Figure 2.32 [13]. It is clear that the bainitic microstructure becomes coarser as the coiling temperature increases from 490 to 650°C. Therefore, the strength of steel decreases with the increase of the coiling temperature as shown in Figure 2.33 [13].

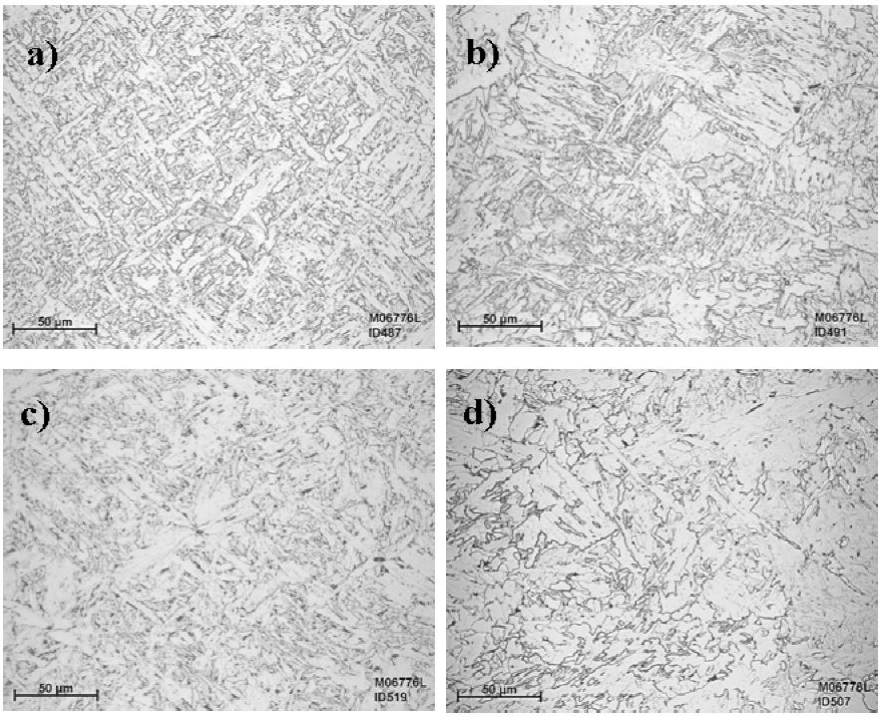

Figure 2.32 Microstructures for 0.024%Nb UCS steel at different coiling temperatures, a) 490ºC, b) 535ºC, c) 570ºC and d) 650ºC [13]

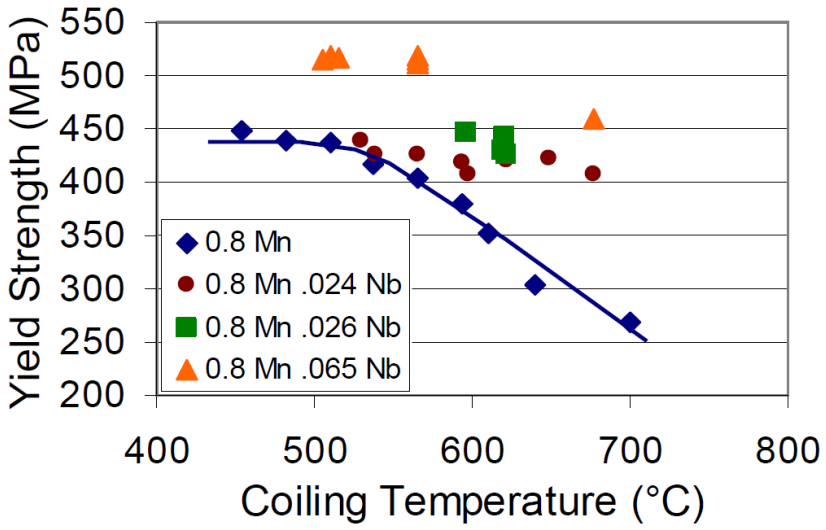

Figure 2.33 Effect of coiling temperature on yield strength of the C-Mn-Si base UCS steel and various Nb microalloyed UCS steels [13]

2.3 Precipitation hardening in HSLA steel

2.3.1 Introduction of precipitation hardening

Normally, precipitation hardening is composed of a solution heat treatment at a high temperature and a fast cooling from the solution temperature to room temperature followed by an age hardening heat treatment. The purpose of the high temperature solution heat treatment and quench to room temperature is to produce a supersaturated solid solution where an excessive number of solute atoms are retained in solid solution. In the age hardening heat treatment, the steel is heated to a given aging temperature and the excessive solute atoms segregate from the solid solution and form precipitates which can increase the hardness and strength of the steel. A typical precipitation hardening heat treatment is shown in Figure 2.34. Solid solubilities of Nb and C in steel increase with temperature as expected. However, more importantly, the solid solubilities of Nb and C are much higher in gamma iron than alpha iron. Some of the solubility products curves of NbC, Nb(CN) and other nitrides, carbides are shown in Figure 2.35 [39-44]. For this reason, a considerable amount of niobium and carbon is dissolved in steel during a reheating process. Then the steel is quenched from the solution treatment temperature to room temperature. The Nb and C remain in the solid solution of the steel because the fast cooling rate prevents the formation of NbC during the cooling. As a result the steel is now supersaturated with Nb and C. In the age hardening heat treatment, the excessive Nb and C in the supersaturated solid solution will precipitate out as NbC at grain boundaries and defects such as dislocations in the interior of grains. Finally, the steel is quenched from the aging temperature to room temperature. After the age hardening, the strength and hardness of the HSLA steel will increase and the ductility of steel decreases due to the precipitate produced from the age hardening heat treatment. It is believed that the precipitates produced at dislocation are the main factor for hardness increment of the age hardened steel.

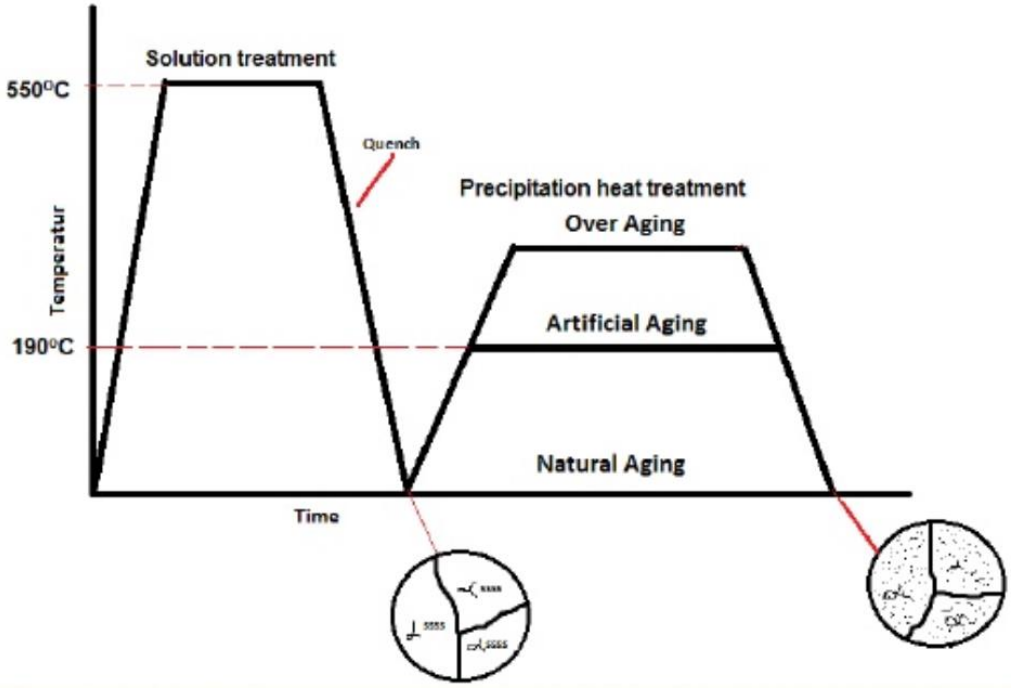

Figure 2.34 Schematic diagram of age hardening (www.slideshare.net)

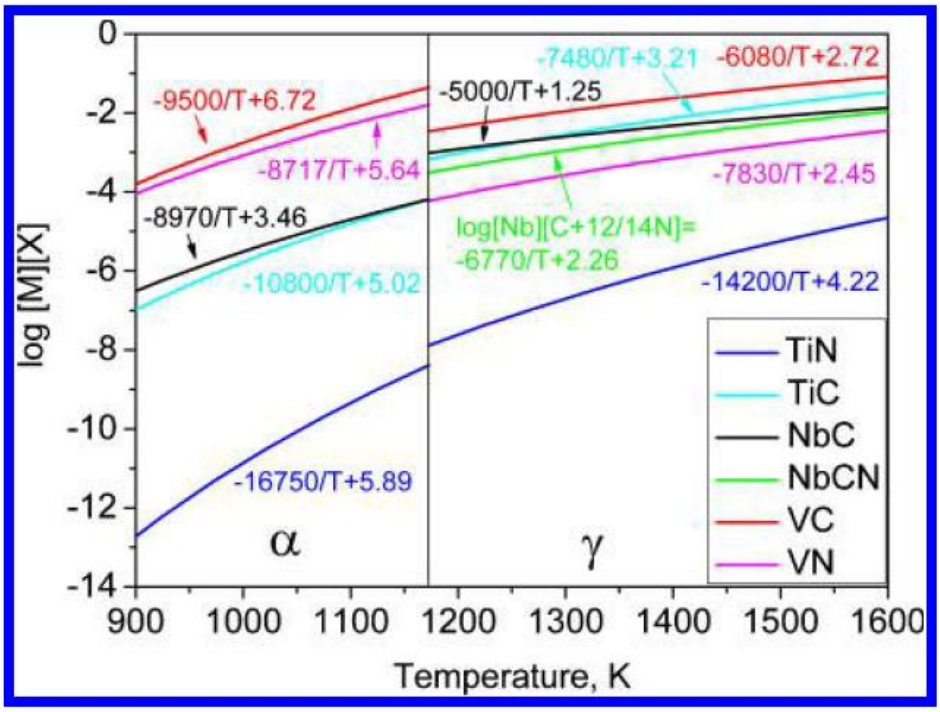

Figure 2.35 Solubility products of main precipitate species in HSLA steels [39-44]

The strengthening mechanisms of the precipitation hardening are grain refinement and dislocation hardening. Precipitates formed at grain boundaries can impede grain growth during a reheating and refine the final microstructure of the steel. Precipitates formed in the grain interior suppress the movement of dislocation and thus increase the strength of the steel. The effect of the precipitation hardening depends on many factors including the size, the number and the stability of the precipitates.

2.3.2 Analysis of precipitate in precipitation hardening

2.3.2.1 Introduction

Carbide forming elements such as Nb and V are used in the HSLA steel to form carbides, nitride or carbonitrides as precipitations hardening and grain refinement. Nucleation sites for these precipitates are grain boundaries, dislocations, deformation bands and other defects. The precipitates nucleated at grain boundary contribute to the grain refinement and the precipitate nucleated at dislocations strengthen the HSLA steel due to accumulation of dislocations. The shape of the precipitate varies depending on the formation conditions. Normally, the typical shapes of the precipitates are semi-dendritic, dendritic, rod-like and cuboidal if they are formed in liquid or semi liquid state.

2.3.2.2 Influence of the size and number of precipitate on precipitation hardening

2.3.2.2.1 Influence of the size of precipitate on precipitation hardening

The size of precipitates plays an important role in the precipitation hardening. It is well known that precipitate strengthens low carbon steel by grain refinement hardening and dislocation hardening. As for the dislocation hardening, there are two mechanisms for precipitate to impede the movement of dislocation. Dislocations cut the precipitates when the size of precipitates is small, while the dislocations bypass the precipitates when the size of the precipitates is large. Usually, the size of precipitate less than 5 nm is defined as small particle [45]. For this reason, large precipitates have a weak precipitation hardening effect no matter whether they are in dislocation hardening or in grain refinement hardening.

2.3.2.2.1.1 Small precipitate

The precipitate $\leq$ 5 nm is usually defined as small precipitate. The way the dislocation gets through the small precipitate is to cut through the precipitate as shown in the Figure 2.36 [45].

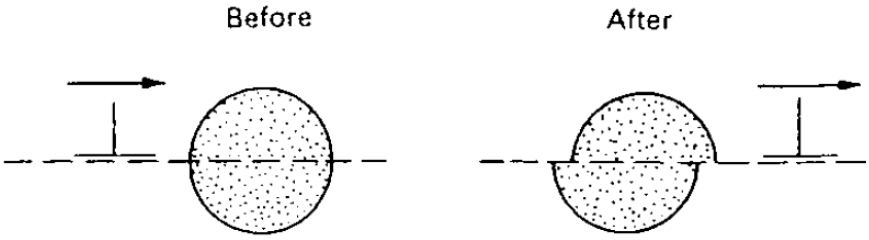

Figure 2.36 Dislocation motion may continue through second phase particles (particle cutting) [45]

The shear stress required to cut through a small particle is given by equation 2-2 [46].

$$\Delta\tau_y = (\gamma^{1/2}/b)\,(4r_s f/\pi T)^{1/2} \quad \text{.....(2-2)}$$

where $\Delta\tau_y$ is the increase in the shear stress due to the particle, γ is the antiphase boundary energy, the boundary resulting from the disordering effect of the penetrating dislocation, b is the Burgers vector of the dislocation, r_s is the mean radius of the particle in the slip plane, f is the volume fraction of particles, T is the free line tension of the dislocation in an isotropic matrix.

It is clear that the cutting through stress is proportional to the radius of the small particle. The size of the small particle on the material strength increment can be clearly seen in Figure 2.37 which reveals that the shear strength increment of the dislocation increases with the increase of the radius of the small precipitate [45].

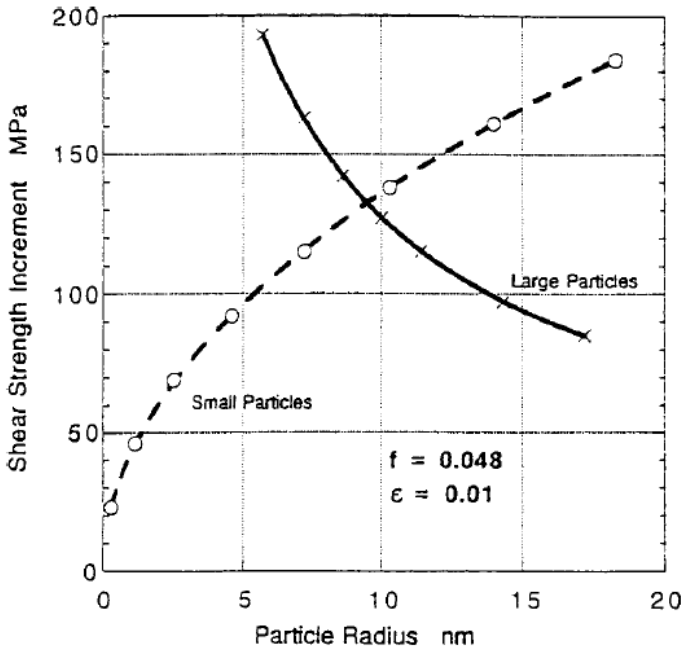

Figure 2.37 Relationship between shear strength increment and particle radius [45]

2.3.2.2.1.2 Large precipitate

The size of the large precipitate is more than 5nm and the strengthening mechanism of the large precipitate is different from the small precipitate. Dislocations move more freely when the size of the precipitate is large and they bypass the large precipitates instead of cutting through them. Figure 2.38 shows a dislocation bypassing large precipitates and forming Orowan dislocation loops [45].

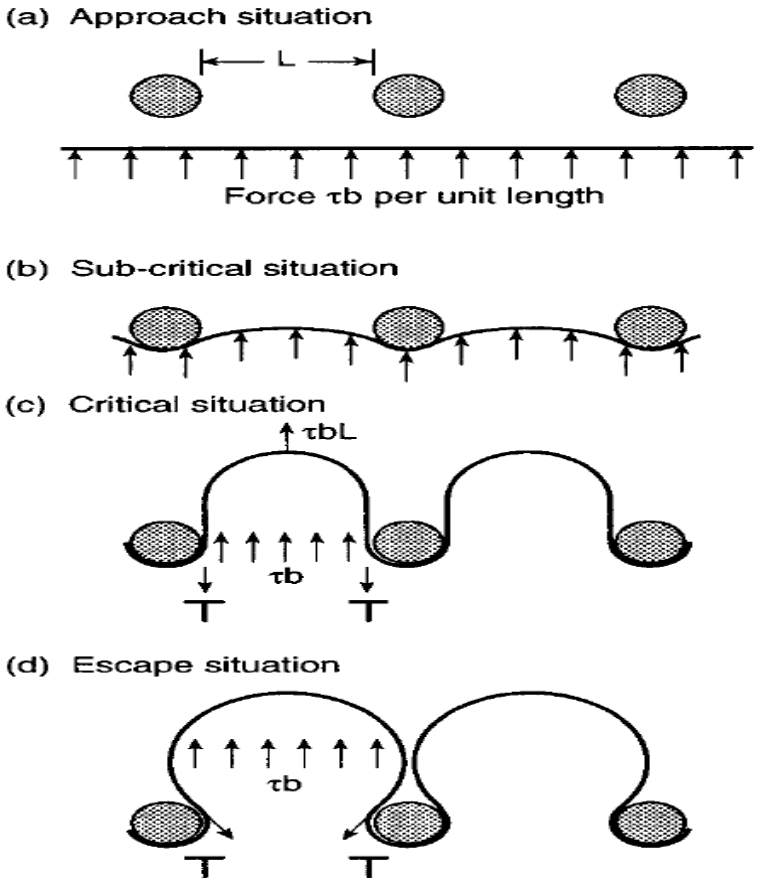

Figure 2.38 Dislocation meets hard undeformable second phase particles; dislocation release higher stresses may occur by Orowan looping or by cross-slip [45]

The strengthening effect of the large precipitate decreases with the increase of the size of the large precipitate, as it is shown by equation 2-3 [47].

$$\Delta\sigma = (0.538Gbf^{1/2}/X)\ln(X/2b) \quad \text{(2-3)}$$

where $\Delta\sigma$ is the increase in yield strength (MPa), G is the shear modulus (MPa), b is the Burgers vector (nm), f is the volume fraction of the particles, and X is the real diameter of the particles (nm).

2.3.2.2.2 Influence of the number of precipitate on precipitation hardening

It was reported that the strength of HSLA steel increases with the increase of the number of precipitate[45]. Under the condition of the small precipitate, the effective precipitation strengthening can be obtained when a high volume fraction of fine precipitates are produced [48-51]. The relationship between the strength increment and the volume fraction of the precipitate is shown in Figure 2.39 [45]. It is clear that the strength increment of HSLA steel is proportional to volume fraction of the precipitate.

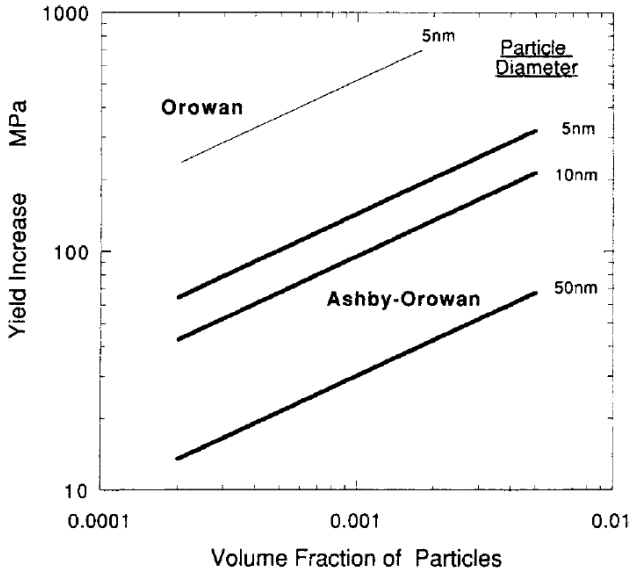

Figure 2.39 Ashby-Orowan relationship [45]

2.3.2.3 Spatial distribution of precipitate

There are mainly two types of spatial distributions of precipitates: coherent distribution and incoherent distribution. Usually, precipitates produced at a low aging temperature are so small that even transmission electron microscopy cannot resolve them and they are called precipitation zones. The spatial distribution of the precipitation zones is coherent with the matrix lattice, which is illustrated in Figure 2.40. In contrast, the

precipitates produced at high aging temperatures are coarser in size and tend to incoherent with the matrix lattice as shown in Figure 2.41 [52].

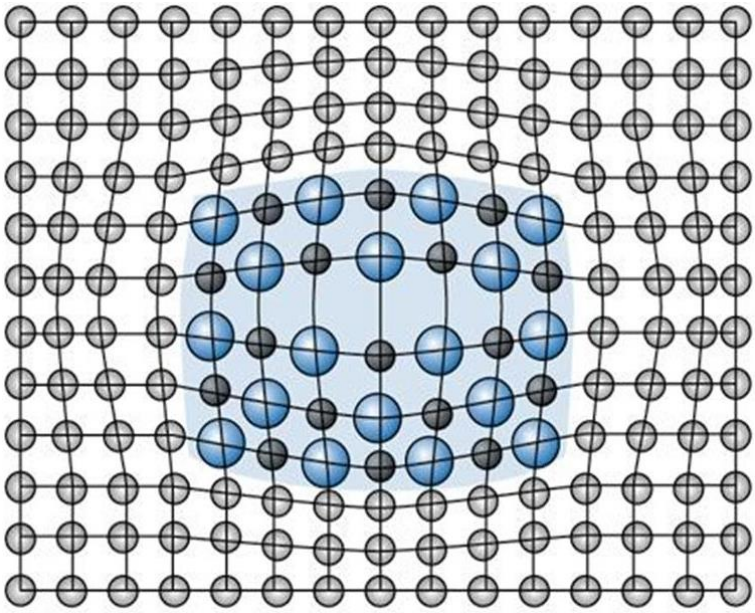

Figure 2.40 Zones or precipitate phase (aging) with lattice distortion [52]

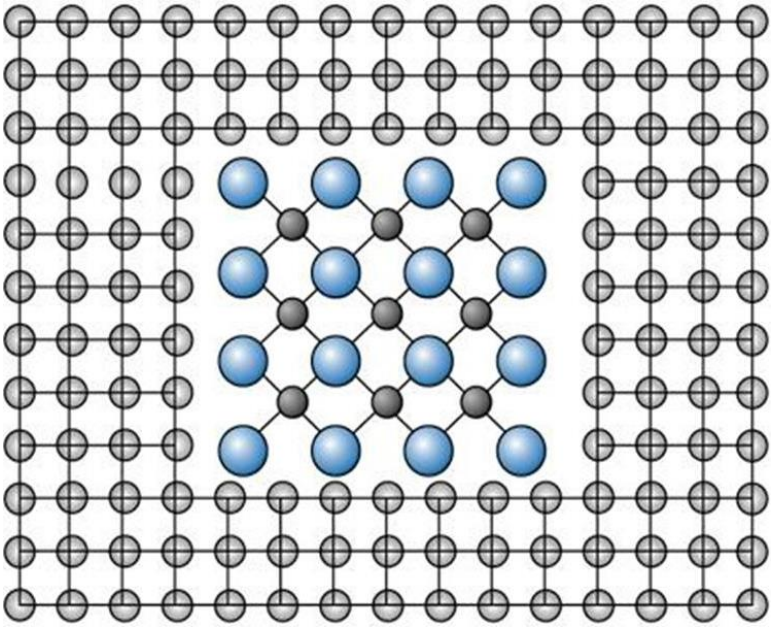

Figure 2.41 Equilibrium phase (Overaging) without distortion [52]

2.3.2.4 Stability of precipitate

It is well known that if more Nb atoms dissolving into solid solution in a solution heat treatment, more precipitates will be produced after an age hardening heat treatment. The stability of precipitates MX in austenite can be described by equation 2-4 [53].

$$\log[M]\,[X] = B - (A/T) \quad \text{(2-4)}$$

where: [M] and [X] - mass fraction of metallic micro addition and metalloid dissolved in austenite at temperature T in Kelvin, respectively, A and B are constants connected to the free enthalpy of MX phase formation. The values of A and B constants in equation (2-4) for selected interstitial phases are given in Table 2.2 [16,17].

Table 2.2 Values of the constants A and B [16,17]

MX phase	A	B
AlN	7184	1.79
VC	9500	6.72
VN	7840	3.02
TiC	10745	5.33
TiN	14400	5.00
NbC	7290	3.04
NbN	8500	2.80
ZrC	8464	4.26
ZrN	13968	3.08
TiN*	16586	5.90
BN	13970	5.24

Normally, the solubility of precipitate in austenite is higher than that in ferrite. The solubility of the various MX precipitates in austenite and ferrite as a function of

temperature are given in Figure 2.42 [54-59]. As expected that the solubility of the NbC precipitates in austenite is higher than that in ferrite.

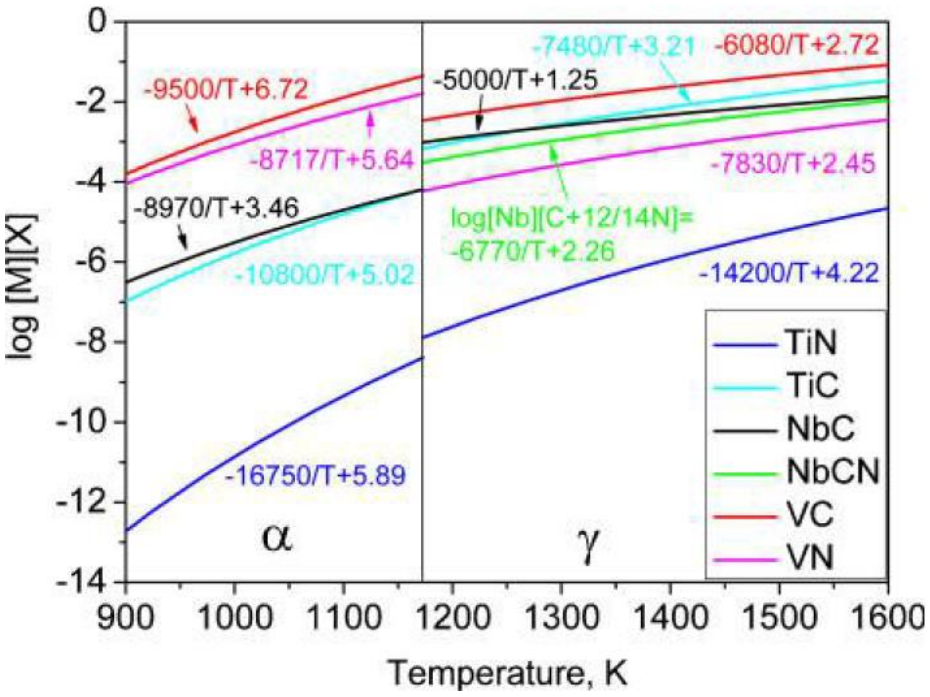

Figure 2.42 Solubility products of main precipitate species in HSLA steels [54-59]

2.3.2.5 Influence of aging time and aging temperature on precipitate during age hardening

2.3.2.5.1 Aging time

Figure 2.43 shows that the hardness of the UCS steel increases with the increase of the aging time until it reaches to peak hardness. After the peak hardness, the hardness of the steel decreases upon further aging [60]. Because the precipitate is small precipitate owning cutting mechanism to impede dislocation movement before the hardness of the steel reaches peak hardness and the shear strength increment of dislocation increases with the increase of the radius of the small precipitate. Therefore, the hardness of the steel increases with the increase of the aging time due to the grain growth of the small precipitate before the steel reaches the peak hardness. However, the precipitate is large

precipitate owing Orowan mechanism to impede the movement of the dislocation and the shear strength increment of dislocation decreases with the increase of the radius of the large precipitate. Therefore, the hardness of the steel decrease with the increase of the aging time due to the grain growth of the large precipitate after the steel reaches the peak hardness.

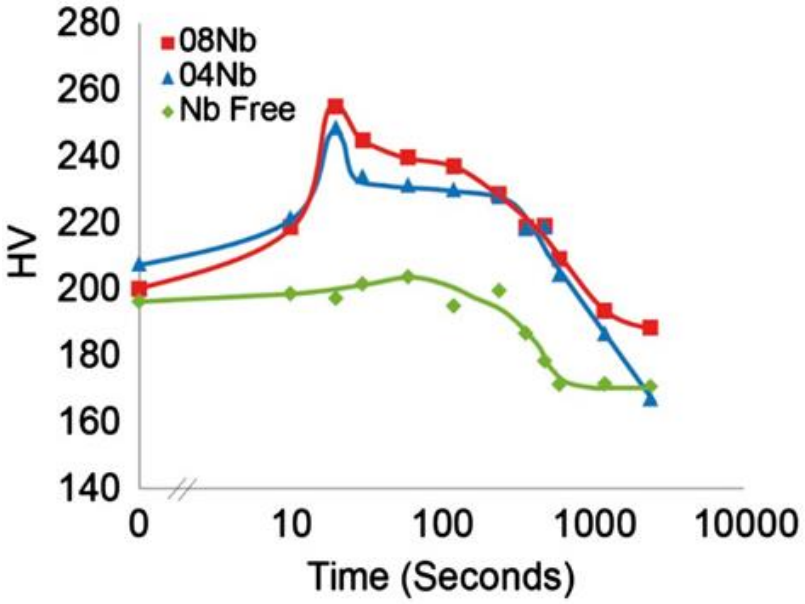

Figure 2.43 Hardness as a function of aging time for Nb-free, 0.04wt% and 0.08wt% Nb steel aged at 800°C [60]

2.3.2.5.2 Aging temperature

Aging temperature also plays an important role in an age hardening heat treatment. Figure 2.44 reveals the relationship between the aging temperature and the strength of the HSLA steel [3]. It is clear that the strength of the steel increases with the increase of the aging temperature before the steel reaches to the peak strength and then the strength decreases with the increase of the aging temperature. It has been reported that the size of precipitate is smaller when the steel is aged at lower temperature and it became coarser with the increase of the aging temperature due to higher diffusion rate of solute atom in higher aging temperature [52]. Before the steel reached to the peak strength, the aging

temperature is lower so the precipitate is small precipitate owning cutting mechanism to impede dislocation movement and the shear strength increment of dislocation increases with the increase of the radius of the small precipitate. Therefore, with the increase of the aging temperature, the small precipitate becomes coarser so that the strength of the steel increases. In contrast, after peak strength, the precipitate is large precipitate and the shear strength increment of dislocation decreases with the increase of the radius of the large precipitate. Therefore, with the increase of the aging temperature, the large precipitate becomes coarser so that the strength of the steel decrease with the increase of the aging temperature.

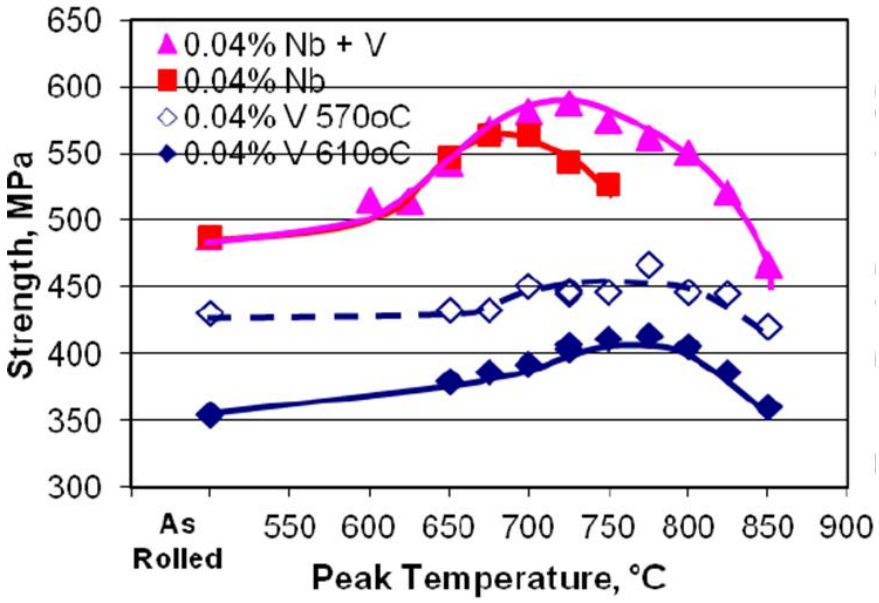

Figure 2.44 Laboratory aging results for V, Nb and V+Nb steels for strength as a function of peak aging temperature [3]

2.3.3 Strengthen mechanism of precipitation hardening

The precipitate nucleated at the grain boundary plays an important role in grain refinement. It has been shown that a pinning force can be produced by precipitates

nucleated at grain boundaries to impede the movement of the grain boundary and achieve grain refinement hardening [61,62]. For instance, in a thermal-mechanical control process, precipitates can suppress the austenite recrystallization to refine the austenite size and achieve grain refinement hardening [60]. Apart from the grain refinement hardening, the precipitate nucleated at dislocation produces pinning force to impede the movement of dislocation, which is the main strengthening mechanism of precipitation hardening in age hardening heat treatment [63].

2.3.4 The influence of cooling rate and coiling temperature on the Nb retention in low carbon steel in CASTRIP process

2.3.4.1 The influence of cooling rate on precipitation hardening

It is well known that Nb atoms segregate from solid solution to form precipitate during the hot rolling and subsequent cooling processes and the former is due to the strain induced precipitation and the latter is due to the decrease of the solubility of Nb atoms in the solid solution.

In terms of the precipitation during a cooling control process, a great number of studies focused on how does the temperature influence the diffusion rate and diffusion time of Nb atoms, only a few of studies focused on the temperature region where most precipitates are likely produced during CASTRIP process. Jun, who studied the effects of cooling rate and isothermal holding temperature on the precipitation behaviour of a Nb–Ti bearing HSLA steels, found that most precipitates do not form before the $\gamma \rightarrow \alpha$ phase transformation [64]. In their experiment (Figure 2.45), the samples were cooled from temperature melt to 800°C at a range of cooling rates and followed by a water quenching to room temperature. The amounts of Nb and Ti precipitates formed in the slab and simulated samples were measured and the results are shown in Figure 2.46 [64].

It is clear to see from the column chart that even with the very slow cooling rate of 10°C/min, there was just a small quantity of precipitates produced. According to Fe-Fe_3C phase diagram, there are no phase transformation occurred before 800°C for the steel. Therefore, it is a good evidence to prove that precipitates are not mainly produced before the $\gamma \rightarrow \alpha$ phase transformation.

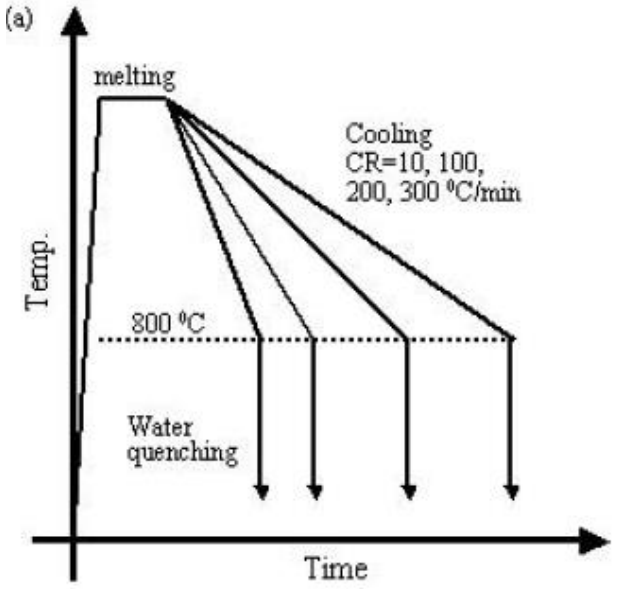

Figure 2.45 Thermal schedules of the simulation for solidification and cooling [64]

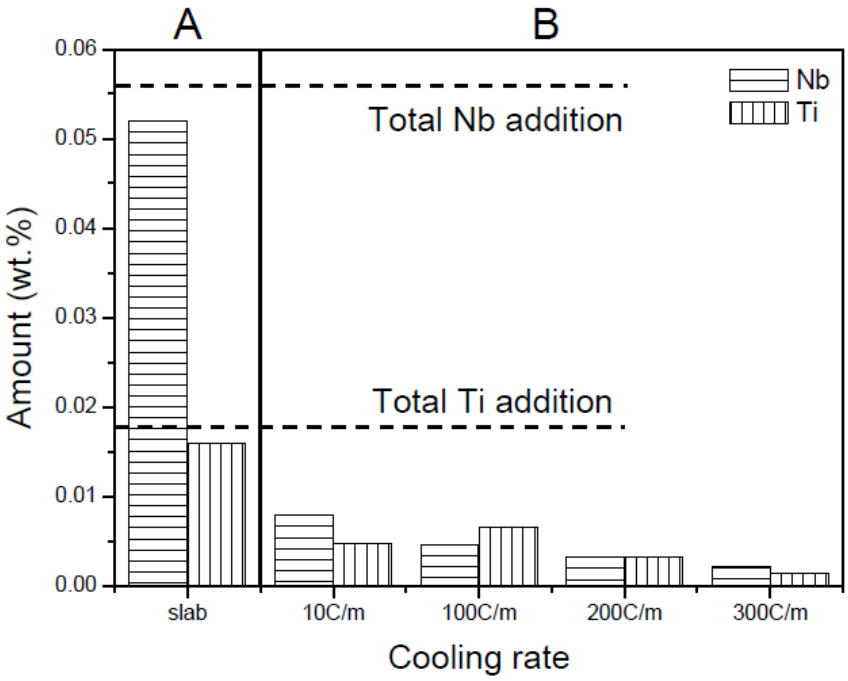

Figure 2.46 Amounts of Nb and Ti precipitated in precipitates formed in the cast slab, and in the simulated samples measured by dissolution and filtration with ICP spectroscopy [64]

In order to investigate if precipitates are produced during the $\gamma \rightarrow \alpha$ phase transformation of low carbon steel, R. Simoneau, who studied progress of Nb(CN) precipitation in HSLA steels, quenched the samples from 1350°C to room temperature at various cooling rates as shown in Figure 2.47 [2]. It was found that number of precipitates in the sample at the cooling rate of 4K/s is similar to that in the sample at 50K/s cooling rate as shown in Figure2.48 [2]. It is well known that phase transformation occurs in fairly short time during continuous cooling, for this reason, the dwelling time of the steel in the phase transformation temperature range is much shorter than that in the temperature range after phase transformation. If precipitates were mainly produced after the phase transformation, more precipitates should be detected at the cooling rate of 4K/s than at 50 K/s. Therefore, it confirms that precipitates are not

mainly produced after the $\gamma \rightarrow \alpha$ phase transformation temperature range. It is evident that precipitates are mainly produced in the $\gamma \rightarrow \alpha$ phase transformation temperature range during cooling and it is due to the large solubility difference of alloy carbides between the austenite and ferrite.

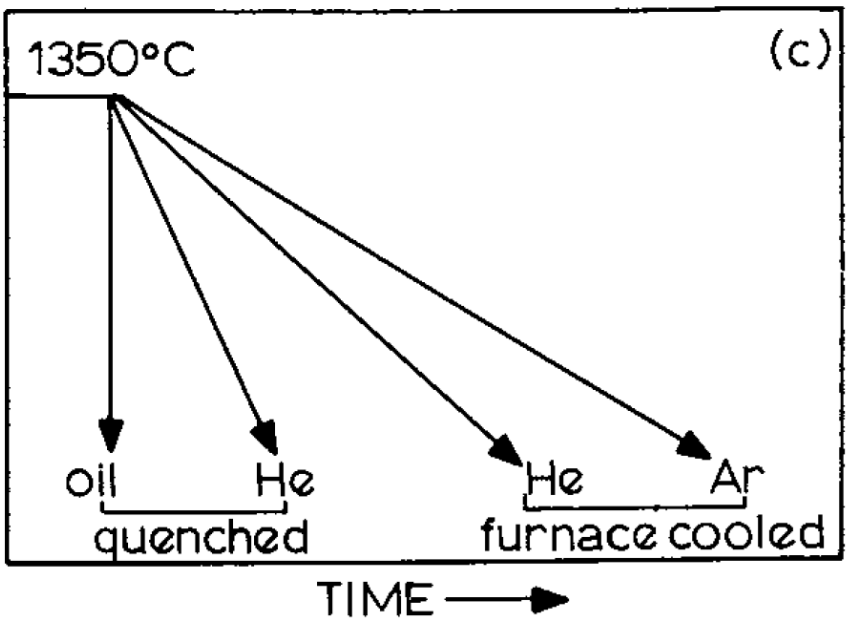

Figure 2.47 Heat treatment used in experiment [2]

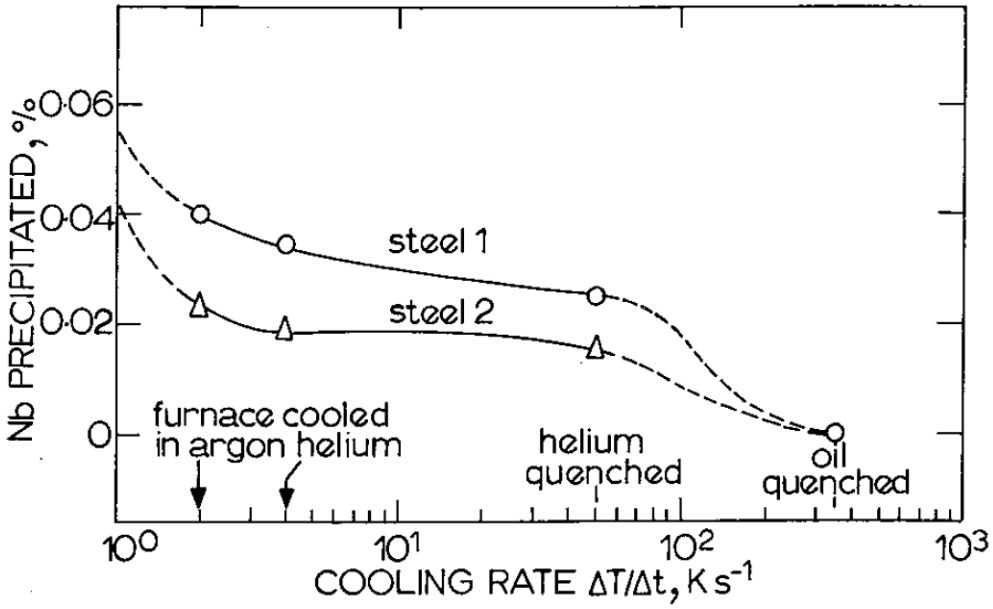

Figure 2.48 Effect of cooling rate on Nb precipitation after austenitization at 1350°C [2]

Cooling rate can influence the NbC precipitation hardening in low carbon steel. A. Ghosh, who studied the influence of thermos-mechanical processing and different post-cooling techniques on structure and properties of HSLA steel, did relevant experiment and the experiment procedure is shown in Figure 2.49 [65]. It is clear that the steel was heated to 1200°C and then carried out in 1-ton capacity down stroke power hammer in two stages until the steel was cooled to 800°C. The steel was cooled at three different cooling rates of 0.68, 1.15 and 35°C/s after 800°C. The microstructural observation is shown in Table 2.3 [65]. It has been shown that the precipitates became coarser and the volume fraction of precipitate became larger as the decrease of the cooling rate. This is because a slow cooling rate will give more time for Nb carbide to precipitate out and grow. Therefore, more precipitates were produced and less Nb atoms were left in the solid solution. It is well known that the age hardening effect will be significantly if more Nb atoms retained in the solid solution. For this reason, a fast cooling rate in a

cooling control process will lead to more Nb atoms retained in the solid solution after CASTRIP process. This will result in more precipitation strengthening in the age hardening heat treatment.

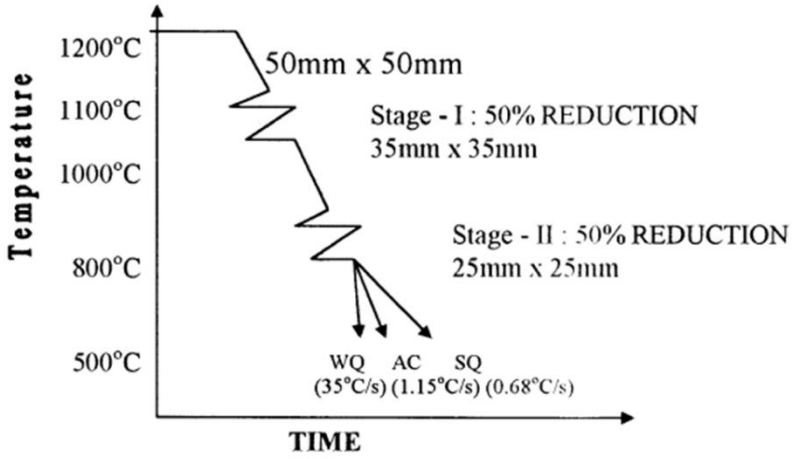

Figure 2.49 Schematic diagram of the simulation for forging and cooling [65]

Table 2.3 A summary of the microstructural observations [65]

	Water-quenched	Air-cooled	Sand cooled
Cooling rate	35 (°C s^{-1})	1.15(°C s^{-1})	0.68(°C s^{-1})
OM:			
Matrix (vol.%)	BF (59%)+GB (34%)	GB (91%)	PF (30%)+GB (52%)
Second Phase (vol.%)	7%	9%	18%
TEM:			
MA constituents/RA particle size	100–120 nm	150–190 nm	200–220 nm
Precipitates type:	NbC/NbCN, TiC/TiCN	NbC/NbCN, TiC/TiCN, ε-Cu	NbC/NbCN, TiC/TiCN
Size and shape	Spherical, 8–25 nm	Spherical, 5–25 nm	Spherical: 20–55 nm, cuboids: 150–165 nm, ε-Cu: spherical, 10–55 nm (fine ppt.)/110–125 nm (coarse ppt.) Rod shaped 40–45 nm

BF, bainitic ferrite; GB, granular bainite; PF, polygonal ferrite; RA, retained austenite; OM, optical microscopy; TEM, transmission electron microscopy.

As previously mentioned, precipitates are mainly produced during γ-α phase transformation range in CASTRIP process. In order to know how the cooling rate

influences the precipitation hardening during phase transformation temperature range, Burgmann et al studied the Influence of cooling rate on the precipitation behaviour of the Ti-Nb-Mo microalloyed steel samples cooled from 850 to 600°C at the cooling rates of 5, 1 and 0.5°C/s, the detailed experiment procedure is shown in Figure 2.50 [66]. In order to prove that the phase transformation temperature range of the samples at the different cooling rates is nearly between 600 and 850°C, a CCT diagram was plotted as shown in Figure 2.51 [66]. TEM observations of the fine precipitates in the samples at the different cooling rates are shown in Figure 2.52 [66]. It is clear that only a small amount of precipitates were produced in the sample cooled at 5°C/s from 850 and 600°C and the number of the precipitates increases with the decrease of the cooling rate.

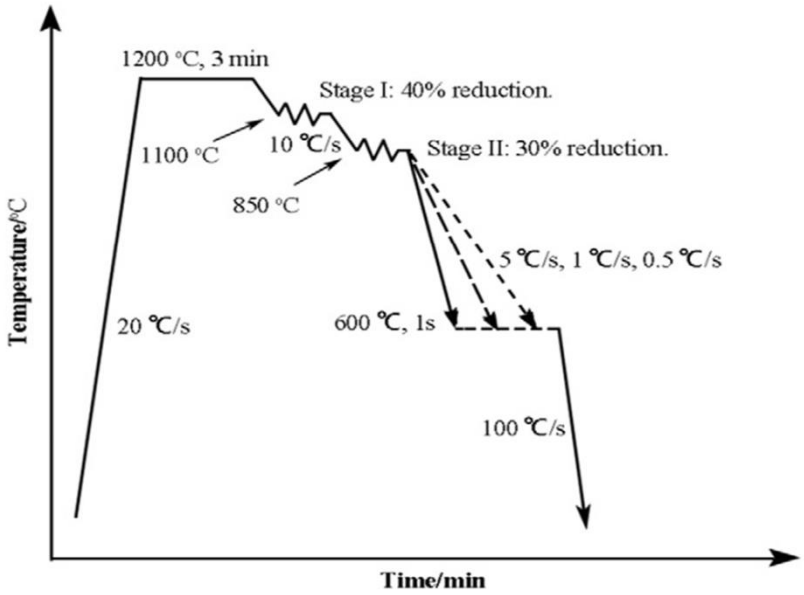

Figure 2.50 Schematic diagram of the simulation for rolling and cooling [66]

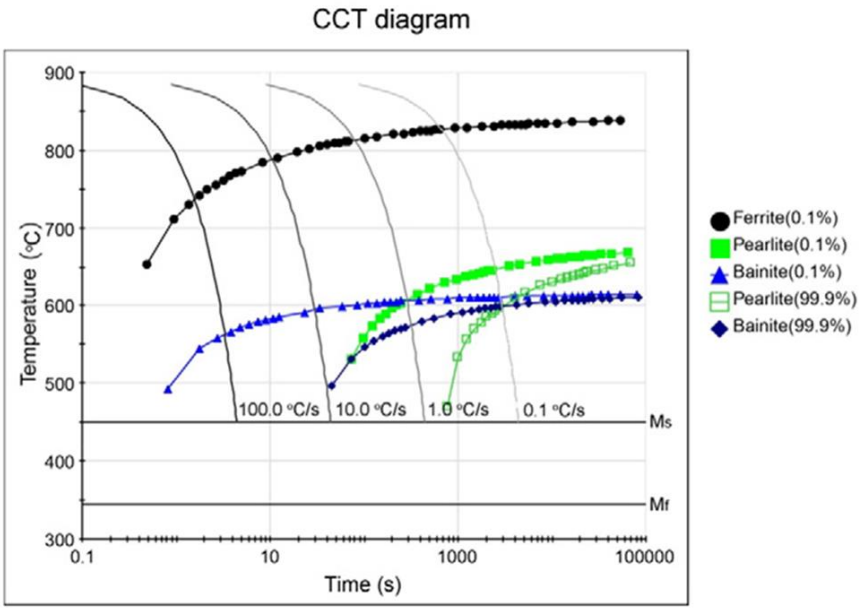

Figure 2.51 Continuous cooling transformation diagram(CCT) calculated by JMatPro [66]

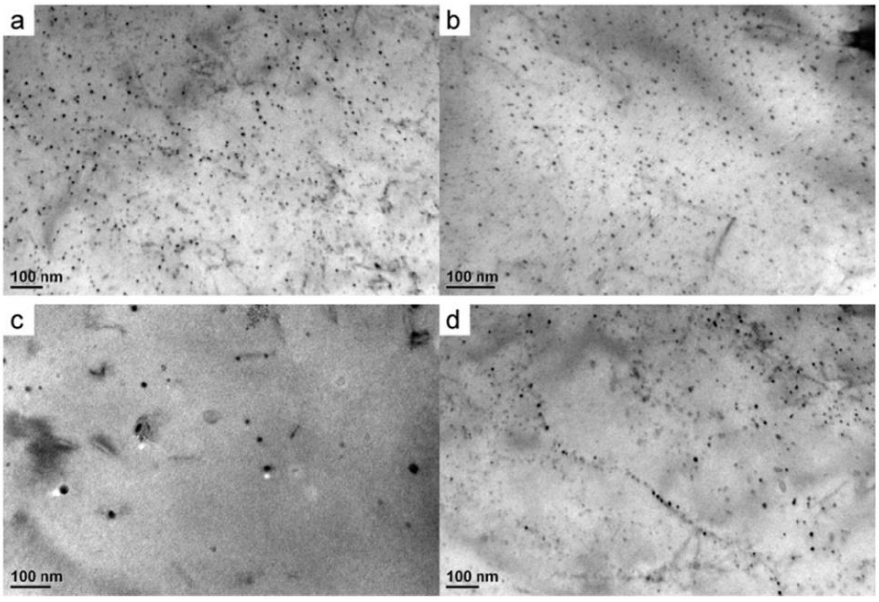

Figure 2.52 Bright field TEM micrographs of Ti-Nb-Mo steel at different cooling rates showing fine carbide precipitates at (a) 0.5°C/s (b) 1°C/s (c) 5°C/s, and (d)precipitation at subgrain boundary [66]

2.3.4.2 The influence of coiling temperature on precipitation hardening

A very important work has been dedicated to investigate how the coiling temperature influences the precipitation hardening in CASTRIP process. It is believed that the size of the precipitate became coarser with the increase of the coiling temperature due to a faster diffusion rate of Nb atoms in the higher coiling temperature region. The relationship between the coiling temperature and precipitation hardening is schematically illustrated in Figure 2.53 which reveals that only a small amount of precipitates was produced and the size of the precipitate is small in the sample produced in the coiling temperature region Ⅰ, which is attributed to a slow diffusion rate of Nb atoms in the lower coiling temperature region[1]. The precipitates became larger and denser with the increase of the coiling temperature to the coiling temperature region Ⅱ due to a faster diffusion rate of Nb atoms in the higher coiling temperature region. Consequently, the hardness of the ferrite increases because of the denser and larger precipitates. In region Ⅲ, the size of the precipitate became coarser due to the even faster diffusion rate of Nb atoms, the coarser precipitate cannot play any useful role in the hardness increment. Park, who studied the strengthening mechanism of a hot rolled Ti and Nb microalloyed HSLA steel, also pointed out that the average precipitates size increases with the increase of the coiling temperature, which can be seen in Figure 2.54 [67].

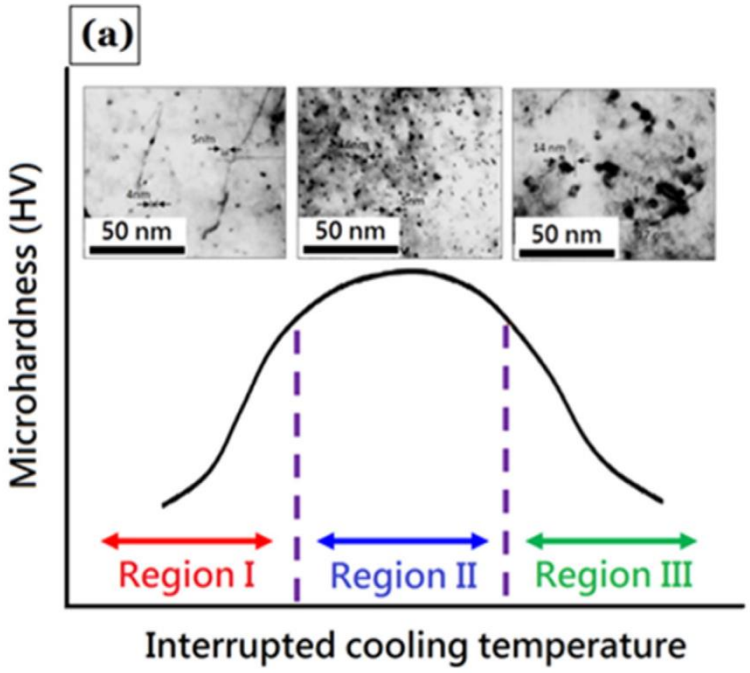

Figure 2.53 Schematic diagram dividing the variation of microhardness with interrupted cooling temperature into three different regions and further associating the microhardness with the carbide precipitation by corresponding TEM images [1]

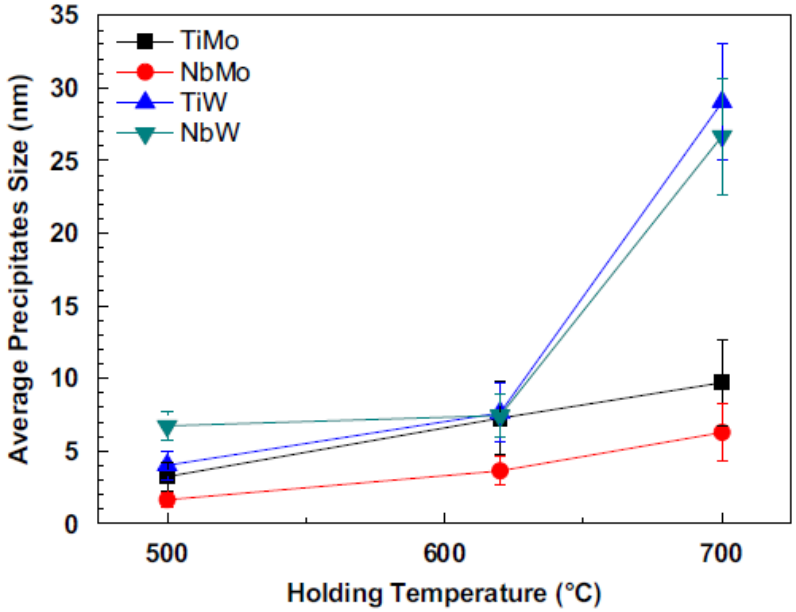

Figure 2.54 The average size of precipitates of the steels treated by the different simulated hot-coiling temperatures [67]

2.4 Literature review summary

CASTRIP process is a revolutionary new twin-rolling technique for producing strip cast steel and it uses less energy, time and space compared to a conventional continuous casting process. It is mainly composed of three parts: twin-roll casting, hot rolling reduction, controlled cooling process. Cooling rate and coiling temperature can be used to control the γ-α phase transformation and the Nb retention of the steel during the controlled cooling process. More bainite and less polygonal ferrite are produced with the higher cooling rate and the lower coiling temperature. The reason is that with the higher cooling rate, there are not enough dwelling time of the steel in autenite to polygonal ferrite transformation range and with the lower coiling temperature, the steel will spend less time in the austenite to polygonal ferrite transformation range and more time in the austenite to bainte range. For the influence of the cooling conditions on the Nb retention, more Nb atoms are retained in the solid solution with the fast cooling rate due to insufficient diffusion time and fewer Nb atoms are retained with the higher coiling temperature due to higher diffusion rate.

3 Experimental Procedure

3.1 Materials

The steel used in the experiment is ultra-thin cast strip (UCS) steel， produced in CASTRIP process and supplied by BlueScope. The chemical composition of the steel is shown in Table 3.1. The steel contains 0.031wt% C, 0.059 wt% Nb and the total alloy elements in the steel is below 1wt %.The steel strip is only 0.95 mm thick.

Table 3.1. Chemical compositions of the UCS steel.

Element	C	P	Mn	Si	S	Ni	Cr	Mo	Cu	Nb	N
wt%	0.031	0.014	0.738	0.159	0.003	0.047	0.057	0.017	0.095	0.059	0.005

3.2 Experimental approach

3.2.1 Heat treatment

The heat treatments used in this investigation simulate the CASTRIP process in terms of prior austenite grain size and cooling rates from 900 °C to the coiling temperatures and the simulation experiments were carried out on a Theta dilatometer which is shown in Figure 3.1. The geometry of the diatometry samples is shown in Figure 3.2 and the thickness of the samples is 0.95mm.

Figure 3.1 Theta Dilatometer

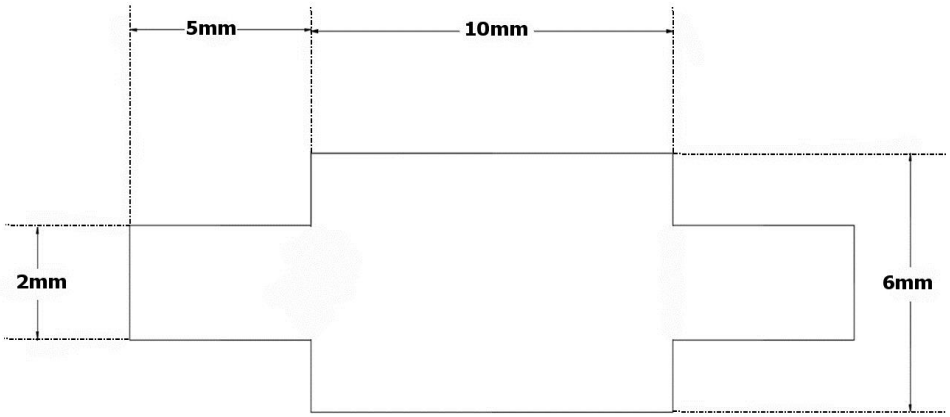

Figure 3.2 Dilatometer sample

At the beginning of the experiment, the sample need to be welded to a thermocouple which is a thermoelectric device used to measure the temperature of the sample during the heat treatment. It is necessary to make sure that the steel is well welded to the thermocouple. Otherwise, the temperature measurement will not be correct. The sample and thermocouple were assembled in the dilatometer after the welding process. In order to avoid oxidation of the sample during the heat treatment, the dilatometry experiments were carried out in vacuum of 6.7×10^{-2} Pa.

The maximum reheating temperature of the dilatometer is 1300˚C and the reheating temperature of 1280˚C was chosen for the heat treatments in order to better simulate CASTRIP process. Figure 3.3 shows that the sample was heated to 1280˚C at the heating rate of 20˚C/s after the chamber was evacuated for six minutes by a mechanical pump. The sample was held at 1280˚C for 5 mins and then cooled to 900 ˚C at the fast cooling rate of 50˚C/s. The purpose of the experiment is to study the influence of the cooling condition on the Nb retention in the steel in the CASTRIP process. Therefore, after 60 seconds dwelling time at 900˚C, the sample was cooled to the coiling

temperatures at the three different cooling rates of 1, 5 or 40˚C/s. It then was cooled from the coiling temperatures to 300˚C at the cooling rate of 10˚C/min followed by a helium gas quenching to room temperature. Two coiling temperatures, 500 and 675˚C were chosen because they are used in the CASTRIP process and the same heat treatments were also carried out when the reheating temperature of 1150 ˚C was used as shown in Figure 3.4. It has to be noted that all niobium were dissolved into solid solution during reheating process no matter in 1280 ˚C or 1150 ˚C, which is determined after the calculation of solubility of niobium based on equation 2-4.

After the simulated CASTRIP heat treatment, the sample was divided into two parts by using a cutting machine as shown in Figure 3.5. One part is for structure characterisation and hardness measurement and another part is for the post aging treatment which is also carried out in the dilatometer and the sample was aged at 700˚C for 60 s and cooled to room temperature by helium gas quenching as shown in Figure 3.6.

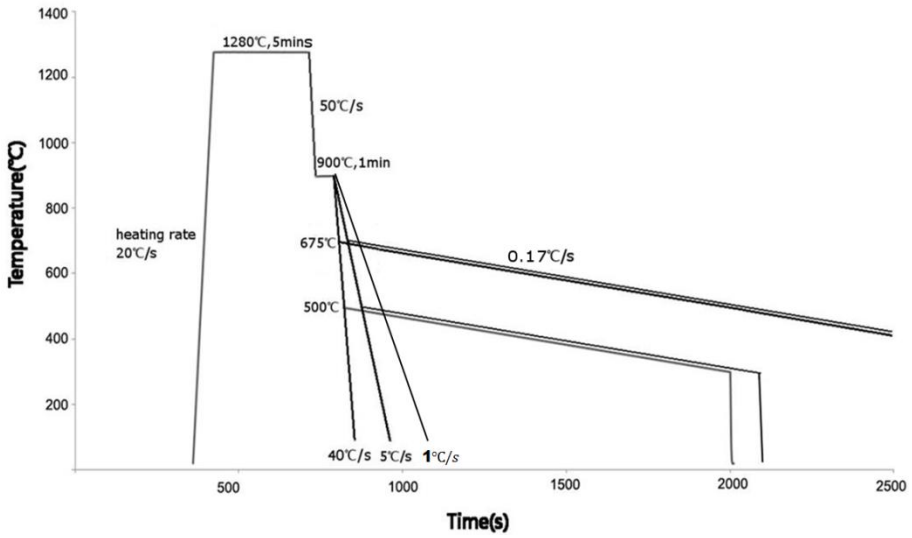

Figure 3.3 Heat treatment simulated CASTRIP process under the condition of 1280˚C reheating temperature

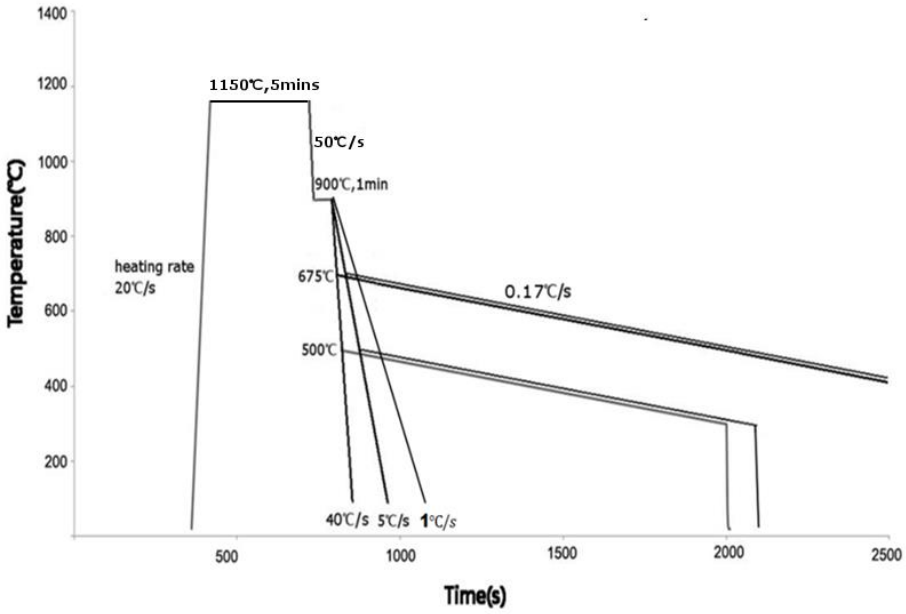

Figure 3.4 Control experiment under the condition of 1150˚C reheating temperature

Figure 3.5 Antitheses to show age hardening performance

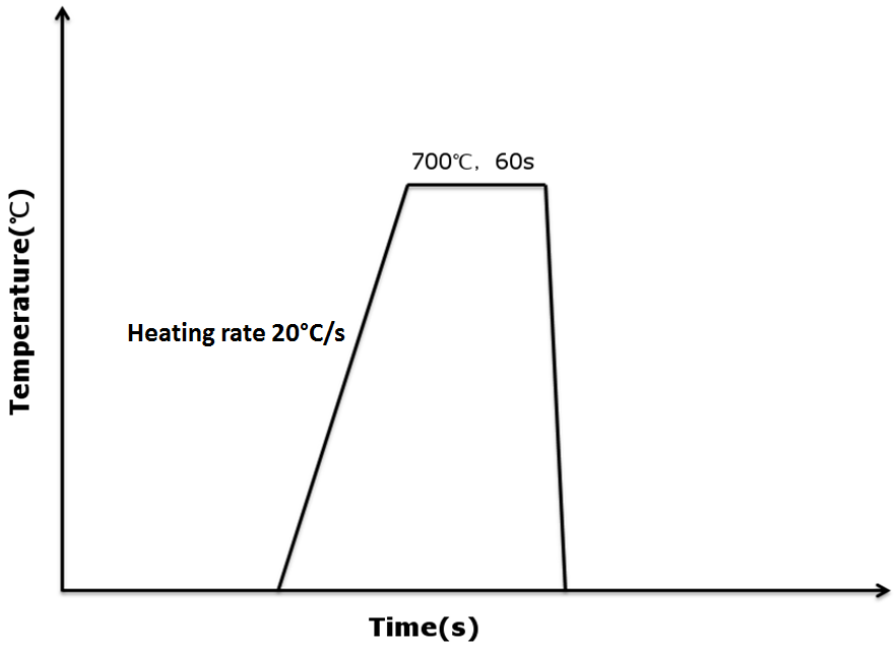

Figure 3.6 Heat treatment simulated post age hardening heat treatment.

3.2.2 Sample sectioning

The heat treated samples are sectioned on a Struers Accutom 5/50 machine which is shown in Figure 3.7 with 0.02 mm/sec feed speed rate. The sample used in the experiment is soft due to its low carbon content. Therefore, 357 CA cut-off wheel was chosen according to Table 3.2 [51].

Figure 3.7 Accutom 5/50 Sectioning machine

Table 3.2 Wheel Selection based on the characterization of material [51]

Cut off machine	Non ferrous soft metals	Soft ferrous metals	Medium soft ferrous metals	Medium hard ferrous metals HP<500	Hard ferrous metals
Accutom-5/50	357CA	357CA	357CA	356CA	356CA

3.2.3 Sample mounting

The samples used in the experiment were mounted on a Struers CitoPress-20 mounting machine which is shown in Figure 3.8. They were mounted by thermosetting resins which are known as compression-mounting materials requiring heat and pressure for

curing. MultiFast resin was chosen as the mount material in the experiment. The sample was put into mounting machine followed by MultiFast resin and then heated to 180°C for 6.5 minutes under the pressure of 3600 psi.

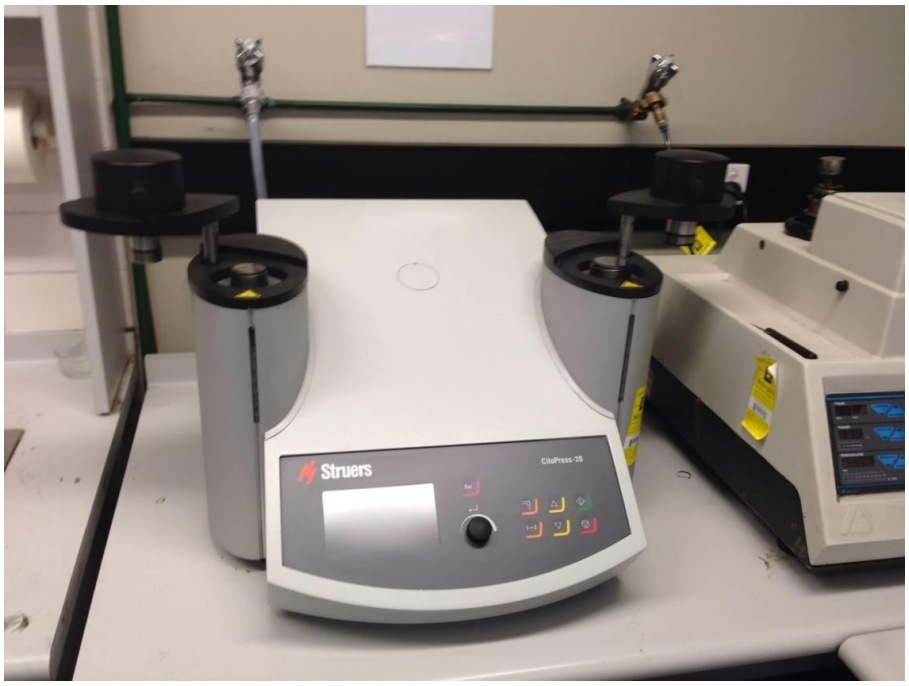

Figure 3.8 Struers CitoPress-20 mounting machine [51]

3.2.4 Grinding and polishing

The sample used in the experiment was grinded and polished by abrasive particles to form bright mirror like surface and then the microstructure of the sample was observed under the microscope. Struers grinding and polishing equipment were used in the experiment as shown in Figure 3.9. Metalogram is used to choose the correct preparation method based on the properties of a specific material as shown in Figure 3.10. It provides ten universally applicable methods which cover all materials. The selection of the preparation method depends on hardness and ductility of the material. The hardness of the UCS steel used in experiment is between 180HV and 250HV and it

owns excellent toughness. Therefore, method D was chosen to grind and polish the samples. The grinding and polishing details are shown in Table 3.3.

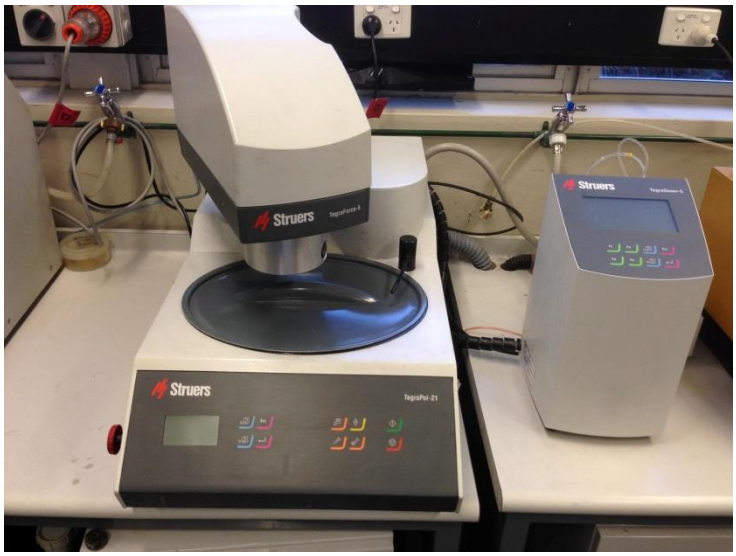

Figure 3.9 The Struers grinding and polishing equipment used in the experiment

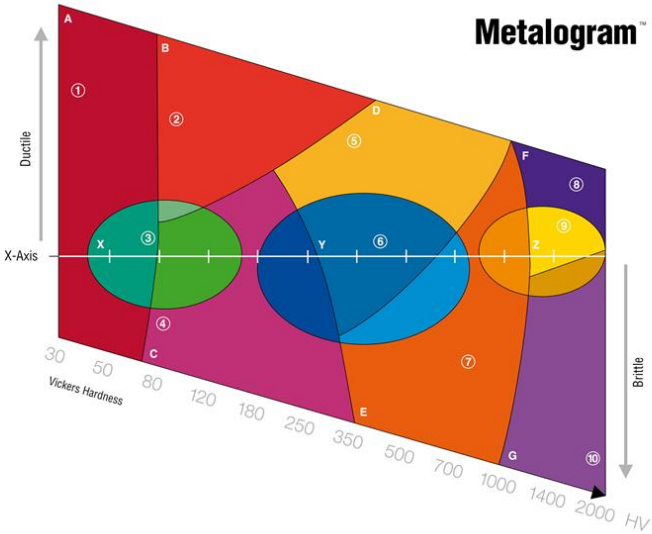

Figure 3.10 Metalogram

Table 3.3 Grinding and polishing detail for method D

Grinding			Polishing		
Step	PG	FG	Step	DP	OP
Surface	MD-Piano 220	MD-Allegro	Surface	MD-Dac	MD-Chem
Abrasive	Diamond	DP-Suspension	Abrasive	DP-Suspension	OP-A
Grit/ Grain size	-	9 µm	Grain size	3 µm	-
Lubricant	Water	Green / Blue	Lubricant	Green / Blue	-
[rpm]	300	150	[rpm]	150	150
Force [N]	180	180	Force [N]	180	90
Time [min]	Until plane	4	Time [min]	4	2

It is clear from Table 3.3 that the experimental procedure is mainly composed of grinding and polishing. Grinding consists of plane grinding (PG) and fine grinding (FG) and polishing consists of diamond polishing and oxide polishing. At the beginning of the experiment, the sample was grinded on the MD-Piano 200 grinding cloth for 5 minutes and water was used for cooling. And then it was grinded on the MD-Allegro grinding paper for 4 mins. 9 µm diamond polish suspension was used and the green and blue lubricants were chosen to protect the material from damage in the fine grinding. The diamond polishing (DP) process was carried on after the plane grinding. The sample was polished on the MD-Dac polishing paper for 4 minutes and 3 um diamond polish suspension and green and blue lubricants were chose in this process. The last step of the experiment is oxide polishing (OP) in which colloidal silica is used to produce a scratch-free surface. The advantage of the oxide polishing is that it not only can produce

a scratch-free surface, but also can save time. The oxide polishing time in the experiment is only 2 minutes.

3.2.5 Etching

Etching was used to reveal the microstructure of the sample before the optical microscopic analysis. 2% Nital and laboratory glassware were used in the experiment. The etching time is essential in the etching process because over etching or under etching will happen if the etching time cannot be well controlled. After a series of tests, the etching time of the sample is finally controlled at 10 s in the experiment. It has to be noted that nital is a volatile liquid, therefore, it is necessary to use top to cover the glassware after etching process. In addition, in order to guarantee the safety in the experiment, wearing acid resistant gloves, lab coat and safety glasses are also very important.

3.2.6 Optical Microscope

A LEICA DMR optical microscope was used to observe the microstructure of the samples and capture the images for microscopic analysis as shown in Figure 3.11. The observation started at a lower magnification and ends at a higher magnification in the experiment and assisting computer software was used to capture the images.

Figure 3.11 Light optical Microscope used in the experiment

3.2.7 Vickers Hardness and Microhardness tests

Vickers hardness and micro Vickers hardness tests were performed on an INDENTEC Vickers hardness testing machine and LECO M-400-H1 micro Vickers hardness testing machine which are shown in Figures 3.12 and 3.13 respectively. The experimental operations of the two machines are similar. It has to be noted that the machines should be zero set before Vickers or micro Vickers hardness measurement commencing. In the Vickers hardness test, a low applied force of 1 kg was applied to the sample because the samples used in the experiment are very soft and thin. Each sample was measured eight times and the average testing value was finally taken, which can improve the measurement precision. In the micro Vickers hardness test, the size of the indentation must be smaller than the measured grain and the location of it must be within the measured grain. After a series of testings, it was found that a 0.05 kg load is appropriate for the micro hardness measurements and it was finally chosen to measure the micro Vickers hardness of the each constituent of the sample in the experiment. The

micro Vickers hardness of the each constituent was also measured eight times and the average testing value was finally taken to guarantee measurement precision.

Figure 3.12 INDENTEC Vickers hardness testing machine

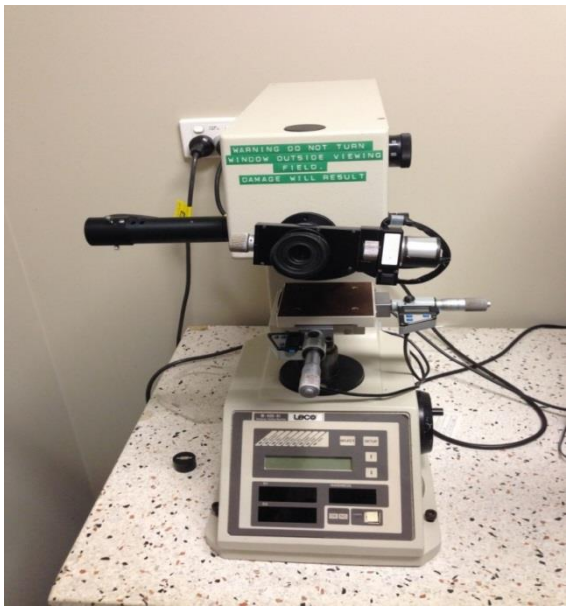

Figure 3.13 LECO M-400-H1 micro Vickers hardness testing machine

3.3 Optical microscopy

3.3.1 Austenite grain size measurement

The austenite grain size of the samples at two different reheating temperatures of 1150 and 1280°C were measured in the experiment. The nucleation sites of polygonal ferrite are austenite grain boundaries, therefore, the polygonal ferrite nucleated at austenite grain boundaries were used to outline the pre-austenite grains as shown in Figure 3.14. Three measurements were carried out in order to minimise the experimental errors. At the beginning of the first measurement, a straight line was plotted and the length of it was measured as shown in Figure 3.15, and then the number of austenite the straight line crossed was measured. Eventually, the average value of the austenite grain size was obtained by using the length of the straight line divided the number of austenite grain. In order to decrease the experimental errors, the second and third measurements were carried out as shown in Figures. 3.16 and 3.17. The final austenite grain size was achieved by averaging the values obtained from three measurements.

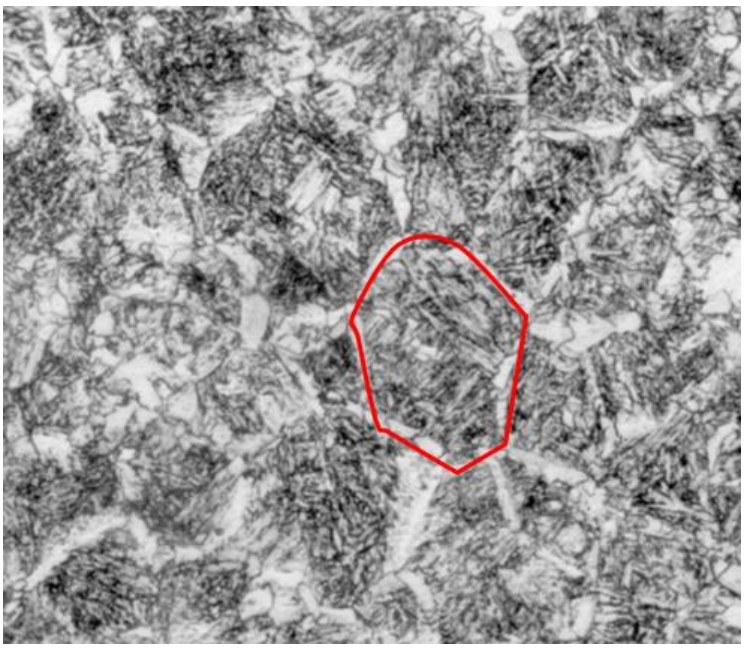

Figure 3.14 Outline austenite grain boundary based on bainitic ferrite

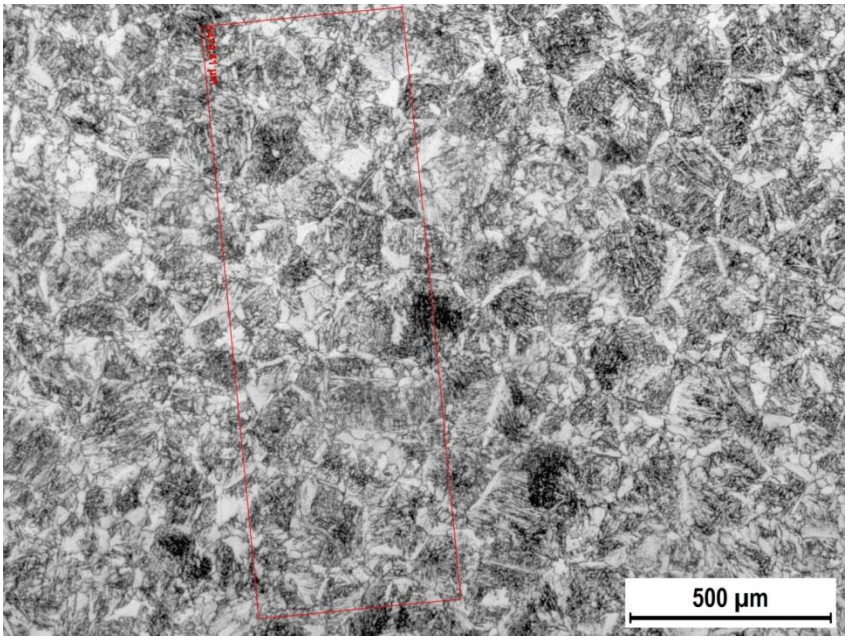

Figure 3.15 Eight austenite grains are measured to calculate austenite grain size

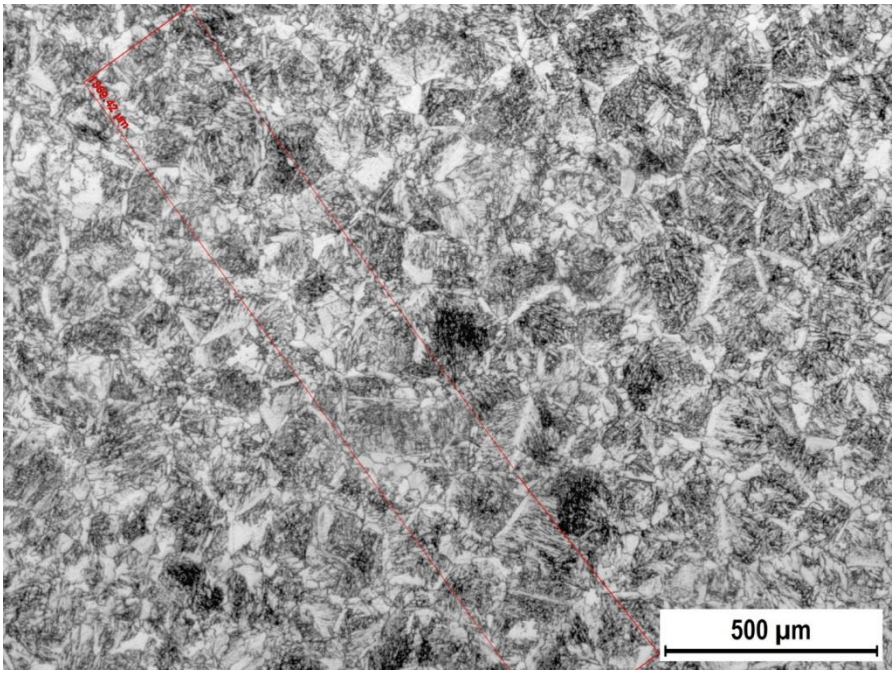

Figure 3.16 Ten austenite grains are measured to calculate austenite grain size

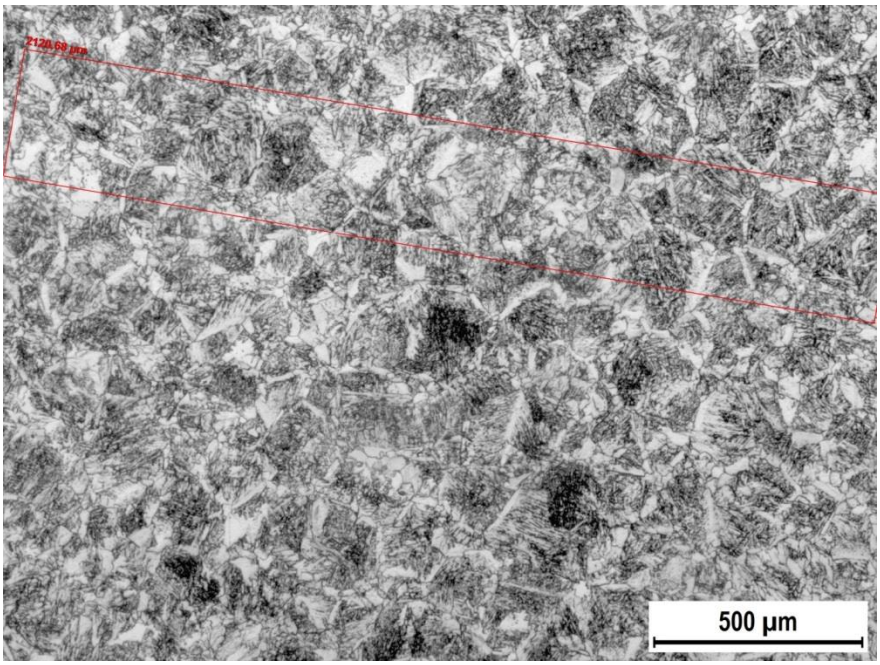

Figure 3.17 Thirteen austenite grains are measured to calculate austenite grain size

3.3.2 Volume fraction of constituents measurement

In order to know how the cooling rate and coiling temperature influence the phase transformations of the steel during CASTRIP process, the volume fraction of constituent was estimated by using the imaging analysis software Axiovision and Microsoft Excel. The micrographs obtained from the light optical microscope were used in the measurements.

3.4 Construct dilatation curve

The dilatation curve shown in Figure 3.18 was obtained by combining the dilatometer data and the microscopic observation in the experiment. Microsoft Excel was used to assist in drawing dilatation curve. The phase transformation start and finish temperatures were labelled in the dilatation curve as shown in Figure 3.18.

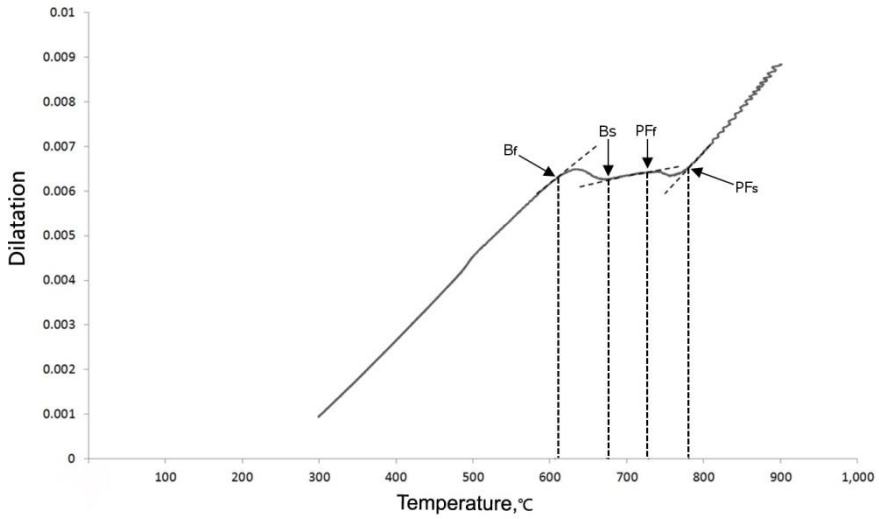

B= bainite; PF polygonal ferrite

Figure 3.18 Dilatation curve mapped in the experiment

4 Results

4.1 Microstructure, phase transformation and hardness of the samples solution treated at 1280°C and cooled from 900°C to the coiling temperature of 675°C at the cooling rates: 1 °C/s, 5°C/s and 40°C/s

4.1.1 The sample cooled at 1 °C/s

Figure 4.1 shows typical microstructure of the sample which consists of 98% polygonal ferrite and 2% pearlite. The polygonal ferrite nucleated at austenite grain boundary and grew away from the austenite grain boundaries and formed the equiaxed grains. The surfaces of the polygonal ferrite grains are smooth, reflecting more light and appear bright and they are separated by continuous, linear boundaries. The pearlite nucleated heterogeneously on the prior austenite grain boundaries appears darker compared to the polygonal ferrite due to the high density grain boundaries it contained. The size of polygonal ferrite is about 56μm. The Vickers hardness of the sample is 191HV1 and the micro Vickers hardness of the polygonal ferrite is 192HV0.05. Clearly the Vickers hardness and micro Vickers hardness measurements are consistent.

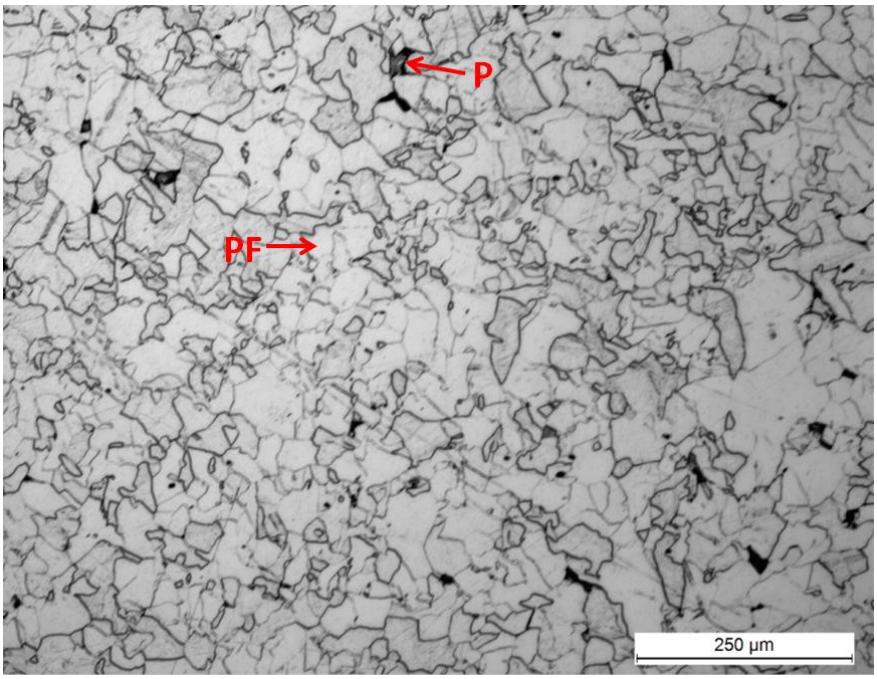

PF=polygonal ferrite; P=pearlite

Figure 4.1 Optical micrograph showing the transformation of microstructure for the sample cooled from 900°C to the coiling temperature of 675°C at the cooling rate of 1°C/s under the condition of the 1280°C reheating temperature

Figure 4.2 shows a dilatation curve. Since there is virtually no other microstructure rather than the polygonal ferrite during the cooling process, the transformation showed in the dilatation curve is the austenite to the polygonal ferrite phase transformation which started at about 801°C and finished at 668°C. The austenite to pearlite transformation cannot be shown clearly in the dilatation curve due to the extremely small amount of it in the sample. It is noted that the coiling temperature of 500°C is outside of the phase transformation temperature range, however, the coiling temperature of 675°C is within the range. The 500 and 675°C coiling temperatures were marked with red dotted lines in Figure 4.2.

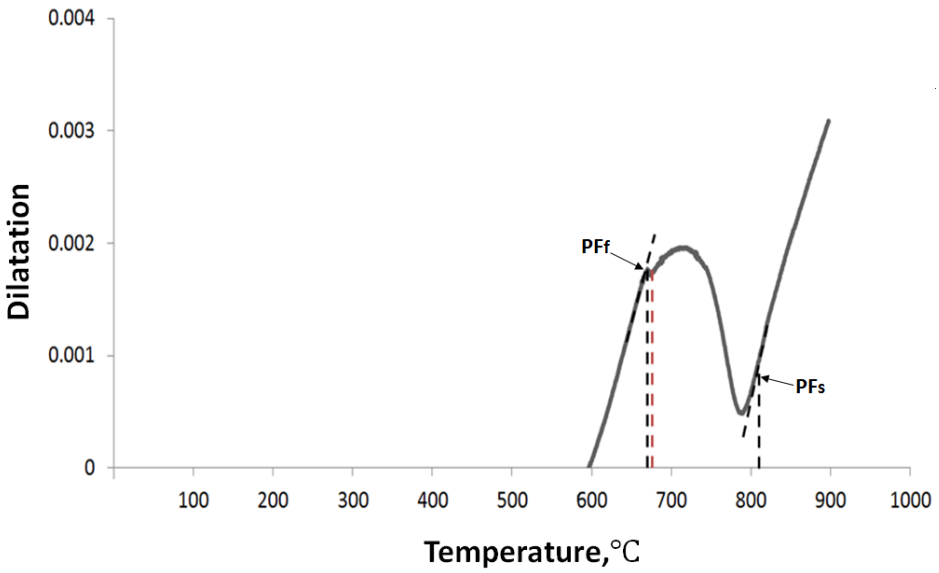

PF= polygonal ferrite

Figure 4.2 Dilatation curve obtained for the sample at the cooling rate of 1°C/s with the coiling temperature of 675°C under the condition of the 1280°C reheating temperature

4.1.2 The sample cooled at 5°C/s

The microstructure of the sample is shown in Figure 4.3. The dominant microstructure is the polygonal ferrite with a small amount of pearlite and bainite which appears as fine equi-axed pockets and within the pockets there are many fine ferrite plates. The volume fraction of the polygonal ferrite is 95% and the rests about 5% are the granular bainite and pearlite. The size of the polygonal ferrite is 45μm which is smaller than that of the sample cooled to 675°C at 1°C/s. A high magnification optical micrograph of the pearlite is shown in Figure 4.4. The Vickers hardness of the sample is 201HV1 and the micro Vickers hardness of the polygonal ferrite and granular bainite are 203HV0.05 and 221HV0.05 respectively.

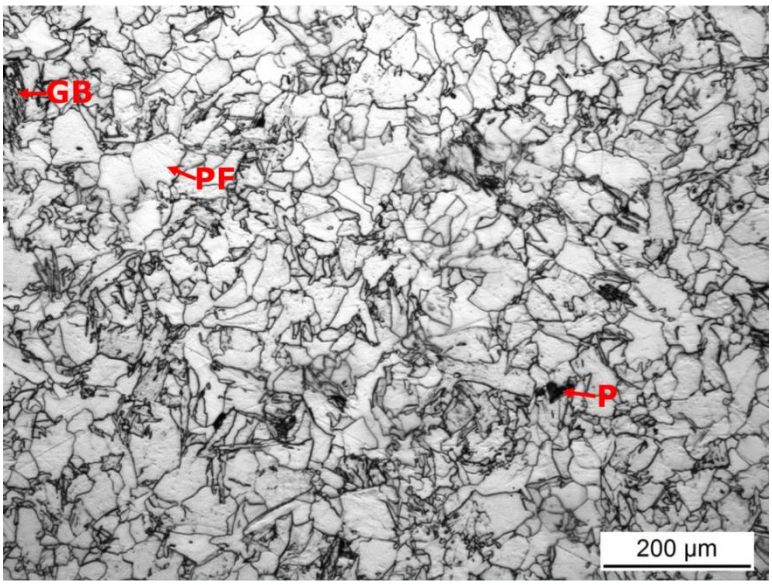

GB=granular bainite; PF=polygonal ferrite; P=pearlite

Figure 4.3 Optical micrograph showing the transformation of microstructure for the sample cooled from 900°C to the coiling temperature of 675°C at the cooling rate of 5°C/s under the condition of the 1280°C reheating temperature

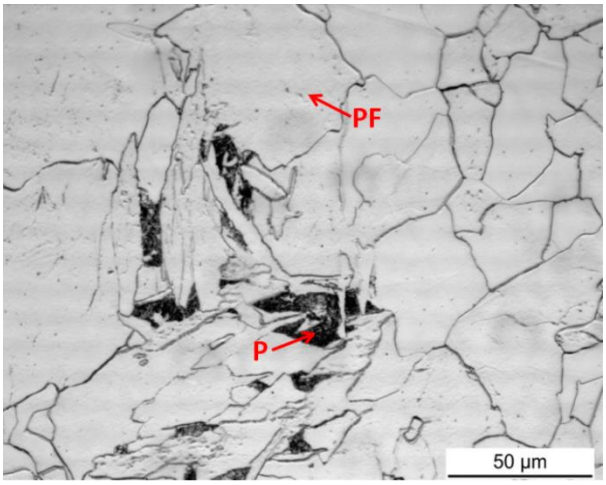

PF=polygonal ferrite; P=pearlite

Figure 4.4 Microstructure of the sample cooled from 900^{0}C to the coiling temperature of 675°C at the cooling rate of 5°C/s, showing pearlites were produced in this cooling condition.

The dilatation curve of the sample is given in Figure 4.5 which shows two phase transformations: the first one started at 786°C and finished at 731°C and the second one started at 679°C and finished at 671°C. It is believed that the former is the austenite to polygonal ferrite transformation and the latter is the austenite to pearlite and granular bainite. Again the coiling temperature of 500°C is outside of the γ-α phase transformation temperature range, however, the coiling temperature of 675°C is within the austenite to granular bainite transformation temperature range. The 500 and 675°C coiling temperatures were marked with dashed red lines in Figure 4.5.

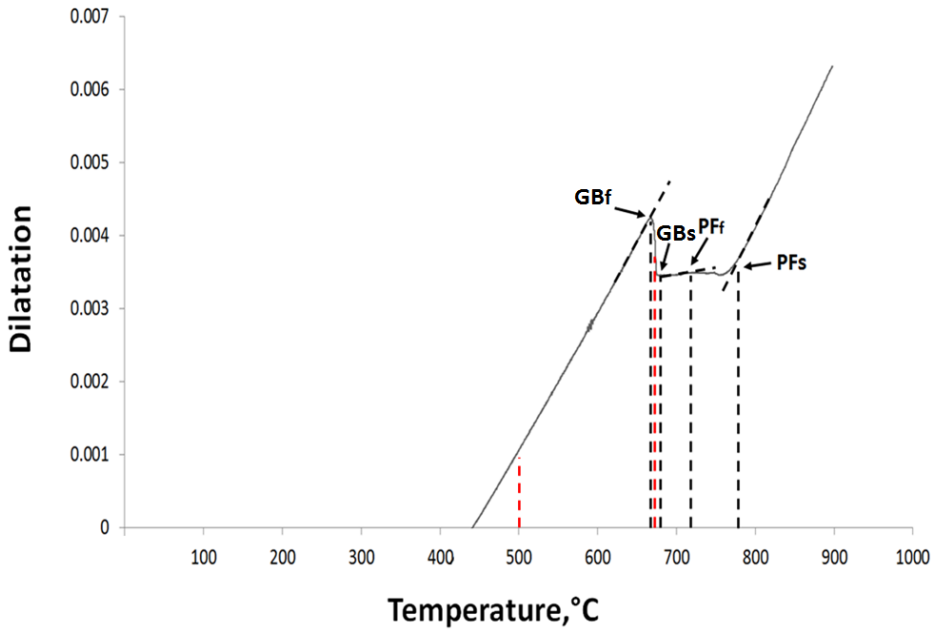

GB= granular bainite; PF= polygonal ferrite

Figure 4.5 Dilatation curve obtained for the sample at the cooling rate of 5°C/s with the coiling temperature of 675°C under the condition of the 1280°C reheating temperature

4.1.3 The sample cooled at 40°C/s

The microstructure shown in Figure 4.6 consists predominantly of granular bainite and acicular ferrite and a small amount of bainitic ferrite. The granular bainite nucleated away from the austenite grain boundaries and contains bundles of parallel lenticular shaped ferrites as shown in Figures 4.6 and 4.7. The acicular ferrite is similar to the granular bainite and it is not very easy to distinguish between the two microstructures in the experiment. Apart from the acicular ferrite and granular bainite, bainitic ferrite is also observed in the sample. They have a sheaf-like shape [20-23]. The combined volume fraction of the granular bainite and acicular ferrite is up to 55% and the value of the bainitic ferrite is 45%. The Vickers hardness of the sample is 204HV1 and the micro Vickers hardness of the granular bainite is 227HV0.05

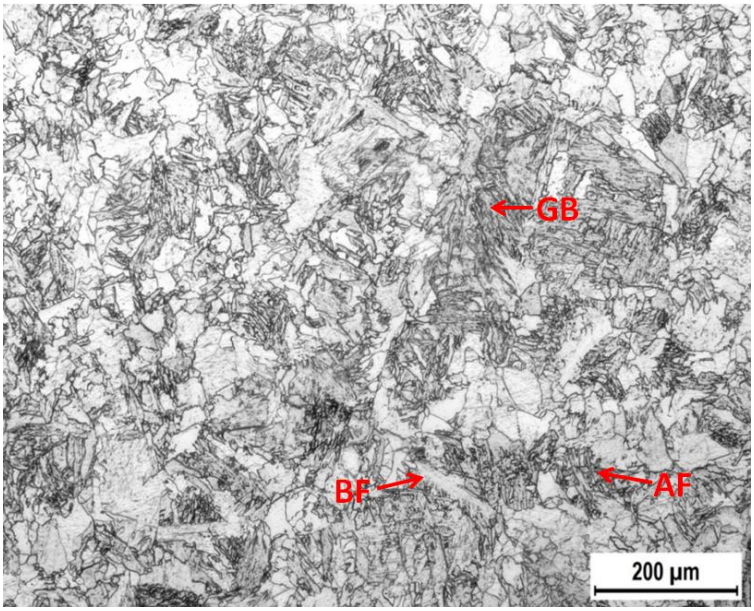

BF=bainitic ferrite; GB=granular bainite; AF=acicular ferrite

Figure 4.6 Optical micrograph showing the transformation of microstructure for the sample cooled from 900°C to the coiling temperature of 675°C at the cooling rate of 40°C/s under the condition of the 1280°C reheating temperature

Figure 4.7 is the dilatation curve of the sample which shows that austenite transformed to bainitic ferrite at the higher temperature range between 720 and 706°C and transformed to granular bainite at the lower temperature range between 677 and 640°C. The coiling temperature of 500°C is outside of the phase transformation temperature range and the coiling temperature of 675°C is within the range. The coiling temperatures of 500°C and 675°C were marked with red dotted lines in Figure 4.7.

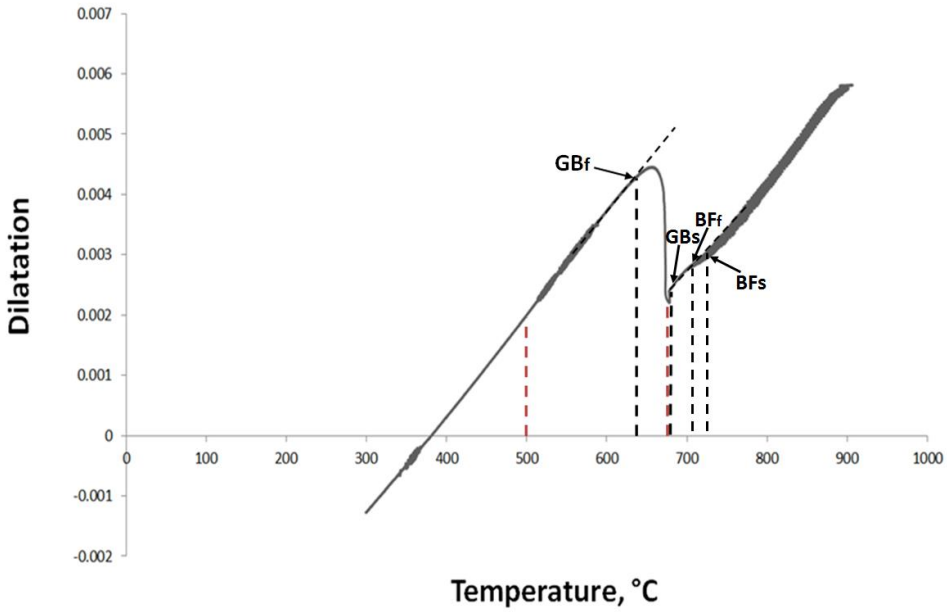

BF=bainitic ferrite; GB=granular bainite

Figure 4.7 Dilatation curve obtained for the sample at the cooling rate of 40°C/s with the coiling temperature of 675°C under the condition of the 1280°C reheating temperature

4.2 Microstructure, phase transformation and hardness of the samples solution treated at 1280°C and cooled from 900°C to the coiling temperature of 500°C at the cooling rates: 1 °C/s, 5°C/s and 40°C/s

4.2.1 The sample cooled at 1°C/s

Figure.4.8 shows typical microstructure of the sample cooled from 900°C to the coiling temperature of 500°C at 1°C/s and then cooled to 300°C at 0.17 °C/s. It is clear that there is no big difference between the microstructures of the samples at the coiling temperatures of 500 and 675°C. The dominant microstructure is still polygonal ferrite with a small amount of pearlite. The volume fraction of the polygonal ferrite is 95% and the size of the polygonal ferrite is 58 μm and the values are similar to the sample at the coiling temperature of 675°C. The Vickers hardness of the sample is 178HV1 and the micro Vickers hardness of the polygonal ferrite is 177HV0.05.

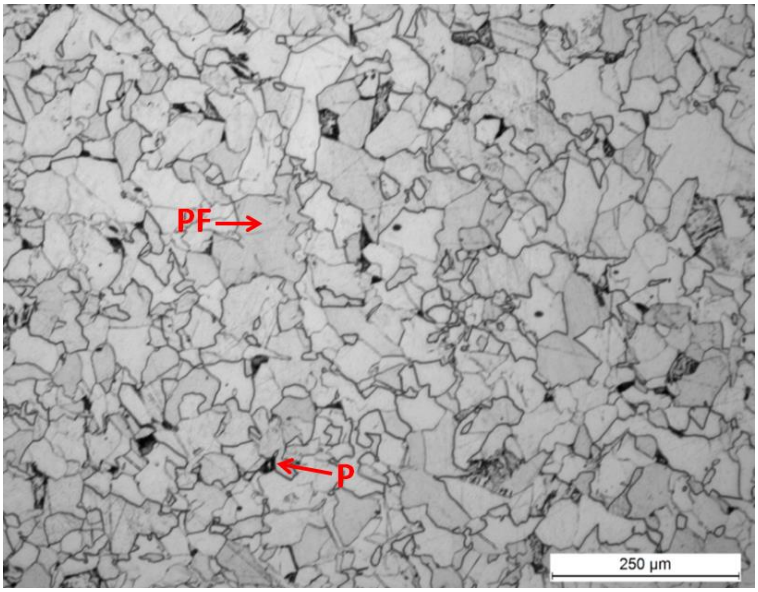

PF=polygonal ferrite; P=pearlite

Figure 4.8 Optical micrograph showing the transformation of microstructure for the sample cooled from 900°C to the coiling temperature of 500°C at the cooling rate of 1°C/s under the condition of the 1280°C reheating temperature

Figure 4.9 shows a dilatation curve for the sample which is similar to the dilatation curve of the sample cooled to the coiling temperature of 675°C at the same cooling rate of 1 °C/s. The austenite transformed into the polygonal ferrite during the cooling. The temperature range of the austenite to the polygonal ferrite phase transformation is between 802 and 643°C. Again the austenite to the pearlite transformation is not visible in the dilatation curve. Again the 500°C coiling temperature is also outside of the austenite to polygonal ferrite phase transformation temperature range, and the coiling temperature of 675°C is still within the range. The 500 and 675°C coiling temperatures were marked with the red dotted line in Figure 4.9.

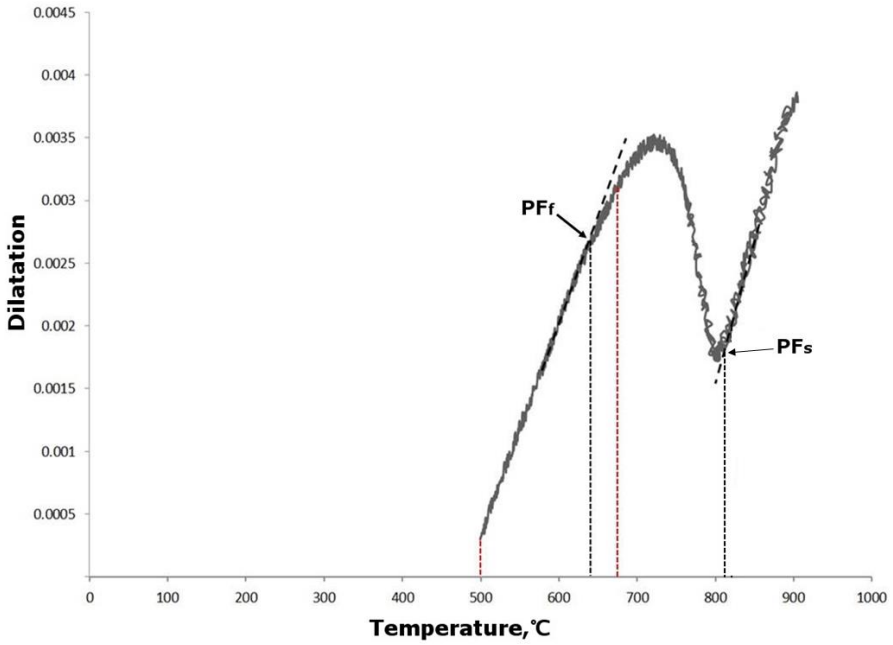

PF= polygonal ferrite

Figure 4.9 Dilatation curve obtained for the sample at the cooling rate of 1°C/s with the coiling temperature of 500°C under the condition of the 1280°C reheating temperature

4.2.2 The sample cooled at 5°C/s

The microstructure of the sample is shown in Figure 4.10 and it consists of polygonal ferrite and granular bainite. The bainite appears darker in the etched sample than the polygonal ferrite due to the high density grain boundaries it contained. The volume fractions of the polygonal ferrite and bainite are 71% and 29% respectively. The volume fraction of the polygonal ferrite decreased with the decrease of the coiling temperature from 675 to 500°C. The size of the polygonal ferrite is 47μm which is smaller than that of the sample cooled to the coiling temperature of 500°C at 1°C/s. The Vickers hardness of the sample is 198HV1 and the micro Vickers hardness of the polygonal ferrite and granular bainite are 185HV0.05 and 207HV0.05 respectively.

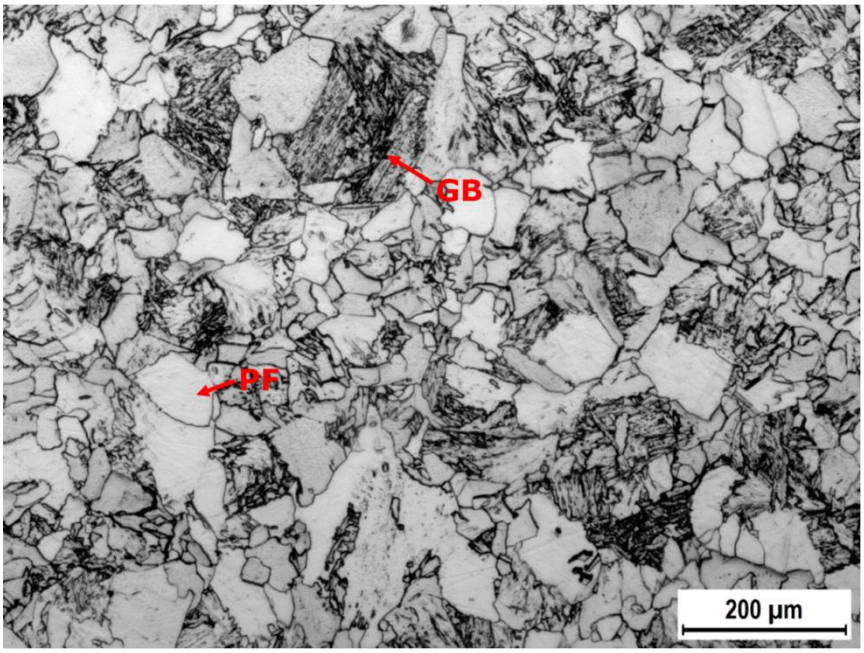

GB=granular bainite; PF=polygonal ferrite

Figure 4.10 Optical micrograph showing the transformation of microstructure for the sample cooled from 900°C to the coiling temperature of 500°C at the cooling rate of 5°C/s under the condition of the 1280°C reheating temperature

The dilatation curve of the sample is given in Figure 4.11. Some of the austenite transformed firstly into the polygonal ferrite at the higher temperatures between 786 and 731°C and the rest of the austenite transformed into granular bainite at the lower temperatures between 674 and 618°C. The coiling temperature of 500°C is also outside of the both phase transformation temperature ranges and the coiling temperature of 675°C is above the austenite to granular bainite transformation temperature range. The coiling temperatures of 500 and 675°C were marked with red dotted lines in Figure 4.11.

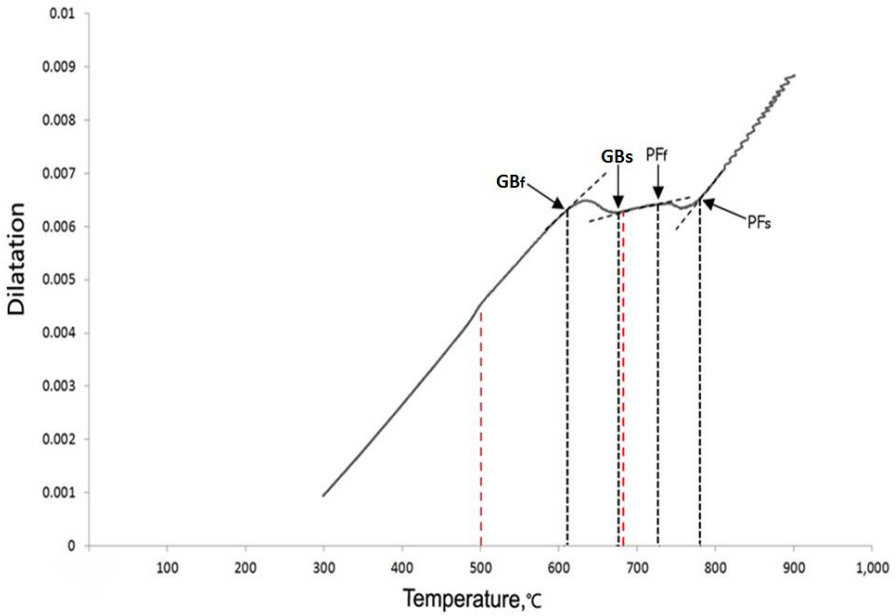

GB=granular bainite; PF= polygonal ferrite

Figure 4.11 Dilatation curve obtained for the sample at the cooling rate of 5°C/s with the coiling temperature of 500°C under the condition of the 1280°C reheating temperature

4.2.3 The sample cooled at 40°C/s

Figure 4.12 reveals the microstructure of the sample and the microstructure consists of mainly granular bainite and acicular ferrite with a small amount of bainitic ferrite at

the pre-austenite grain boundaries. The volume fraction of the granular bainite and acicular ferrite is 61% and the bainitic ferrite is only 39%. The volume fraction of the bainitic ferrite decreases with the decrease of the coiling temperature from 675 to 500°C. The Vickers hardness of the sample is 201HV1 and the micro Vickers hardness of the granular bainite is 230HV0.05.

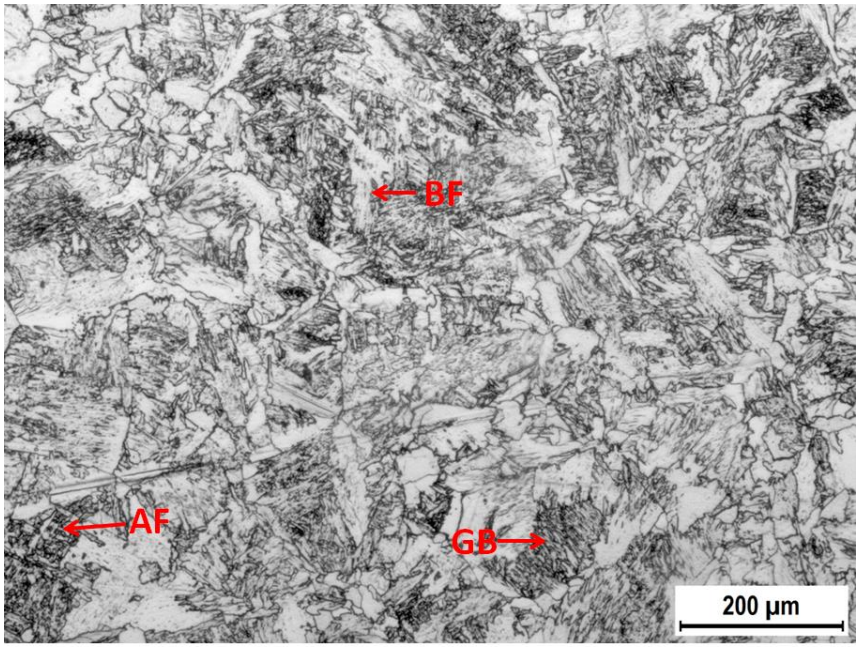

BF=bainitic ferrite; GB=granular bainite; AF=acicular ferrite

Figure 4.12 Optical micrograph showing the transformation of microstructure for the sample cooled from 900°C to the coiling temperature of 500°C at the cooling rate of 40°C/s under the condition of the 1280°C reheating temperature

The dilatation curve of the sample is given in Figure 4.13 which shows austenite transformed to bainitic ferrite at the higher temperature range between 720 and 706°C and transformed to granular bainite at the lower temperature range between 687 to 538°C. Again the coiling temperature of 500°C is outside of the phase transformation

temperature range, and the coiling temperature of 675°C is within the range. The coiling temperatures of 500 and 675°C were marked with red dotted lines in Figure 4.13.

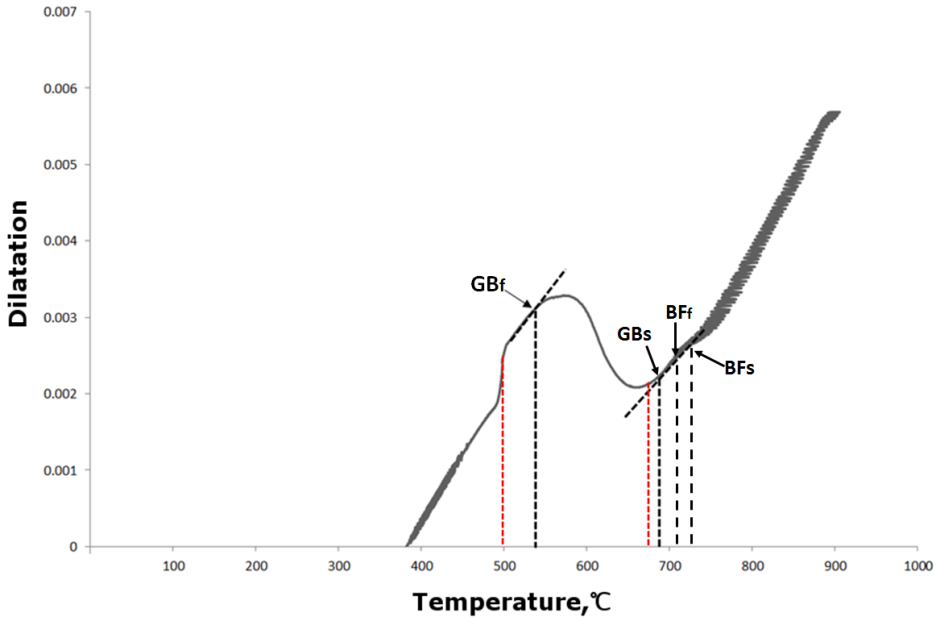

BF=bainitic ferrite; GB=granular bainite

Figure 4.13 Dilatation curve obtained for the sample at the cooling rate of 40°C/s with the coiling temperature of 500°C under the condition of the 1280°C reheating temperature

4.3 Microstructure, phase transformation and hardness of the samples solution treated at 1150°C and cooled from 900°C to the coiling temperature of 675°C at the cooling rates: 1 °C/s, 5°C/s and 40°C/s

4.3.1 The sample cooled at 1°C/s

Figure. 4.14 shows typical microstructure of the sample and the microstructure consist of 99% polygonal ferrite and 1% pearlite in terms of volume fraction. The size of

polygonal ferrite is about 50 μm. The Vickers hardness of the sample is 182HV1 and the micro Vickers hardness of the polygonal ferrite is 182HV0.05.

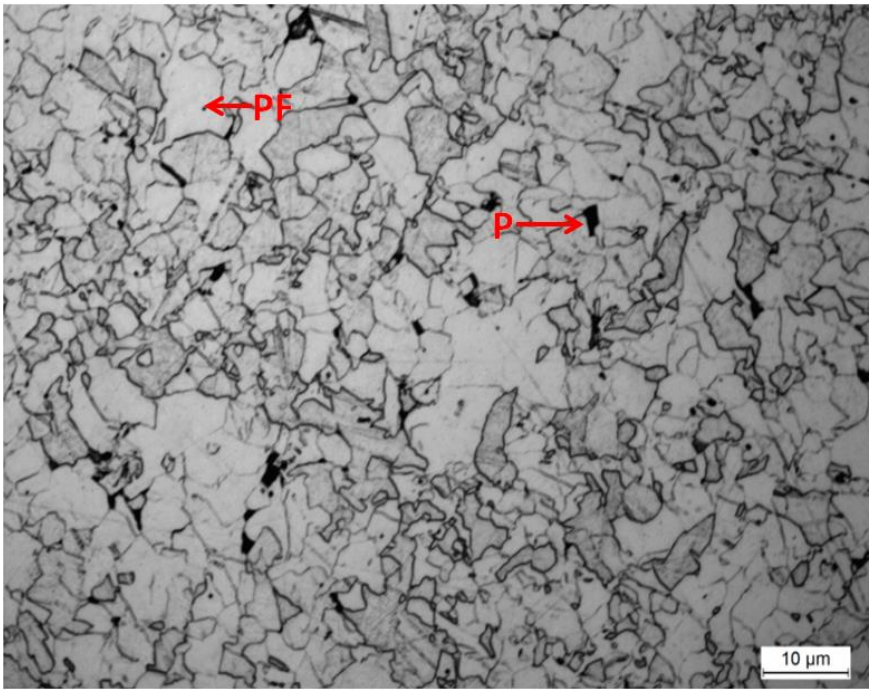

PF=polygonal ferrite; P=pearlite

Figure 4.14 Optical micrograph showing the transformation of microstructure for the sample cooled from 900°C to the coiling temperature of 675°C at the cooling rate of 1°C/s under the condition of the 1150°C reheating temperature

Figure 4.15 is a dilatation curve of the sample which shows that there is one phase transformation between 824 and 670°C. The transformation is austenite to polygonal ferrite. It is noted that the coiling temperature of 500°C is outside of the phase transformation temperature range and the coiling temperature of 675°C is within the

range. The 500 and 675°C coiling temperatures were marked with red dotted lines in Figure 4.15.

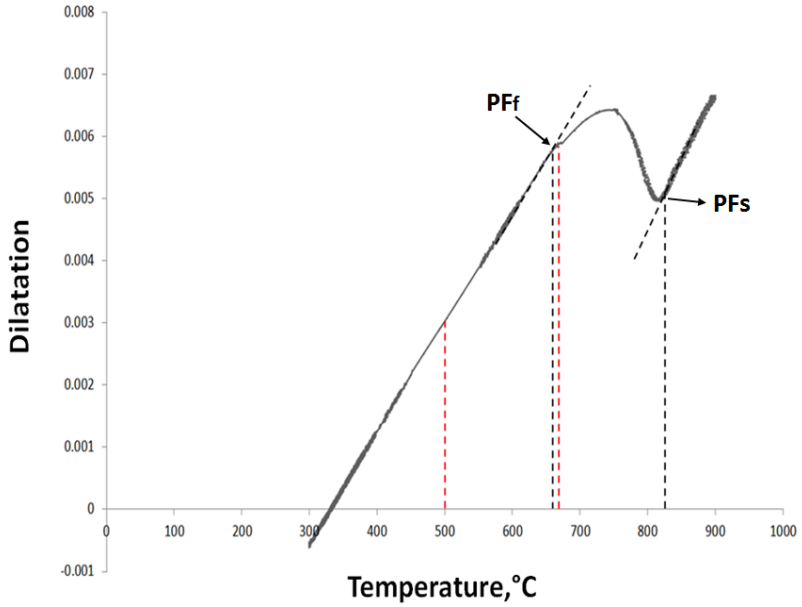

PF= polygonal ferrite

Figure 4.15 Dilatation curve obtained for the sample at the cooling rate of 1°C/s with the coiling temperature of 675°C under the condition of the 1150°C reheating temperature

4.3.2 The sample cooled at 5°C/s

The microstructure of the sample is given in Figure 4.16. The microstructure consists of mainly polygonal ferrite with a small amount of pearlite and granular bainite. The volume fraction of the polygonal ferrite is 85% and the rests about 15% are the granular bainite and pearlite. The size of the polygonal ferrite is about 35μm which is lower than that of the sample cooled to the coiling temperature of 675°C at 1°C/s. The Vickers

hardness of the sample is 208HV1 and the micro Vickers hardness of the polygonal ferrite and granular bainite are 208HV0.05 and 230HV0.05 respectively.

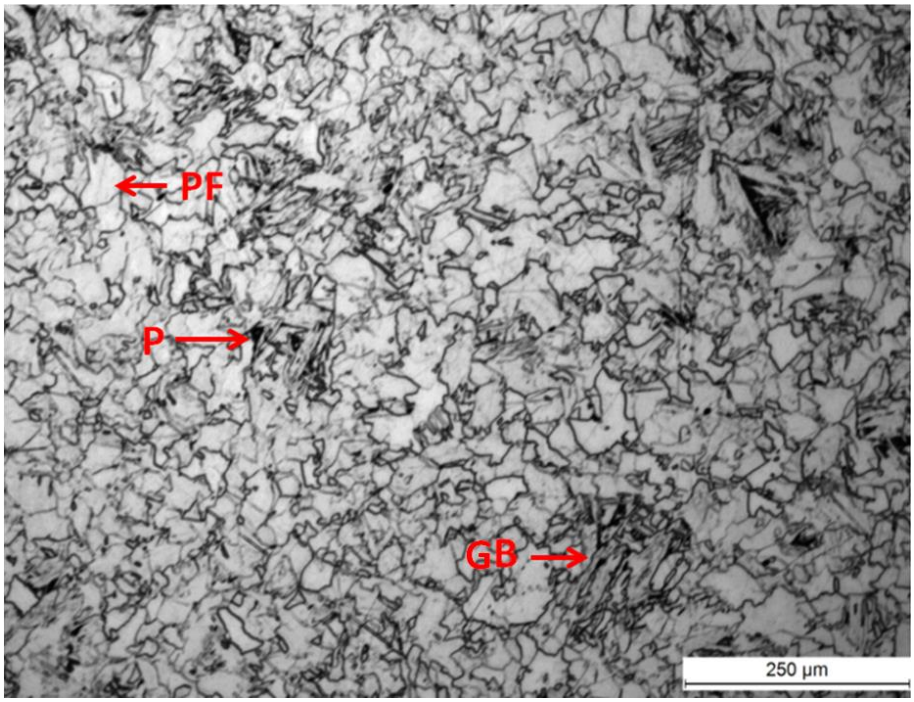

GB=granular bainite; PF=polygonal ferrite; P=pearlite

Figure 4.16 Optical micrograph showing the transformation of microstructure for the sample cooled from 900°C to the coiling temperature of 675°C at the cooling rate of 5°C/s under the condition of the 1150°C reheating temperature

The dilatation curve of the sample is given in Figure 4.17 which shows two phase transformations: the first one started at 791°C and finished 748°C and the second one started at 682°C and finished at 660°C. The former is the austenite to polygonal ferrite transformation and the latter is the austenite to pearlite and granular bainite. Again the coiling temperature of 500°C is outside of the two phase transformation temperature

range, however, the coiling temperature of 675°C is within the austenite to granular bainite transformation temperature range. The 500 and 675°C coiling temperatures were marked with dashed red lines in Figure 4.17.

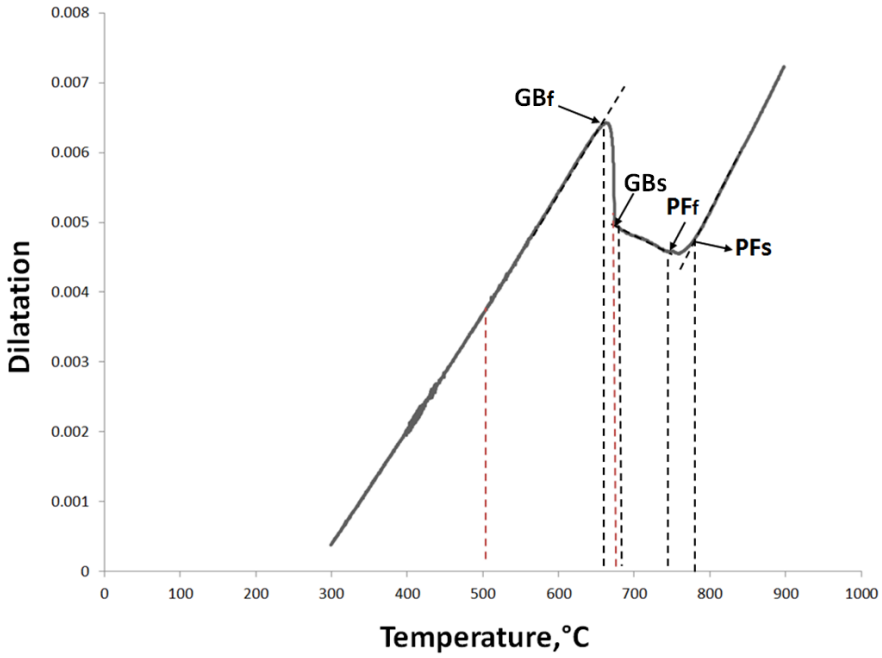

GB=granular bainite; PF= polygonal ferrite

Figure 4.17 Dilatation curve obtained for the sample at the cooling rate of 5°C/s with the coiling temperature of 675°C under the condition of the 1150°C reheating temperature

4.3.3 The sample cooled at 40°C/s

The microstructure of the sample is shown in Figure 4.18 and the microstructure consists of granular and acicular ferrite and bainitic ferrite. The volume fraction of granular bainite and acicular ferrite is up to 49% while the value of the bainitic ferrite is 51%. The Vickers hardness of the sample is 209HV1 and the micro Vickers hardness of the granular bainite is 220HV0.05.

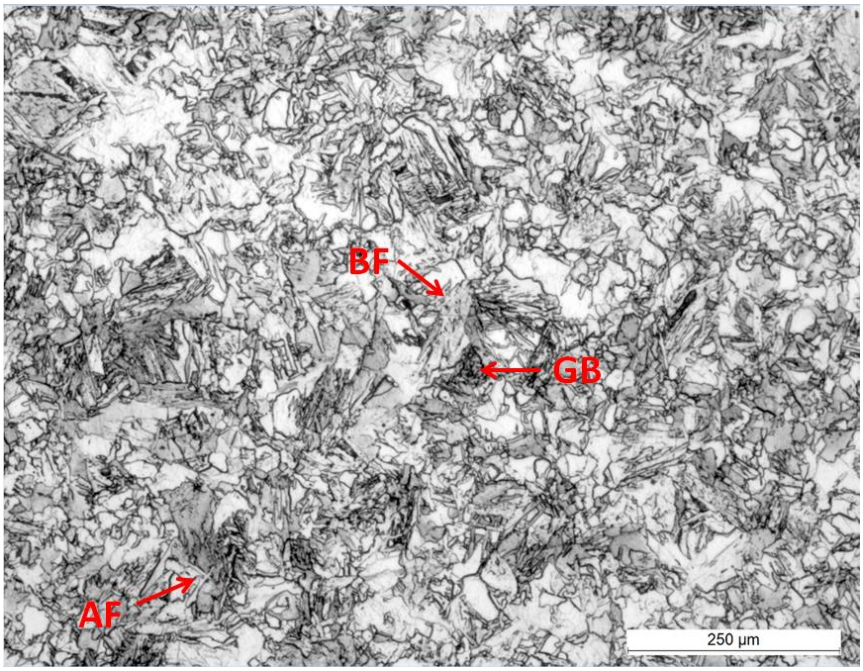

BF=bainitic ferrite; GB=granular bainite; AF=acicular ferrite

Figure 4.18 Optical micrograph showing the transformation of microstructure for the sample cooled from 900°C to the coiling temperature of 675°C at the cooling rate of 40°C/s under the condition of the 1150°C reheating temperature

The dilatation curve of the sample is given in Figure 4.19 which shows only one phase transformation. The dilatation curve does not show detailed information about austenite to bainitic ferrite, granular bainite or acicular ferrite phase transformation. The transformation temperature range for the austenite to granular bainite is between 725°C and 640°C. The coiling temperature of 500°C is outside of the phase transformation temperature range and the coiling temperature of 675°C is within the range. The coiling temperatures of 500 and 675°C were marked with red dotted lines in Figure 4.19.

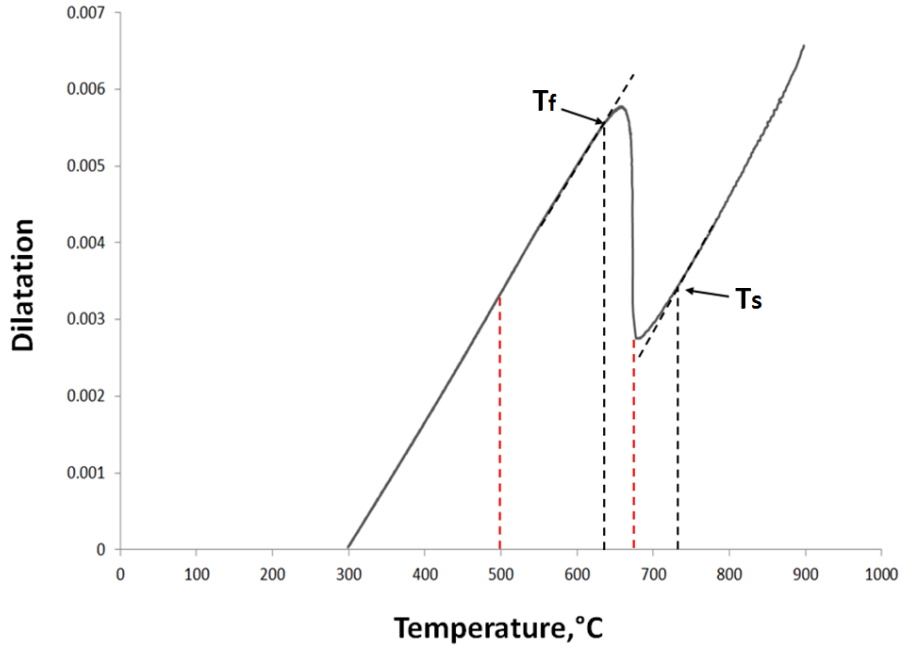

Ts=phase transformation start temperature; Tf=phase transformation finish temperature

Figure 4.19 Dilatation curves obtained for the sample at the cooling rate of 40°C/s with the coiling temperature of 675°C under the condition of the 1150°C reheating temperature

4.4 Microstructure, phase transformation and hardness of the samples solution treated at 1150°C and cooled from 900°C to the coiling temperature of 500°C at the cooling rates: 1 °C/s, 5°C/s and 40°C/s

4.4.1 The sample cooled at 1°C/s

Figure 4.20 shows typical microstructure of the sample. The microstructure consists of 97% polygonal ferrite with a small amount of pearlite in terms of volume fraction and the size of the polygonal ferrite is about 37 μm. The Vickers hardness of the sample is 181HV1 and the micro Vickers hardness of the polygonal ferrite is 178HV0.05.

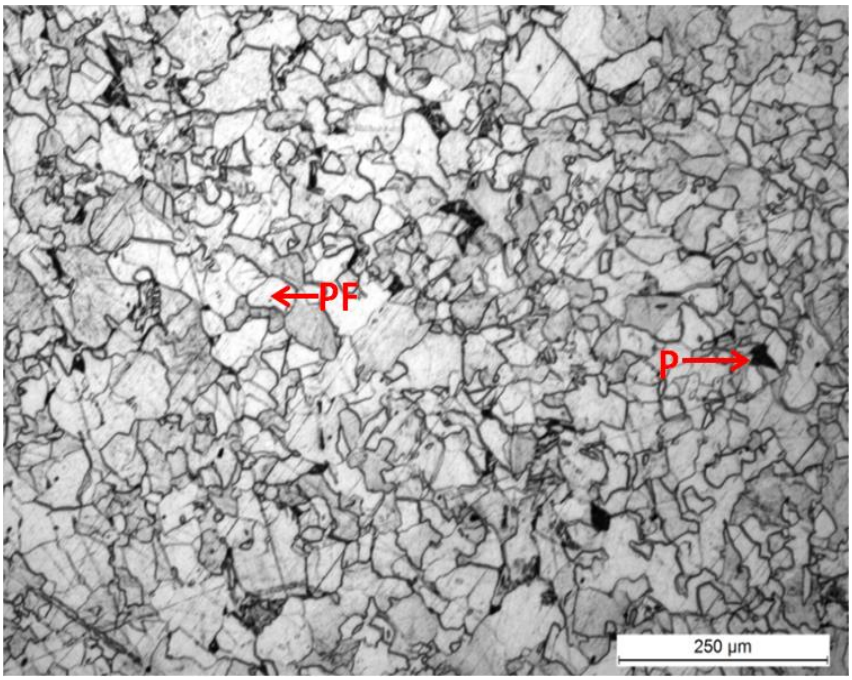

PF=polygonal ferrite; P=pearlite

Figure 4.20 Optical micrograph showing the transformation of microstructure for the sample cooled from 900°C to the coiling temperature of 500°C at the cooling rate of 1°C/s under the condition of the 1150°C reheating temperature

The dilatation curve of the sample is given in Figure 4.21 which shows only one phase transformation: austenite transformed into the polygonal ferrite during the cooling. The temperature range of the austenite to polygonal ferrite phase transformation started at 824°C and ended at 657°C. Again the austenite to the pearlite transformation is not visible in the dilatation curve. Again the 500°C coiling temperature is also outside of the austenite to polygonal ferrite phase transformation temperature range and the coiling temperature of 675°C is still within the range. The 500 and 675°C coiling temperatures were marked with the red dotted lines in Figure 4.21.

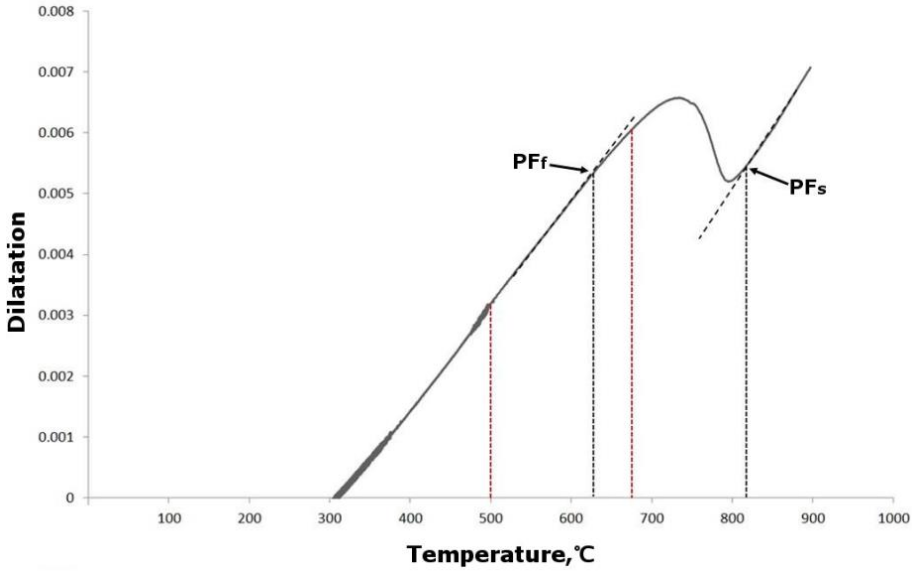

PF= polygonal ferrite

Figure 4.21 Dilatation curve obtained for the sample at the cooling rate of 1°C/s with the coiling temperature of 500°C under the condition of the 1150°C reheating temperature

4.4.2 The sample cooled at 5°C/s

The microstructure of the sample is shown in Figure 4.22 and it consists of polygonal ferrite and granular bainite. The volume fractions of the polygonal ferrite and granular bainite are 71% and 29% respectively. The size of the polygonal ferrite is 36 μm which is lower than that of the sample cooled to 500°C at 1°C/s. The Vickers hardness of the sample is 188HV1 and the micro Vickers hardness of the polygonal ferrite and granular bainite are 183HV0.05 and 199HV0.05 respectively.

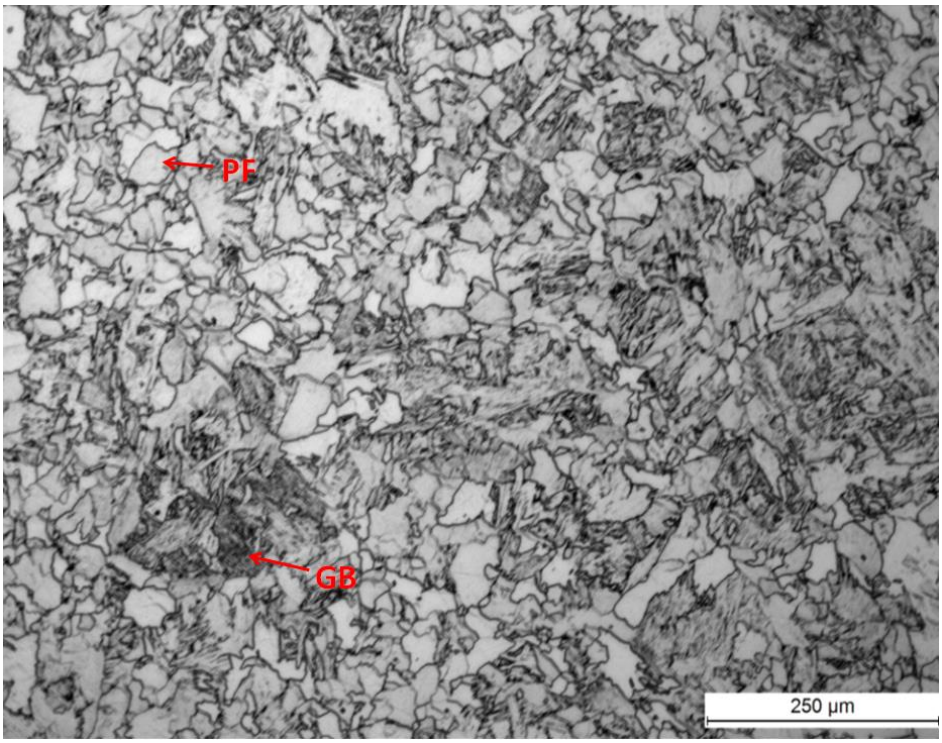

GB=granular bainite; PF=polygonal ferrite

Figure 4.22 Optical micrograph showing the transformation of microstructure for the sample cooled from 900°C to the coiling temperature of 500°C at the cooling rate of 5°C/s under the condition of the 1150°C reheating temperature

Figure 4.23 shows a dilatation curve of the sample and it shows two phase transformations: some of the austenite transformed firstly into the polygonal ferrite at the higher temperatures and the rest of the austenite transformed into granular bainite at the lower temperatures. The transformation temperature ranges are between 791°C and 708°C for the austenite to the polygonal ferrite and between 681 and 611°C for the austenite to the granular bainite. The coiling temperature of 500°C is also outside of the two transformation temperature ranges and the coiling temperature of 675°C is within the austenite to granular bainite transformation temperature range. The coiling temperatures of 500 and 675°C are marked with red dotted lines in Figure 4.23.

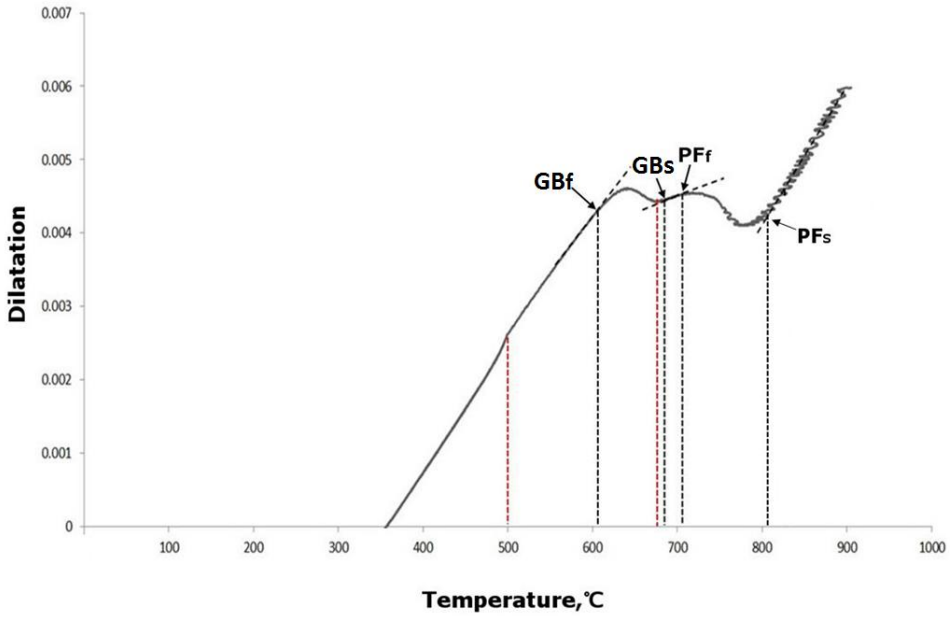

GB=granular bainite; PF= polygonal ferrite

Figure 4.23 Dilatation curves obtained for the sample at the cooling rate of 5°C/s with the coiling temperature of 500°C under the condition of the 1150°C reheating temperature

4.4.3 The sample cooled at 40°C/s

The microstructure of the sample is presented in Figure 4.24 and it consists of mainly granular bainite and acicular ferrite at about 62% volume fraction and 38% of bainitic ferrite at the pre-austenite grain boundaries. The Vickers hardness of the sample is 220HV1 and the micro Vickers hardness of the granular bainite is 230HV0.05.

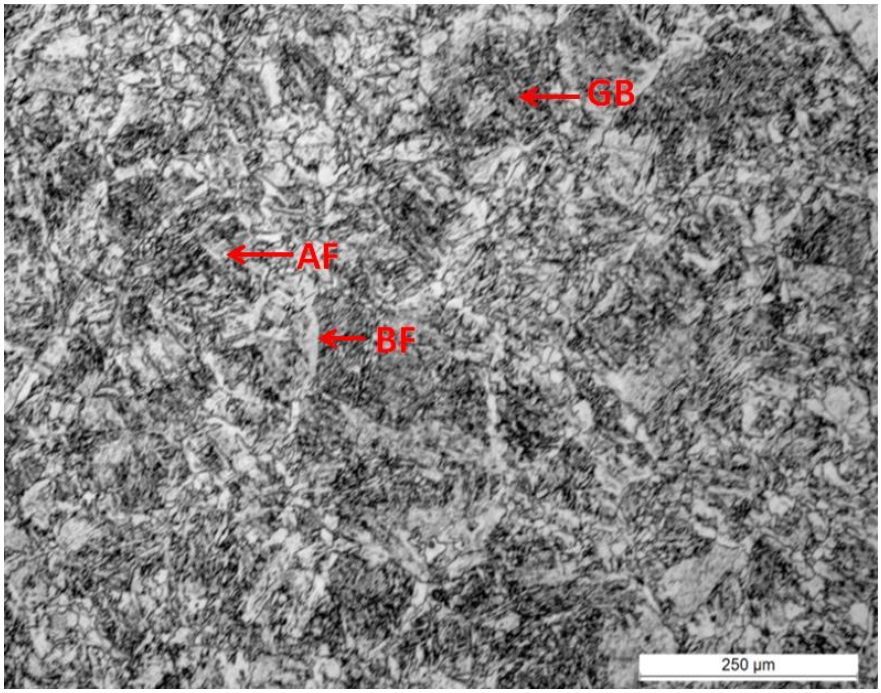

BF=bainitic ferrite; GB=granular bainite; AF=acicular ferrite

Figure 4.24 Optical micrograph showing the transformation of microstructure for the sample cooled from 900°C to the coiling temperature of 500°C at the cooling rate of 40°C/s under the condition of the 1150°C reheating temperature

The dilatation curve of the sample is shown in Figure 4.25 which reveals only one phase transformation, austenite to granular bainite. The transformation temperature range for the austenite to the granular bainite is between 725 and 550°C. Again the coiling temperature of 500°C is outside of the phase transformation temperature range and the coiling temperature of 675°C is within the range. The coiling temperatures of 500 and 675°C were marked with red dotted lines in Figure 4.25.

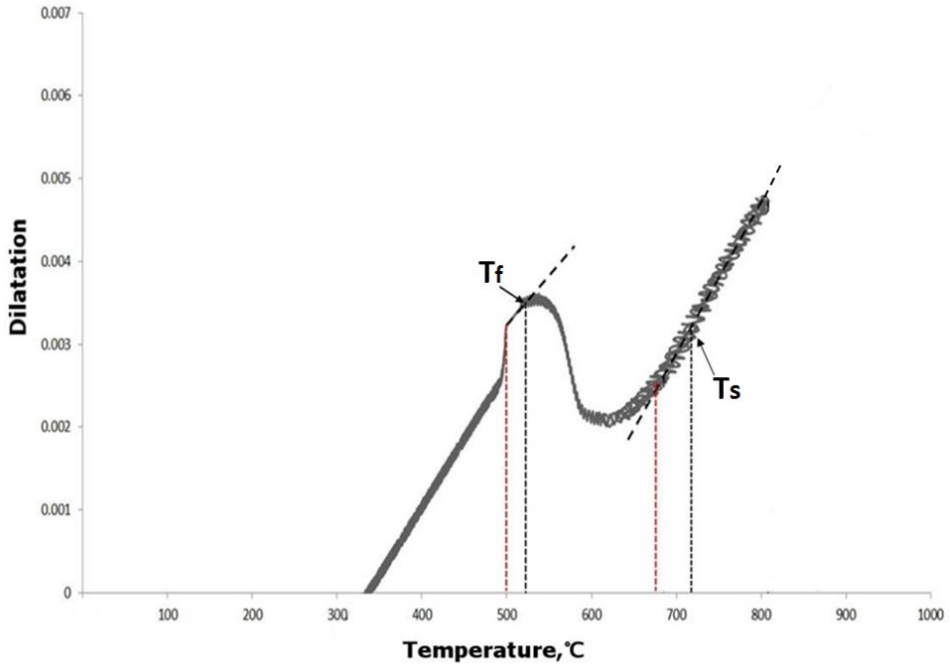

Ts=phase transformation start temperature; Tf=phase transformation finish temperature

Figure 4.25 Dilatation curves obtained for the sample at the cooling rate of 40°C/s with the coiling temperature of 500°C under the condition of the 1150°C reheating temperature

4.5 Vickers hardness of the sample and the micro Vickers hardness of the constituent after age hardening

After the age hardening heat treatment, the Vickers hardness of the samples and micro Vickers hardness of the constituent in various cooling conditions under the conditions of 1150 and 1280°C reheating temperatures are shown in Tables 4.1 and 4.2.

Table 4.1 The Vickers hardness of the samples in various cooling conditions under the conditions of 1150 and 1280°C reheating temperatures after age hardening

Cooling Rate (°C/s)	Coiling Temperature (°C)	Vickers hardness(HV1) After age hardening	
		1150°C	1280°C
1	500°C	216	205
5	500°C	223	224
40	500°C	269	233
1	675°C	206	206
5	675°C	229	211
40	675°C	229	212

Table 4.2 The micro Vickers hardness of the constituent in various cooling conditions under the conditions of 1150 and 1280°C reheating temperatures after age hardening

Cooling rate(°C/s)	Coiling Temperature(°C)	Micro Vickers hardness(HV0.05) After age hardening			
		1150°C		1280°C	
		PF	GB	PF	GB
1	500	205	-	206	-
5	500	215	242	216	243
40	500	-	281	-	263
1	675	206	-	217	-
5	675	226	247	220	238
40	675	-	252	-	239

GB=granular bainite; PF= polygonal ferrite

4.6 Result summary

4.6.1 The effect of cooling rate and coiling temperature on phase transformation

The microstructures of all the samples solution treated at 1280°C are summarised in Table 4.3 and the microstructures of all the samples solution treated at 1150°C are summarised in Table 4.4. Regardless of the different solution temperature, at the same coiling temperature, more bainite and acicular ferrite and less polygonal ferrite were produced in the sample with the increase of the cooling rate. At the same cooling rate, more polygonal ferrite or bainitic ferrite were produced in the sample with the higher coiling temperature of 675°C compared to the sample at the coiling temperature of 500°C.

Table 4.3 Proportion of each constituent for the samples with the different cooling rates and coiling temperatures under the condition of 1280°C reheating temperature

Cooling rate(°C/s)	1	5	40	1	5	40
Coiling T(°C)	500	500	500	675	675	675
Matrix (vol. %)	PF (95%) P (5%)	PF (71%) GB (29%)	BF (39%) GB+AF (61%)	PF (98%) P (2%)	PF (95%) B+P (5%)	BF (45%) GB+AF (55%)

PF=polygonal ferrite; GB=granular baintie; BF=bainitic ferrite; AF=acicular ferrite; P=pearlite.

Table 4.4 Proportion of each constituent for the samples with the different cooling rates and coiling temperatures under the condition of the 1150°C reheating temperature

Cooling rate(°C/s)	1	5	40	1	5	40
Coiling T(°C)	500	500	500	675	675	675
Matrix (vol. %)	PF (97%) P (3%)	PF (71%) GB (29%)	BF (38%) GB+AF (62%)	PF (99%) P (1%)	PF (85%) B+P (15%)	BF (51%) GB+AF (49%)

PF=polygonal ferrite; GB=granular baintie; BF=bainitic ferrite; AF=acicular ferrite; P=pearlite.

4.6.2 The influence of the cooling rate and coiling temperature on micro Vickers hardness of each constituent and Vickers hardness of the sample

Under the condition of the 1280°C reheating temperature, the micro Vickers hardness of the polygonal ferrite and granular bainite and the Vickers hardness of the samples in the various cooling conditions before and after the age hardening heat treatment are given in Tables 4.5 and 4.6 respectively. It is clear to see that at the same cooling rate, the age hardening increased as the coiling temperature decreases from 675 to 500°C. At the coiling temperature of 500°C, the age hardening increased as the cooling rate

increased from 1 or 5 to 40°C/s, however, at coiling temperature of 675°C, the age hardening decreased with the increase of the cooling rate.

Table 4.5 Vickers hardness of the samples at 1280°C reheating temperature from Vickers hardness tester with 1kg load before and after age hardening

Cooling Rate, Coiling Temperature	Vickers Hardness (HV1)		Hardness increment
	Before age hardening	After age hardening	
1°C/s, 500°C	178±7	205±9	27
5°C/s, 500°C	198±8	224±6	26
40°C/s, 500°C	201±8	233±4	32
1°C/s, 675°C	191±9	206±7	15
5°C/s, 675°C	201±8	211±7	10
40°C/s, 675°C	204±7	212±3	8

Similar results were also obtained in the micro Vickers hardness experiments as shown in Table 4.6. At the same cooling rate, more age hardening was observed in the polygonal ferrite or granular bainite in the samples having the low coiling temperature of 500°C than the polygonal ferrite or granular ferrite in the sample having the high coiling temperature of 675°C. Taking the 5°C/s cooling rate as an example, the aging hardness increments of the polygonal ferrite and granular bainite of the sample at the coiling temperature of 500°C are 31HV0.05 and 36HV0.05 respectively, which are much higher than 17HV0.05 and 17HV0.05 hardness increments of the polygonal ferrite and granular bainite of the sample having the coiling temperature of 675°C. Under the condition of the same coiling temperature, the aging hardness increment of

the polygonal ferrite of the sample having the coiling temperature of 675°C increased with the decrease of the cooling rate as shown in Table 4.6. At the cooling rate of 1°C/s, the hardness increment of the polygonal ferrite is 25HV0.05, in contrast, the hardness increment of the polygonal ferrite of the sample at 5°C/s cooling rate is relatively low and the value is 17 HV0.05.

Table 4.6 Micro Vickers hardness of the constituent of the sample from Micro Vickers hardness tester with 50g load before and after age hardening

Cooling rate(°C/s)	Coiling Temperature(°C)	Hardness(HV0.05) Before age hardening		Hardness(HV0.05) After age hardening		Hardness increment (HV0.05)	
		PF	GB	PF	GB	PF	GB
1	500	177±3	-	206±4	-	29	-
5	500	185±6	207±8	216±9	243±8	31	36
40	500	-	230±5	-	263±7	-	33
1	675	192±4	-	217±3	-	25	-
5	675	203±6	221±9	220±8	238±5	17	17
40	675	-	227±6	-	239±5	-	16

PF=polygonal ferrite; GB=granular bainite

The micro Vickers hardness of the constituent and Vickers hardness of the samples with the 1150°C reheating temperature showed the same trend as the samples with the 1280°C reheating temperature as shown in Tables 4.7 and 4.8.

Table 4.7 Micro Vickers hardness of the constituent of the sample at 1150°C reheating temperature from Micro Vickers hardness tester with 50g load before and after age hardening

Cooling rate(°C/s)	Coiling Temperature(°C)	Hardness(HV0.05) Before age hardening		Hardness(HV0.05) After age hardening		Hardness increment (HV0.05)	
		PF	GB	PF	GB	PF	GB
1	500	178±4	-	205±7	-	27	-
5	500	183±5	199±3	215±7	242±5	32	43
40	500	-	230±6	-	281±4	-	51
1	675	182±7	-	206±5	-	24	-
5	675	208±4	230±5	226±6	247±4	18	17
40	675	-	220±6	-	252±3	-	20

PF=polygonal ferrite; GB=granular bainite

Table 4.8 Vickers hardness of the samples at 1150°C reheating temperature from Vickers hardness tester with 1kg load before and after age hardening

Cooling Rate, Coiling Temperature	Vickers Hardness (HV0.05)		Hardness increment
	Before age hardening	After age hardening	
1°C/s, 500°C	181±5	216±7	35
5°C/s, 500°C	188±3	223±4	35
40°C/s, 500°C	220±3	269±4	49
1°C/s, 675°C	182±5	206±5	24
5°C/s, 675°C	208±4	229±6	21
40°C/s, 675°C	209±4	229±3	20

4.6.3 The influence of reheating temperature on the austenite grain size and phase transformation

The prior austenite grain size of the sample at 1150°C or 1280°C reheating temperature was measured three times and the final austenite grain size was obtained by averaging the results from three measurements in the experiment as shown in Tables 4.9 and 4.10 and the values are 118 µm and 179 µm respectively. The prior austenite grain size increases with the increase of the reheating temperature.

Table 4.9 Austenite grain size for the sample at the 1150°C reheating temperature

	1	2	3	average
Average grain size(μm)	125.4	115	114	118±7

Table 4.10 Austenite grain size for the sample at the 1280°C reheating temperature

	1	2	3	average
Average grain size(μm)	184.93	188.94	163.13	179±16

The phase transformation start and finish temperatures of the samples at 1150°C or 1280°C reheating temperature in various cooling conditions were measured from dilatation curve and the results are summarised in Table 4.11. It is clear that the phase transformation start temperature of the most of the samples at 1150°C reheating temperature is higher than that of the samples at 1280°C reheating temperature at the same other heat treatment condition and the phase transformation finish temperature of the most of the samples at 1150°C reheating temperature is also higher than that of the samples at 1280°C reheating temperature in the same cooling condition, which means that the γ-α phase transformation temperature range increases with the decrease of the reheating temperature.

Table 4.11 Phase transformation temperatures for samples in various cooling conditions

Cooling Rate (°C/s)	Coiling Temperature (°C)	Reheating Temperature(℃)			
		1150		1280	
		Ts	Tf	Ts	Tf
1	500°C	824±1℃	657±1℃	802±1℃	643±1℃
5	500°C	791±1℃	611±1℃	786±1℃	618±1℃
40	500°C	725±1℃	550±1℃	677±1℃	538±1℃
1	675°C	824±1℃	670±1℃	801±1℃	668±1℃
5	675°C	791±1℃	660±1℃	786±1℃	670±1℃
40	675°C	725±1℃	640±1℃	677±1℃	640±1℃

5 Discussions

The objective of the experiment is to study the influence of the different cooling conditions on the retention of Nb in the strip produced during CASTRIP process. The investigation was carried out based on the fact that the age hardening of the strip is closely related to the retention of Nb atoms in the strip. The reason is that more precipitates are likely produced during the age hardening if more Nb atoms are retained in the solid solution before the age hardening. It is known that in HSLA steel NbC most likely to precipitate in the γ-α phase transformation temperature range [2]. The reason is that a great number of carbon and Nb atoms segregate from the solid solution as the austenite transformed into the ferrite due to the large solubility difference of carbon and Nb atoms between the austenite and ferrite. Therefore the longer the strip stays in the $\gamma \rightarrow \alpha$ transformation temperature range the more NbC likely to precipitate and the less retention of Nb in the strip.

5.1 The influence of the reheating temperature on the retention of Nb

The reheating temperature can influence the retention of Nb in the strip by the change of the prior austenite grain size which in turn affects the $\gamma \rightarrow \alpha$ phase transformation temperature range. It is clear from Table 5.1 that the age hardening effect of the samples at the reheating temperature of 1280°C is lower than that of the samples solution treated at 1150°C, which means that fewer Nb atoms were retained in the samples solution treated at 1280°C before the age hardening. As expected that the $\gamma \rightarrow \alpha$ phase transformation temperature range decreased as the reheating temperature increased from 1150 to 1280°C. The retention of Nb atoms in the samples was influenced by the change of the phase transformation temperature range. It is possible that the lower phase

transformation temperature range of the samples solution treated at 1280°C is more superimposed with the NbC precipitation range than the higher phase transformation temperature range of the samples solution treated at 1150°C. Therefore, more NbC precipitates were produced and fewer Nb atoms were left in the samples solution treated at 1280°C reheating temperature compared to the samples solution treated at 1150°C reheating temperature.

Table 5.1 Results summary of the samples in γ-α phase transformation temperature range at various cooling conditions under the condition of 1150℃ or 1280℃ reheating temperature

Cooling Rate (°C/s)	Coiling Temperature (°C)	Phase Transformation Temperature Range(°C)		Dwelling Time(s)		Age Hardening (HV1)	
		1150°C	1280°C	1150°C	1280°C	1150°C	1280°C
1	500	818-620	802-643	198	159	35	27
5	500	805-605	786-615	40	34	35	26
40	500	725-520	720-538	5	5	49	32
1	675	824-670	801-668	178	167	24	15
5	675	791-660	786-670	111	52	21	10
40	675	725-640	720-640	207	207	20	8

5.2 The influence of the cooling rate on the Nb retention

Since the coiling temperature of 500°C is outside of the γ-α phase transformation temperature range in all the samples, the dwelling time of the samples in the phase transformation range mainly depends on the cooling rate. The higher the cooling rate the

shorter the dwelling time and thus the less the NbC precipitation and the more Nb retained in the samples. Thus it is expected that more Nb will be retained in the samples cooled at the high cooling rate of 40°C/s than the samples cooled at the lower cooling rates of 1 and 5°C/s.

Table 5.1 summarized the $\gamma \rightarrow \alpha$ phase transformation range, dwelling time and age hardening at the two different reheating temperatures, three different cooling rates and two different coiling temperatures. As expected that at the same coiling temperature of 500°C, the age hardening of the samples cooled at 40°C/s is 32HV1 with the reheating temperatures of 1280°C, which is higher than 27HV1 and 26HV1 of the samples cooled at the cooling rates of 1 and 5°C/s with the same reheating temperature. At the cooling rate of 40°C/s, the dwelling time of the samples in the γ-α phase transformation temperature range is short so that there was less time for NbC to precipitate. The dwelling times of the samples cooled at 40°C/s under the condition of 1150 and 1280°C reheating temperature are only 4 and 5s respectively, which are much shorter than that of the samples cooled at 1 and 5°C/s having the same reheating temperature.

The coiling temperature of 675°C is within γ-α phase transformation temperature range of the samples and it makes things more complicated, for example, more Nb was retained in the sample cooled at 1°C/s compared to the samples at the higher cooling rates of 5 and 40°C/s, which was not totally expected.

However if the details of the $\gamma \rightarrow \alpha$ phase transformation is analysed it was found that at the cooling rate of 1°C/s, almost all the austenite transformed into the polygonal ferrite before the 675°C coiling temperature as shown in Figure 4.2. For this reason, there was nearly no austenite left in the sample below 675°C. Therefore, even if the cooling rate is very slow after the coiling temperature of 675°C, there was virtually little phase transformation. Therefore, the γ-α phase transformation mainly occurred before

the coiling temperature of 675°C for the sample at 1°C/s. In contrast, the samples cooled at the higher cooling rate such as 40°C/s, some of the austenite transformed into the bainitic ferrite before the coiling temperature of 675°C as shown in Figure 4.7. A larger volume fraction of the austenite transformed into the granular bainite at the temperature range below 675°C at the cooling rate of 0.17 °C/s. Such a slow cooling rate will enable more Nb to precipitate out as NbC and thus less Nb was retained in the solid solution for the age hardening. Therefore more Nb was retained in the samples cooled at 1 °C/s to the coiling temperature of 675 °C than in the sample cooled at 5 or 40°C/s to the coiling temperature of 675°C. Furthermore it is well known that the nucleation sites of the precipitate are dislocations and grain boundaries and the volume fraction of dislocations in the bainite would be much more than that in the polygonal ferrite [68-70]. There were more nucleation sites for NbC precipitate during the γ-α phase transformations for the samples at 40°C/s owing to the granular bainite produced during the phase transformation. The nucleation rate of the precipitate in the sample cooled at 40°C/s would be faster than the sample cooled at 1°C/s. As for the sample cooled at the cooling rate of 5°C/s, even if the dwelling time of the sample in the γ-α phase transformation is shorter than that of the sample at 1 °C/s as shown in Table 5.1, more precipitate would be produced in the sample. Maybe the nucleation rate of the precipitation is faster for the sample cooled at 5°C/s compared to the sample at 1°C/s due to more nucleation sites of the precipitate provided by the granular bainite.

5.3 The effect of the coiling temperature on the Nb retention in the UCS steel

Before age hardening, the greatest difference in hardness between 675˚C and 500^{o}C coiling temperature results, was at 1^{o}C/s where the hardness of the sample at 675 ^{o}C is higher than that of the sample at 500˚C as shown in Table 4.5. While at 5 or 40˚C/s, the

hardness of the sample at the coiling temperature of 500˚C is similar to the sample at 675 ˚C. It is clear from Table 4.3 that at the cooling rate of 5 or 40˚C/s, more granular banite were produced in the sample at 500 ˚C compared to the sample at 675 ˚C. Therefore, at 5 or 40˚C/s, the hardness of the sample at 500 ˚C should be higher than that of the sample at 675 ˚C due to more granular bainite produced, which is obviously contradict the results. The reason of contradiction is that the strength of the steel is not only determined by grain refinement, but also determined by other strengthening mechanism shown in equation 5-1 [71].

$$\sigma_y = \sigma_0 + \sigma_s + \sigma_g + \sigma_p + \sigma_d \qquad (5\text{-}1)$$

where σ_y is the yield strength, σ_0 is the ferrite lattice strength, σ_s, σ_g, σ_p and σ_d are the strengthening contributions caused by solid solution, grain refinement, precipitation hardening and dislocation hardening respectively. Of the above mechanisms, grain refinement hardening and precipitation hardening are the most likely candidates to cause an increase in hardness for samples in the present study.

It is clear from Table 4.5 that at the same cooling rate, the age hardening increment of the sample with the low coiling temperature of 500˚C is much higher than that of the sample with 675˚C, which means more Nb atoms were retained in the solid solution before the age hardening and fewer precipitates were produced in the sample during CASTRIP process. Simoneau, who studied the progress of NbCN precipitate in HSLA, proposed that the precipitates are mainly produced during γ-α phase transformation in the cooling process and it is due to the large solubility difference of alloy carbides between the austenite and ferrite [2]. The solubility of Nb carbides in austenite is higher than that in ferrite and thus the Nb carbides will precipitate out during γ-α phase transformation in the cooling process [54-59]. It is clear from all dilatation curves that 500°C is outside of the γ-α phase transformation temperature range but 675°C is within

the range for all dilatation curves. Furthermore, with the same cooling rate, the diffusion rate of the sample at 500°C was lower and the diffusion time is shorter than that of the sample at 675°C as shown in Table 5.1. Therefore, at the same cooling rate, fewer precipitates were produced in the sample at the lower coiling temperature of 500°C compared to the sample at 675°C. Therefore, at 5 or 40°C/s, the hardness of the sample at 500°C is similar to that of the sample at 675°C despite more granular banite produced in the samples cooled to 500°C and at 1°C/s where both microstructures were polygonal ferrite, the hardness of the sample at 675 ^{o}C is higher than that of the sample at 500˚C.

6 Conclusions

This experiment is to study the effect of cooling rate and coiling temperature on the niobium retention in ultra-thin CASTRIP steel. From the study, the following conclusions are obtained:

1 The higher reheating temperature resulted in the larger austenite grain size and the lower $\gamma \rightarrow \alpha$ transformation temperatures which in turn resulted in the lower Nb retention and lower age hardening effect in the samples age hardened at 700°C for 60s for the cooling rate range from 1 to 40 °C/s from 900 to 500°C regardless of the coiling temperatures. The austenite grain size of the strip produced in CASTRIP process should be much larger than the austenite size achieved in this investigation therefore even a smaller Nb retention would be expected in the real strip.

2 The cooling effect on the Nb retention is very clear for the samples which have the coiling temperature of 500°C. The faster cooling rate results in the lower $\gamma \rightarrow \alpha$ transformation temperatures and the specimens spent less time in the $\gamma \rightarrow \alpha$

transformation temperature range and more Nb is retained in solid solution and the large age hardening effect.

3 The cooling effect on the Nb retention is complicated for the samples having the coiling temperature of 675°C because the coiling temperature is within the the $\gamma \rightarrow \alpha$ transformation temperature range. The retention of Nb depends on the the $\gamma \rightarrow \alpha$ transformation temperature range of the samples. If most of the $\gamma \rightarrow \alpha$ transformation occurred above the coiling temperature of 675°C then more Nb will be retained and the large age hardening effect will be produced.

4 The hardness of the UCS steel is not only determined by the microstructures, but also determined by precipitates produced during CASTRIP process. The findings suggest that even if more granular bainite were produced in the sample with the lower coiling temperature of 500^0C, the hardness of it is lower compared to the sample cooled to 675^0C due to fewer precipitates produced.

7 Suggestions for Future Works

The following works could be proposed for further studies and understanding how cooling rate and coiling temperature influence the Nb retention in UCS steel during cooling.

1 Scanning electron microscope (SEM) should be used to observe the micrograph of precipitate in the samples under the different cooling conditions. It is a strong evidence to prove the theory got from this work.

2 In order to better understand the relationship between coiling temperature and hardness of the steel, extra coiling temperatures are advised to be added to the

experiment and a curve revealing the relationship between coiling temperature and hardness of the steel should be plotted.

8 References

1. Chen, C. Y., et al. (2016). "Microstructural characterization and strengthening behavior of nanometer sized carbides in Ti-Mo microalloyed steels during continuous cooling process." Materials Characterization 114: 18-29.

2. Simoneau, R., et al. (1978). "Progress of NbCN precipitation in HSLA steels as determined by electrical resistivity measurements." Metal Science12(8): 381.

3. Carpenter, K., et al. (2012). The effects of Nb and V microalloying on hardenability and age hardening in ultrathin cast strip steels produced by the Castrip®1 process. AIST Steel Properties and Applications Conference Proceedings - Combined with MS and T'12, Materials Science and Technology.

4. Massalski, T. B. and H. Okamoto (1990). Binary alloy phase diagrams / editor-in-chief, Thaddeus B. Massalski ; editors, Hiroaki Okamoto, P.R. Subramanian, Linda Kacprzak, Materials Park, Ohio : ASM International. 2nd ed.

5. Callister, W. D., Jr. (2000). Materials science and engineering : an introduction / William D. Callister, Jr, New York ; Chichester : Wiley,5th ed.

6. Bhadeshia, H. K. D. H. and Edmonds, D.V. (1980), Acta Metall., Vol. 28, pp. 1265–1273.

7. Mehl, R. F. (1939), In Hardenability of Alloy Steels, ASM, Cleveland, OH, pp. 1–65.

8. Sawada M, Tsuzaki K, Maki T (1994), Unpublished research, Kyoto University.

9. Hehemann R F (1970), 'The bainite transformation', in Phase Transformations, Metals Park, OH, ASM, 397–432.

10. Matsuda H, Bhadeshia HKDH (2004), Kinetics of the bainite transformation, Proc R Soc Lond A 460:1707–1722.

11. Pereloma, E. and D. V. Edmonds (2012), Phase transformations in steels. Fundamentals and diffusion-controlled transformations / Guest editor Elena Pereloma, D. V. Edmonds, Cambridge : Woodhead Publishing Ltd.

12. M. Kumar (1994), "Isothermal Decomposition of Coarse-Grained Austenite in Low-Carbon, Copper-Containing HSLA-80 Plate Steel," M.S. thesis, Colorado School of Mines, Golden, CO.

13. Killmore, C. R., et al. (2008). Development of plain carbon and niobium microalloyed ultra-thin cast strip products produced by the castrip® process. 3rd International Conference on Thermomechanical Processing of Steels, TMP.

14. H.K.D.H. Bhadeshia (2001), Bainite in Steels: transformations, microstructure and properties, IOM Communications, London.

15. M.Diaz-Fuentes, A.Iza-Mendia, I.Guttierez (2003), Analysis of Different Acicular Ferrite Microstructures in Low-Carbon Steels by Electron Backscattered Diffraction. Study of Their Toughness Behavior, Metall. Mater. Trans. A34A 2505–2516.

16. R.A. Farrar, P.L.Harrison (1987), Review: acicular ferrite in carbon-manganese weld metals: anoverview, J. Mater. Sci. 22 3812–3820.

17. W.Wang, W.Yan, L.Zhu, P.Hu, Y.Shan, K.Yang (2009), Relation among rolling parameters, microstructures and mechanical properties in an acicular ferrite pipeline steel,Mater.Des.30 3436–3443.

18. R.F. Mehl and W.C. Hagel (1956), The Austenite:Pearlite Reaction, Progress in Metal Physics, B. Chalmers and R. King, Ed., Vol 6, Pergamon Press, New York, p 74–134.

19. Carpenter, K. R. and C. R. Killmore (2015). "The effect of Nb on the continuous cooling transformation curves of ultra-thin strip CASTRIP© steels." Metals 5(4): 1857-1877.

20. S.W. Thompson, D.J. Colvin, and G. Krauss (1990), Continuous Cooling Transformations and Microstructures in a Low-Carbon, HighStrength Low-Alloy Plate Steel, Metallurgical Transactions A, Vol 21A, p 1493– 1507.

21. Y.E. Smith, A.P. Coldren, and R.L. Cryderman (1971), ManganeseMolybdenum-Niobium Acicular Ferrite Steels with High Strength, in Toward Improved Ductility and Toughness, Climax Molybdenum Co, Ann Arbor, MI, p 119– 142.

22. S.W. Thompson, D.J. Colvin, and G. Krauss (1996), Austenite Decomposition During Continuous Cooling of an HSLA-80 Plate Steel, Metallurgical and Materials Transactions A, Vol 27A, p 1557– 1571.

23. G.R. Speich and T.M. Scoonover (1988), Continuous Cooling Behaviour and Strength of HSLA 80 (A710) Steel Plates, in Processing, Microstructure and Properties of HSLA Steels, A.J. DeArdo, Ed., TMS, Warrendale, PA, p 263– 286.

24. Krauss, G. (2005). Steels : processing, structure, and performance / George Krauss, Materials Park, Ohio : ASM International.

25. T. Araki, et. Al (1992), Atlas for Bainitic Microstructures Vol. 1, ISIJ, Tokyo, p 1-20.

26. L.J. Habraken and M. Economopoulos (1967), Bainitic Microstructure in Low-Carbon Alloy Steels and Their Mechanical Properties, Transformation and Hardenability in Steels, Climax Molybdenum Co., Ann Arbor, MI, p 69– 108.

27. Desaguliers, J.T. (1745), A Course of Experimental Philosophy, London, 436-46.

28. Becker,K.(1926),"An X-Ray method to Determine the Thermal Expansion Coefficient at High Temperature" Z.Physik,40,37-41.

29. Jacobs, S. F., Berthold, J. W., Ⅲ, and Osmundsen, J. (1972), “Ultraprecise Measurement of Thermal Expansion Coefficients-Recent Progress,” in AIP Conf. Proc. No. 3- Thermal Expansion, American Institute of Physics, New York, 1-12.

30. Cezairliyan, A. (1971),"A High-Speed Method of Measuring Thermal Expansion of Electrical Conductors" Rev. Sci. Instr ,42, 540-1.

31. Lee, S., et al. (2013). "Effect of Niobium on the Ferrite Continuous-Cooling-Transformation (CCT) Curve of Ultrahigh-Thickness Cr-Mo Steel." Metallurgical & Materials Transactions. Part A 44(6): 2523-2532.

32. Homberg, D., N. Togobytska and M. Yamamoto (2009). "On the evaluation of dilatometer experiments." Applicable Analysis 88(5): 669.

33. García de Andrés, C., F. G. Caballero, C. Capdevila and L. F. Álvarez (2002). "Application of dilatometric analysis to the study of solid–solid phase transformations in steels." Materials Characterization 48: 101-111.

34. Caballero FG, Capdevila C, Garcı´a de Andre´s C (2001). Kinetics and dilatometric behaviour of non-isothermal ferrite-to-austenite transformation. Mater Sci Technol;17:1114– 8.

35. Garcia C, Alvarez LF, Carsi M (1992). Effects of heat treatment parameters on non-equilibrium transformations and properties of X45Cr13 and X60Cr14MoV martensitic stainless steels. Weld Int; 6:612– 21.

36. Yang, G.-w., et al. (2014). "Austenite Grain Refinement and Isothermal Growth Behavior in a Low Carbon Vanadium Microalloyed Steel." Journal of Iron and Steel Research International 21: 757-764.

37. Nowotnik, A. and T. Siwecki (2010). "The effect of TMCP parameters on the microstructure and mechanical properties of Ti–Nb microalloyed steel." Journal of Microscopy 237(3): 258-262.

38. Datta, S., et al. (2004). "Effect of thermomechanical processing and aging on microstructure and precipitation hardening in low carbon Cu–B steel." Ironmaking & Steelmaking 31(4): 312-318.

39. H. Beladi and P. D. Hodgson (2007), Scr. Mater., 56, 1059.

40. S. Akamatsu, M. Hasebe, T. Senuma, Y. Matsumura and O.

Akisue (1994), ISIJ Int., 34, 9.

41. K. J. Irvine, F. B. Pickering and T. Gladman(1967), J. Iron Steel Inst.

, 205, 161.

42. P. R. Rios (1988), Mater. Sci. Technol., 4, 324.

43. H. Sawamura and T. Mori (1952), J. Iron Steel Inst., 43, 31.

44. R. W. Fountain and J. Chipman (1962), Trans. AIME, 224, 599.

45. Gladman, T. (1999). "Precipitation hardening in metals." Materials Science and Technology15(1): 30-36.

46. L. M. BROWN and R. K. HAM (1971), 'Strengthening methods in crystals', (ed. A. Kelly and R. B. Nicholson), 12; London, Applied Science Publishers.

47. M. F. ASHBY (1958), in 'Oxide dispersion strengthening', (ed. G. S. Ansell et al.), 143; New York, Gordon and Breach.

48. A. Ghosh, S. Das, S. Chatterjee, P. Ramachandra Rao (2006), "Effect of cooling rate on structure and properties of an ultra-low carbon HSLA-100 grade steel", Mater. Charact. 56 59–65.

49. Y.W. Kim, S.W. Song, S.J. Seo, S.-G. Hong, C.S. Lee (2013), “Development of Ti and Mo microalloyed hot-rolled high strength sheet steel by controlling thermomechanical controlled processing schedule”, Mater. Sci. Eng. A 565 430–438.

50. M.D.C. Sobral, P.R.Mei, H.J. Kestenbach (2004), “Effect of carbonitride particles formed in austenite on the strength of microalloyed steels”, Mater. Sci. Eng. A 367 317–321.

51. J. Hu, L.-X. Du, J.-J. Wang, Q.-Y. Sun (2014), “Cooling process and mechanical properties design of hot-rolled low carbon high strength microalloyed steel for automotive wheel usage”, Mater. Des. 53 332–337.

52. William F. Smith & Javad Hashemi, 2011,“Foundations of materials science and engineering”, 5nd edition, McGraw-Hill, New York.

53. T. Gladman (1997), The physical metallurgy of microalloyed steels, The Institute of Materials, London.

54. H. Beladi and P. D. Hodgson (2007), Scr. Mater., 56, 1059.

55. S. Akamatsu, M. Hasebe, T. Senuma (1994), Y. Matsumura and O. Akisue: ISIJ Int., 34, 9.

56. K. J. Irvine, F. B. Pickering and T. Gladman (1967), J. Iron Steel Inst., 205, 161.

57. P. R. Rios (1988), Mater. Sci. Technol., 4, 324.

58. H. Sawamura and T. Mori (1952), J. Iron Steel Inst., 43, 31.

59. R. W. Fountain and J. Chipman (1962), Trans. AIME, 224, 599.

60. Shrestha, S. L., et al. (2013). "Cluster strengthening of Nb-microalloyed ultra-thin cast strip steels produced by the CASTRIP® process." Materials Science and Engineering A568: 88-95.

61. H.-J. Kestenbach, J. Gallego (2001), On dispersion hardening of microalloyed hot strip steels by carbonitride precipitation in austenite, Scr. Mater. 44 791–796.

62. Z. Jia, R. Misra, R. O'Malley, S. Jansto (2011), Fine-scale precipitation and mechanical properties of thin slab processed titanium–niobium bearing high strength steels, Mater.Sci. Eng. A 528 7077–7083.

63. P. Haasen, B.L. Mordike (1996), Physical Metallurgy, Cambridge University Press, Cambridge, UK,.

64. Jun, H. J. (2003). "Effects of cooling rate and isothermal holding on the precipitation behavior during continuous casting of Nb–Ti bearing HSLA steels." Scripta Materialia 49(11): 1081-1086.

65. Ghosh, A., et al. (2003). "Influence of thermo-mechanical processing and different post-cooling techniques on structure and properties of an ultra low carbon Cu bearing HSLA forging." Materials Science & Engineering A348: 299-308.

66. Bu, F. Z., et al. (2015). "Influence of cooling rate on the precipitation behavior in Ti-Nb-Mo microalloyed steels during continuous cooling and relationship to strength." Materials Characterization A102: 146-155.

67. Park, D.-B., et al. (2013). "Strengthening mechanism of hot rolled Ti and Nb microalloyed HSLA steels containing Mo and W with various coiling temperature." Materials Science and Engineering: A 560: 528-534.

68. L.J. Habraken, M. Economopoulus (1967), Transformation and hardenability in steels, in: Climax Molybdenum Co, Ann Harbor,MI, p. 69.

69. S.W. Thompson, D.J. Colvin, G. Krauss (1988), Scripta Metall. 22 1069.

70. B.L. Bramfitt, J.G. Speer (1990), Metall. Trans. 21 817.

71. S.K. Ghosh, P.S. Bandyopadhyay, S. Kundu, S. Chatterjee (2011), Mat. Sci. Eng. A. 528 , 7887–7894.